Characterization of Different Aluminium Alloys of the Series 6000 and of their Joining Processes

Valentin Richter-Trummer

Dissertation

Mestrado Integrado em Engenharia Mecânica

Faculdade de Engenharia da Universidade do Porto

February 2008

"The diamond cannot be polished without friction, nor man perfected without trials."

Confucius [1]

Abstract

Different aluminium alloys are analyzed as regards their joining process and the resulting mechanical properties and fatigue life.

Strain measurements using strain gauges and FBG sensors, and temperature measurements using FBG sensors, thermocouples and a thermal imaging device, were applied to the characterization of the MIG and FSW processes.

Laser beam welded joints of the same alloy are characterized by tensile and fatigue tests and compared to another aluminium alloy of the same series, in a study including a simple metallurgical analysis.

Crack growth tests are performed on another alloy of the same series.

Finally an attempt is made to measure longitudinal residual stress originated from MIG and FS welding using the Contour method.

Keywords

aluminium alloys, crack propagation, Contour method, fatigue, fiber Bragg grating sensors, friction stir welding, laser beam welding, metal inert gas welding, residual stress, thermal image analysis, thermocouples

Acknowledgments

The present work is part of research project supported by FCT: project WELDING in cooperation with INESC-Porto, contract number: PTDC/EME-TME/66362/2006.

The author acknowledges the support of P. M. S. T. de Castro and Eng. Pedro Moreira during all this work.

The FS weldings in the INDUMA milling machine were executed by Mr. J. F. R. Almeida. Eng. M. V. Figueiredo and Eng. Tec. R. Silva and Eng. Sérgio Tavares of DEMEGI-FEUP supported the experimental work.

The FLIR thermographic imaging equipment was used by courtesy of Professor L. A. Ferreira.

The use of a KISTLER load cell in the present work was made possible by Professor A. P. M. Baptista, with the help of Dr. A. M. R. de Aguiar Vieira.

The coordinate measuring machine of INEGI was used with the kind help of Eng. P. Teixeira.

Wire EDM cut was made in Autoconceptus, Rio Tinto, Portugal.

AIMEN, Porriño, Spain, contributed to this work with the execution of LBW joints.

The European Union project DaToN, contract number: AST4-CT-2005-516053, contributed to certain aspects of this work (da/dN behavior characterization).

Resumo

Várias ligas de alumínio da série 6000 e os seus processos de ligação são analizados neste trabalho em termos de propriedades mecânicas e comportamento à fadiga.

A ligação de alumínios pelos processos MIG e FSW é analizada em termos de distribuição de deformações utilizando extensometria e fibras de Bragg, e de temperatura utilizando termopares, fibras de Bragg e termografia infravermelha.

Ligações LBW da mesma liga são analizadas em termos de vida à fadiga e comparadas com outra liga de aluminio.

São também efectuados ensaios de propagação de uma fenda noutra liga de alumínio da mesma série.

Para finalizar é feita uma tentativa de medir tensões residuais longitudinais resultantes de soldaduras MIG e por FSW, recorrendo ao método *contour*.

Palavras chave

alumínio, fadiga, método contour, propagação de fendas por fadiga, sensores de fibras de Bragg, soldadura por fricção linear, soldadura por gás inerte, soldadura por laser, tensão residual, termografia infravermelha, termopar

List of acronyms

AA	Aluminium Association
ASTM	American Society for Testing and Materials
BM	base material
CMM	coordinate measuring machine
CT-specimen	compact tension specimen
DEMEGI	Departamento de Engenharia Mecânica e Gestão Industrial (FEUP)
FBG	fibre Bragg grating (sensor)
FE	finite element (analysis/model)
FS	friction stir (welding)
FSW	friction stir welding
FEUP	Faculdade de Engenharia da Universidade do Porto
HAZ	heat affected zone
HF	hydrofluoric acid
HSM	high speed machining
INEGI	Instituto de Engenharia Mecânica e Gestão Industrial
INESC Porto	Instituto de Engenharia de Sistemas e Computadores do Porto
IST	Instituto Superior Técnico
LBW	laser beam welding
MAG	metal active gas (welding)
MIG	metal inert gas (welding)
PID	Proportional, Integrator, Derivator (servohydraulic machine adjustments)
SN - curve	Stress level verses number of cycles curve
SPAP2	least-squares spline approximation function within MATLAB
TMAZ	thermo-mechanical affected zone
TWI	The Welding Institute
wEDM	wire electro discharge machining

List of symbols

α_A	thermal expansion coefficient of optical fiber
α_n	thermo-optic coefficient
λB	Bragg wavelength
ΔλB	Bragg wavelength shift
ε	strain
με	microstrain = 10^{-6} ε
σ	stress
a	crack length
C, m	Constants of the Paris crack growth law
K	stress intensity factor
ΔK	range of K (K_{max} - K_{min})
K_c	fracture toughness
k	order of polynomials used in SPAP2 function within MATLAB
p, q, n	constants of the Forman crack growth law
p_e	strain optic coefficient
R	stress ratio
R^2	coefficient of determination - square of the correlation between the response values and the predicted response values (goodness of fit)
N	number of cycles
F	force
n	constant of the Walker crack growth law
T	Temperature

Contents

1. Introduction

The aim of this work is to characterize joining processes applicable to series 6000 aluminium alloys. The characterization involves the process itself, where temperature and strain distributions are monitored using fiber Bragg grating (FBG) sensors and other means, and the resulting joints, through metalurgical and mechanical testing including fatigue.

1.1. Joining processes

1.1.1. MIG

Metal inert gas welding (MIG) is a fusion welding process with a consumable wire electrode. Developed in the 1940s, it is now widely used in industrial applications and is also well understood from the scientific point of view.

The high cost of the inert gas limits its applicability to non-ferrous metals. For ferrous metals half inert gases like CO_2 may be used (MAG).

It is referred to as a semi-automatic process, since the wire length is automatically adjusted by the welding tool. This way high welding speeds can be achieved, and long continuous welds may be performed without stops.

Since it uses a gas shield to protect the welding pool during solidification, it is mostly used indoors. The gas also stabilizes the electric arc and assists in the transfer of the metal from the filler wire. Continuous current is normally used, in very few cases alternating current may also be used. Because of its versatility, MIG welding is one of the most widespread welding processes. Welding can either be done by hand or by a robot. All welding positions may be used, al- though since this is a fusion process the flat position is recommended. [2]

In the present work, MIG welding was used in the context of the study of temperature and strain fields.

1.1.2. FSW

Friction stir welding was developed and patented by the TWI in 1991 [3] as a novel solid-state joining process with the ability to weld high strength aluminium alloys difficult to weld with fusion techniques, and even multi-material joints [4]. The process was initially introduced for aluminium alloys, but is now also being studied for steels and other metals. It can operate in all welding positions since no fusion occurs. This property is however limited by the robots used; mostly parallel structure robots are used because of their higher rigidity, and these are less flexible than their serial structure counterparts. No hand welding can be done using this method so far.

No filler wire is used for this type of welding which means that only base material will exist in the final result since the pin is non-consumable. This means that this process has a better ability of retaining the original material properties than a fusion technique using filler wire.

In the friction stir welding (FSW) process a probe (often also called pin) stirs the base material and the rotational friction softens the metal up short of its solidus temperature, which assists in the mixing of both parts. The shoulder helps in the heating of the metal, since it contacts with the surface of the weld. The geometry of this shoulder, i.e., its diameter and form of the base does influence the final quality of the weld. A concave shoulder for example leads to better surfaces than a flat shoulder. Figure 1 shows a scheme of the welding process.

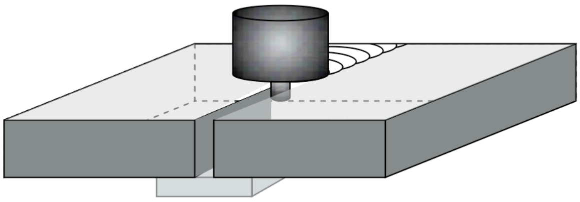

Fig. 1 - scheme of the FSW process

The backing plate required for this process does also influence the welding, since it dictates the heat evacuation through the bottom of the plate, and influences the material properties and their distribution in this way.

Rigid clamping has to be used to prevent both plate halves from separating during the welding process. High reaction forces may be expected, since the probe penetrates the metal. Normally dedicated manufacturing equipment is used in this process, since a high rigidity is required along with force control. It is however also possible to use traditional machining devices, e.g. milling machines, that have been altered for this new process, as in IST or more recently in the workshop of DEMEGI-INEGI (FEUP).

FS welding has the ability to join different thicknesses and has other advantages like a low defect and distortion probability. Therefore it is already in use in the aerospace [5] and automotive industries for joining high strength Aluminium alloys, providing clean and consistently high bond strengths.

As for the welding speed, according to TWI, FSW equals MIG in butt-welding 6 mm thick aluminium. FSW is slower than MIG in thinner materials and faster than MIG in thicker materials, [6]. The quality of the welding depends on a great variety of factors like the pin angle, rotating speed and advancing speed. The influence of these parameters is currently being studied.

Defects inherent to this process are the keyholes that are created when the probe leaves the work piece at the end of the welding line. These keyholes have to be filled after the welding is done. Various methods have been developed for this purpose.

In the present work temperature and strain fields created by FSW were studied.

1.1.3. LBW

The use of lasers for welding has exhibited tremendous growth in a broad range of industries over the last decade, contributing to improved efficiency and reduced costs.

Laser beam welding is a common manufacturing method for a wide range of steel products. However, the process has only recently been approved for critical applications involving aluminium alloys, notably in the aerospace and automotive industries. The properties of aluminium alloys influence the interaction between the beam and the material to a far greater extent than for steels.

Porosity, solidification cracking, and poor weld bead geometry tend to be the most frequently encountered imperfections. These can be eliminated through the use of appropriate filler materials, process gases, material preparation, and in some instances, adaptive control systems. Very little work has been reported on the corrosion properties of laser welded aluminium alloys. [8]

With the wide application of aluminium alloys in automotive, aerospace and other industries, laser welding has now become a critical joining technique for aluminium alloys.

In the present work a fatigue characterization of LBW joints was carried out.

1.2. Process property acquisition

1.2.1. FBG sensor

A fiber Bragg grating (FBG) is a type of distributed Bragg reflector contained in a short segment of optical fiber that reflects particular wavelengths of light and transmits all others. This is achieved by adding a periodic variation to the refractive index of the fiber core, for example by the means of a laser beam, which generates a wavelength specific dielectric mirror. A fiber Bragg grating can therefore be used as a wavelength-specific reflector. Different signals may be measured with the same fiber at the same time, since the acquisition system can separate the signals due to different wavelengths used for reflection.

In a FBG sensor, the quantity to be measured causes a shift in the Bragg wavelength, $\Delta\lambda B$. The relative shift in the Bragg wavelength, $\Delta\lambda B$ / λB, due to an applied strain (ε) and a change in temperature (ΔT) is approximately given by,

$$[\frac{\Delta\lambda_B}{\lambda B}] = (1 - p_e)\epsilon + (\alpha_\Lambda + \alpha_n)\Delta T \qquad (1)$$

where p_e is the strain optic coefficient, the thermal expansion coefficient of the optical fiber is α_Λ, and the thermo-optic coefficient is given by α_n. [9]

As it can be seen in equation 1, eliminating the strain component by special gluing techniques, the temperature variation may be isolated from other signals as long as the shift in the Bragg wavelength is known for the fiber used. Knowing the temperature and the material constants, the calculation of strain is a matter of subtracting the known temperature component from the measured shift.

1.2.2. Thermocouple

Thermocouples are widely accepted temperature measuring devices, due to their large temperature range, stability and low cost. Using thermocouples a large number of points can be measured. In this work they are therefore used essentially for validation of FBG sensor results.

Type K thermocouples (chromel alumel) with 0.08 mm diameter wire are used, which give reliable temperature results in the range of -200ºC to 800ºC while keeping the price-point relatively low. They may also be used with a slightly higher temperature range (-200ºC to 1100ºC), although attention must be paid to de-calibration and drift due to oxidation. Thermocouples of type K have a sensitivity of 40.44 µV/ºC.

A description of how to manufacture these thermocouples by welding may be found in [Annex A].

1.2.3. Infrared thermography

Thermal imaging extends the human vision to the infrared spectrum. The main goal is to measure thermal energy (emitted in the infrared spectrum) which is emitted by a body. Knowing the emissivity of this body, conclusions over the bodies temperature may be drawn.

This is an interesting process, since any body with a temperature higher than 0K emits thermal energy. This energy depends upon its wave-length, so for a better understanding the electromagnetic frequency band has to be known better.

Figure 2 shows the electromagnetic spectrum, and the regime where infrared emissions can be expected.

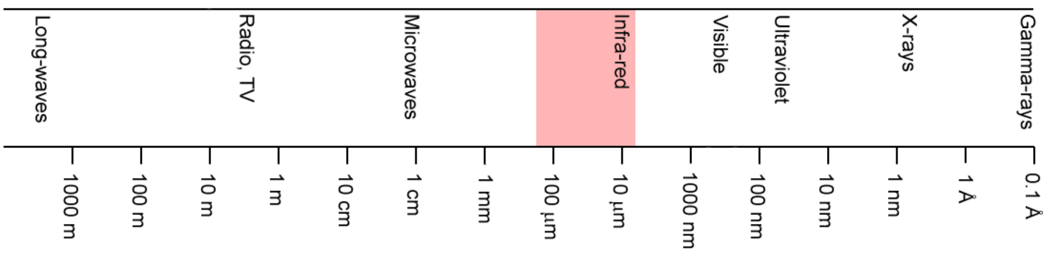

Fig. 2 - electromagnetic spectrum; wavelength and their designation [10]

The thermal imaging device used, FLIR PM575, is able to shift infrared waves (essentially those in the sub-spectrum 10 μm a 100 μm) to the visible spectrum. For image acquisition a CANOPUS ADVC55 analog to digital converter is used.

Various laws have been developed to translate wavelength into emitted energy; they may be found under the names of Kirchhoff, Planck, Wien and Stefan-Boltzman [11].

This is a non-contact measurement process, which has not only inherent advantages, but also some problems. For example the transmissibility of the space where measurements are performed influences the results. Only superficial temperatures can be acquired, and since the welding process alters also the specimens surface, some interpretation difficulties are to be expected.

In the present case, measured surfaces are painted in black, so that the reflection of the aluminium alloy does not influence infrared thermography results. This preparation process leads to another problem. Since the paint evaporates with high temperatures, in the welding line, the pure surface with different emissive properties is captured after the torch has passed which may lead to inaccurate or inadequate interpretations of the obtained results.

1.2.4. Strain gauge

Strain gauges are the more traditional way of acquiring strain on surfaces. Their use is well documented and the results may be used for validation of novel measuring processes as long as the ambient conditions permit their usage. Standard strain gauges should not be used beyond 60ºC continuous or 90ºC short term working temperature [12]. Special high temperature capable strain gauges have to be used in welding applications.

In the present work, strain gauges are essentially used for validation of FBG sensor results during a welding process. Maximum temperature of use is essentially limited due to the use of cyanoacrylate based glue which has an important loss of properties for such high temperatures and does therefore not guarantee a good transmission of strain form the plates surface to the strain gauges measuring grid.

1.3. Material property characterization

A great variety of tests can be performed on Aluminium alloys in order to define its main characteristics. Some of these were used throughout the present work, including fatigue crack initiation (SN) and crack growth tests.

1.3.1. Tensile test

Tensile tests define some of the most important and well known material parameters, such as its rigidity, yield strength and rupture stress. In fatigue characterization these tests are also necessary for the definition of stress levels for SN-tests, since these levels are defined in terms of percentage of yield strength.

1.3.2. Crack initiation test (SN-curve)

The SN-curve is probably one of the best known ways to characterize the fatigue life of specimens. In this type of tests, a specimen is loaded by a harmonic function at constant frequency and amplitude until it breaks. The final number of cycles for a given stress level defines one point on this curve. At least three specimens at each level should be tested, preferably more, since fatigue life can have great variations.

In the SN curve approach, structural details, like butt-welding, are grouped into categories sharing a common resistance to fatigue and associated SN curve. These curves give the allowable stress range (S) for a particular detail and material in terms of obtainable fatigue life (N), where the stress range is the nominal stress perpendicular to the crack surface, not considering local stress concentration factors. [13]

In current codes and standards on fatigue strength assessment of conventional fusion welded joints and parent material, fatigue design curves are obtained by taking into account the scatter of fatigue behavior and providing a reference curve with a probability of survival at greater or equal than 97.7% [14].

Data characterizing the scatter is therefore required, and the present work includes experimental results for different laser beam welded Aluminium alloys.

1.3.3. Crack growth rate determination (CT-specimen)

The compact tension (CT) specimen crack growth test aims to measure the crack growth rate. Therefore a specimens crack is measured at predefined intervals during crack growth. The ASTM E647 standard should be followed thoroughly in order to provide confidence on the results. The number of tests necessary to define material properties depends on the material and on the accuracy of the measurements made.

1.3.4. Microhardness measurements

Microhardness measurements permit the definition of the extent of heat affected zone in fusion welding and thermomecanically affected zone (TMAZ) in friction stir welding. Hardness is to be expected to be lower in this zone.

1.3.5. Micrography

Micrographic images show the microstructure of metals and other materials. This makes it possible to compare grain constitution and size of the base material and the weld bead. The uniformness of material after welding can be seen by this analysis.

1.3.6. Macrography

Macrographic images give an overview over the extend of deposited material in welds. Since in most cases different materials are used for deposition in fusion welding, this images provide a good way of comparing the extend of the influence of different welding techniques. Aluminum alloys, essentially when welded without filler material, are more difficultly analyzed by this technique due to low contrast between the welded zone and base material.

1.3.7. Fractography

Fractography is the study of the features of fracture surfaces. It is useful for determination of the extend of the fatigue cracking zone and final ductile rupture zones. Material defects which lead to crack initiation may also be found.

1.4. Series 6000 aluminium alloys

The Aluminium Association (AA), Inc. is the trade association for producers of primary aluminium, recyclers and semi-fabricated aluminium products, as well as suppliers to the industry [15].

This association has defined various series of aluminium alloys, based on their chemical constitution.

Wrought aluminium is identified with a four digit number, where the first digit identifies the main alloying elements (1 = 99% Al (almost pure Al); 2 = Copper; 3 = manganese; 4 = Silicon; 5 = Magnesium; 6 = Magnesium & Silicon; 7 = Zinc; 8 = others), the second single digit, if different from 0, indicates a modification of the specific alloy, and the third and fourth digits are arbitrary numbers given to identify a specific alloy in the series. The designation is then followed by a dash, a letter identifying the type of heat treatment (F - Extruded and air cooled; O - Softened, annealed at 350-500°C, for 1-5 hours; T - Heat treated) and a 1 to 4 digit number identifying the specific temper (T4 - Solution heat treated and naturally aged at 20°C, for 5-10 days, T6 - Solution heat treated, artificially aged, for example) [16, 17].

The main components of the series 6000 alloys are magnesium and silicon which precipitate in the form of Mg_2Si inside a α-phase aluminium matrix. There is often an iron corrector such as manganese or chromium; occasionally small amounts of copper or zinc to improve the strength without substantial loss of corrosion resistance; boron in conductors to remove titanium and vanadium; zirconium or titanium to control the grain size. Lead and bismuth are sometimes added to improve machinability, but they are less effective than in magnesium-free alloys. The chemical constitution limits of series 6000 aluminium alloys are presented in Table 1.

Table 1 - chemical composition of series 6000 aluminium alloys [18]

Mg:	0.2 - 1.5 %	Mn:	up to 1.5 %
Cu:	up to 2.0 %	B, Ti, Zr:	up to 0.3 %
Si:	0.2 - 2.0 %	Cr:	up to 0.5 %
Zn:	up to 2.5 %	Pb, Bi:	up to 1 %

It should be noted that different alloys within this series may have similar compositions in some cases.

Mechanical properties of the commercial alloys depend on content of Mg, Si, Cu and other alloying elements, treatment conditions and exact heat treatment.

Fully hardened alloys show some tendency to intergranular fractures in tension testing, but manganese additions reduce this tendency. Silicon precipitates, as platelets, may be responsible for this brittleness.

The structure of the alloys is relatively simple, being the main constituent Mg_2Si in an aluminium matrix, which in the heat treated condition is in solution creating the possibility of age hardening after artificial aging. If sufficient copper and silicon are present, it may be replaced at least partly by $Cu_2Mg_8Si_6Al_5$, which will produce some hardening also with natural aging. Series 6000 aluminium can be precipitation hardened, but not to the high strengths that the 2000 and 7000 series can reach [18].

2. Welding process characterization

The experimental work is based on the analysis of welding processes and their resulting joints. In this section, welding parameters used for the different specimens are defined.

2.1. Welding parameters

2.1.1. MIG welding

The MIG weld described in Tables 2 was performed on a FANUC Arc Mate SR welding robot.

Table 2 a) - Welding robot

Robot	brand/model	FANUC Arc Mate SR
	physical configuration	articulated
	nr. of axis	6
	pay load	10 kg
	repeatability	±0.1 mm
	accuracy	±0.1 mm
positioner (table)	nr. of axis	2
welding torch (MIG/MAG)	brand	Daidan
	maximum current	350 A

The plates dimensions and filler wire designation are presented in Table 2 b).

Table 2 b) - Material to be welded and filler wire designation

filler wire	brand	ESAB: OK AUTROD 18.15
	electrode designation	SFA: A5.10; AWS: ER5356; DIN 1732: SG AlMg5
	diameter	Φ1 mm
base material	material	Al6082-T6
	dimensions	250 x 360 x 3 mm

The welding parameters presented in Table 2 c) were used.

Table 2 c) - Welding parameters

welding parameters	arc voltage	17.1 V
	current	128 A
	stick-out	20 mm
	welding speed	700 mm/min
geometry	length of welding line	320 mm (20 mm space on each side)
	type	deposition / but weld

2.1.2. FSW

The INDUMA milling machine of the workshop of DEMEGI-INEGI-FEUP shown in Figure 3 was used for this welding.

Fig. 3 - INDUMA milling machine used for friction stir welding tests

The welding parameters are shown in Table 3.

Table 3 - Welding parameters used for the FSW specimen

travel speed:	290 mm/min
tilt angle:	0º
rotating speed:	1500 rpm
plate thickness:	3.02 mm
tool penetration:	2.95 mm
shoulder diameter:	15 mm
pin diameter:	6 mm

In test B, two passes are performed, one in each direction. In all other tests, only one pass is made.

The borders of the weld-surface are prepared by milling for the but welds. The plate is rigidly clamped onto the milling machines working table. For some of the tests the welding line is only deposited on a flat plate, since this fact is not expected to change the temperature variation considerably.

2.2. Temperature distribution

Five tests were made on FSW welding, and two on MIG welding. They will be referred to as test A, test B, test C, test D and test E for FSW and test A, test C for MIG. Experiments with the same letter designation were made on the same day using the same measuring devices. For FBG sensors, there have to be made a lot of experimental tests, since little information about their correct usage in welding process parameter verification exists.

2.2.1. FSW

Test A - thermocouples and FBG sensors

Four thermocouples were used to measure the temperature distribution in the center of the plate as the tool passes. The first tests were performed using a HBM Spider8 data acquisition system with a data acquisition rate of about 25 Hz. In Figure 4 the instrumentation scheme is presented. In Figure 5 the temperature distribution of the center-line obtained by this instrumentation can be seen.

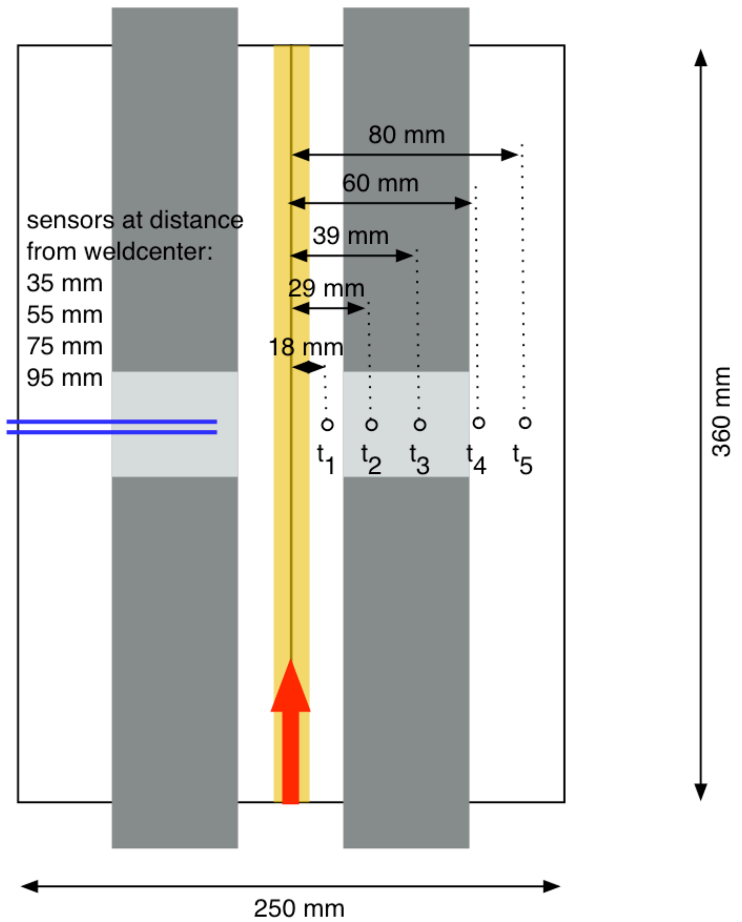

Fig. 4 - Instrumentation scheme for FSW

FBG sensors are bonded in all their extent for measuring deformation, and only at their tips for measuring temperature using a cyanoacrylate based adhesive. Deformation is measured perpendicular to the welding direction only. It should however be noted that four measuring gratings are used on each fiber. This setup should only be used after the correct measuring technique has been defined in order to reduce complexity.

Figure 5 shows the temperature distribution obtained during the welding of this plate using thermocouples. Figure 6 shows equivalent measurements taken by FBG sensors.

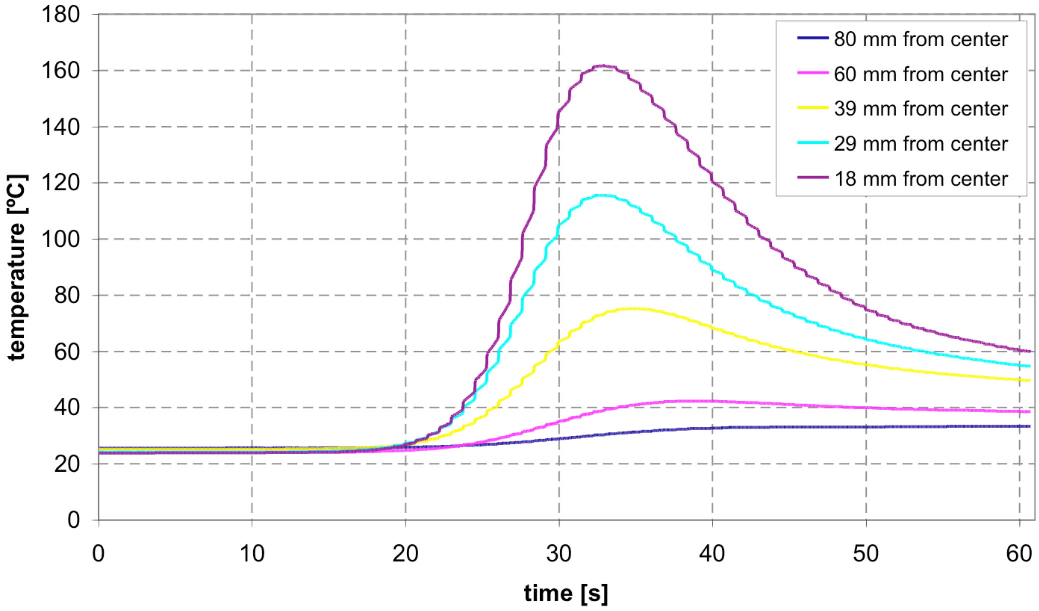

Fig. 5 - temperature variation perpendicular to the welding line measured by thermocouples

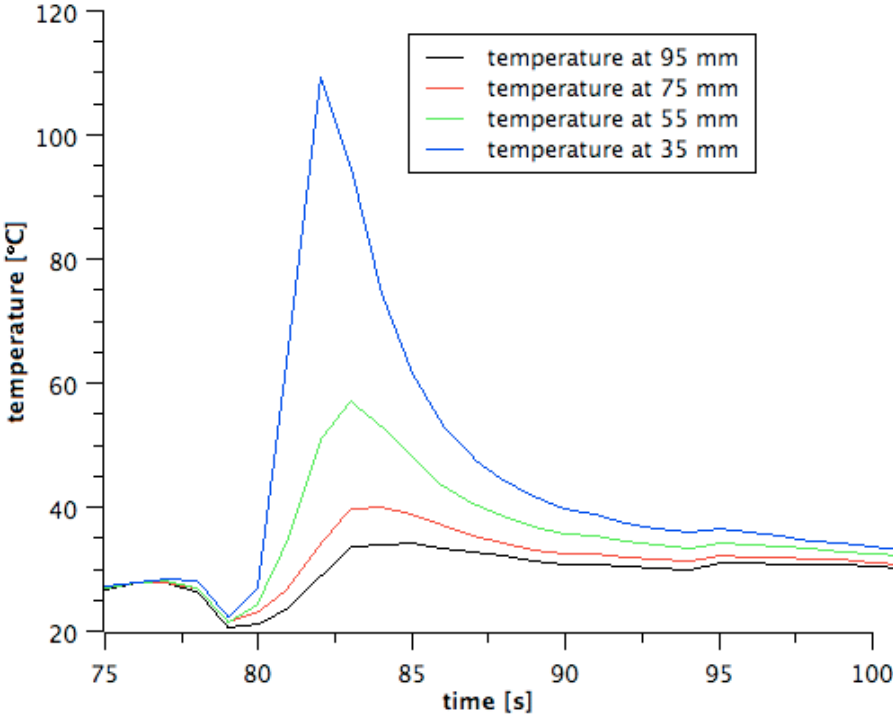

Fig. 6 - temperature variation perpendicular to the welding line measured by FBG sensors

Both results represented in Figure 5 and 6 are relatively similar. Nevertheless, Figure 6 shows phenomena which should be better analyzed in further tests, like the temperature decrease before it starts rising. This does not happen according to the thermocouple measurements. Most likely the bonding technique used in this case does not guarantee the insulation of temperature related fiber deformations from strain related fiber deformations. The complex setup due to the use of various gratings on the same fiber should be simplified in further tests. The acquisition rate is also insufficient in the case of Figure 6. Measurements are done at a rate of only 1 Hz.

It should be noted that a common time-scale has to be found for both measurements. The usage of some sort of fuse which brakes at the a well defined time an is captured by both measuring processes would be acceptable for time synchronization.

Test B - thermocouples and infrared thermal imaging device

A second test was made using thermocouples and an infrared imaging device in order to gather more temperature data. Thermocouples were used on the plate, whereas thermal images were essentially taken to measure the tools temperature without contact.

In Figure 7 the temperature distribution in the centerline similar to the first test presented above can be seen.

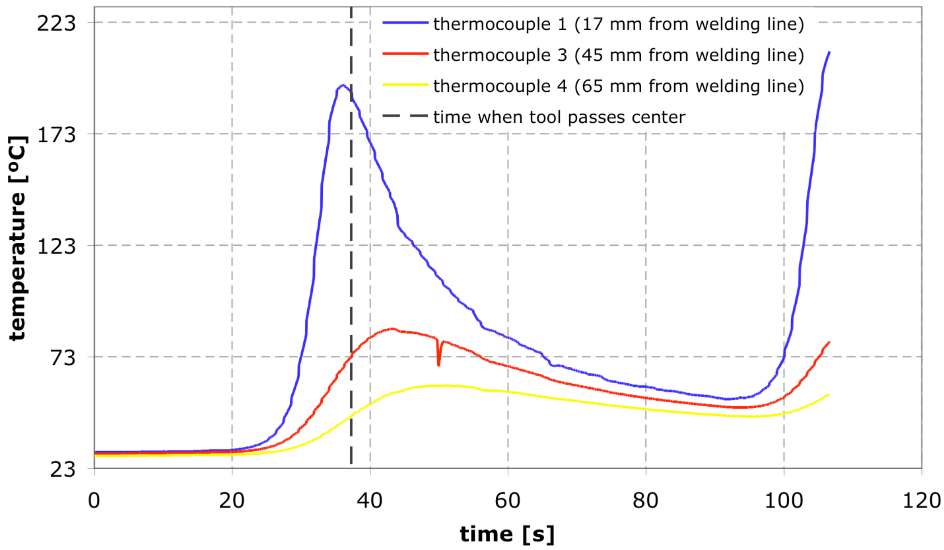

Fig. 7 - temperature distribution along the center-line as obtained by the thermocouples

Thermocouple 2 has failed due to unknown reasons and its measurements should not be considered. Only three measurement points are therefore available.

As it would be expected, on the second pass the maximum temperature is higher, since the heat input is approximately the same in both cases, but the initial temperature is higher in the second pass due to insufficient cooling between both passes.

Temperature distribution on the FS tool is captured by infrared thermography. Figure 8 shows some of the captured frames.

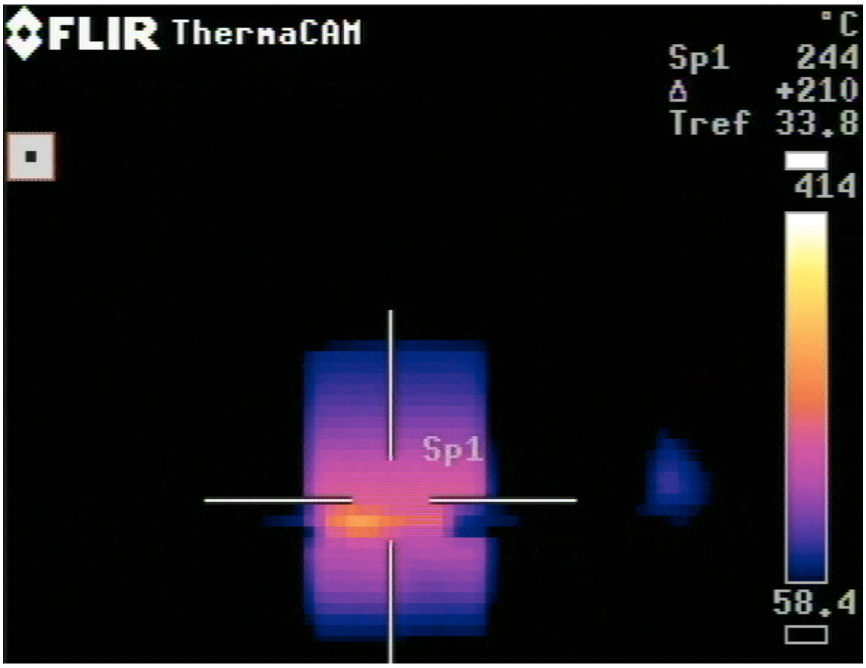

Fig. 8 a) - infrared thermography frames - FS tool, 10 seconds

As can be seen, slightly higher temperatures are measured on the retreating side.

Fig. 8 b) - infrared thermography frames - FS tool, 20 seconds

As it can be verified easily, the camera has a very low resolution for the distance at which it was used. In the next tests, the camera should be positioned closer to the tool.

After about 20 seconds, the tool reaches the center of the plate, where thermocouple measurements are taken; the whole tool has reached high temperatures.

Introducing these images into a MATLAB routine [Annex B] the temperature distribution may be presented as in Figure 9.

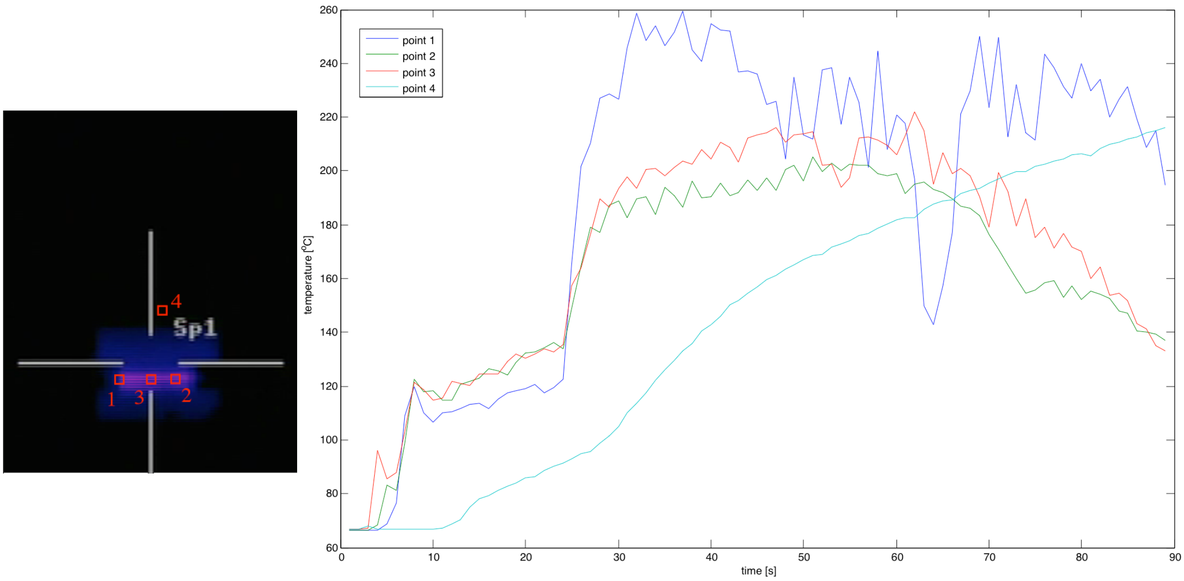

Fig. 9 - evolution of the temperature at 4 points on the tools surface

At the beginning of the temperature acquisition process the tool just touches the plate, and therefore the temperature is low. The next step corresponds to the penetration of the material by the tool. After that the tool advances, and heat is generated by the plastic deformation of the base material and the friction of the shoulder on the plate surface.

The temperature near the plate rises very fast and stays approximately constant throughout the welding. The decrease towards the end of the measurement is probably due to the fact that no more material is stirred in the end of the welding line, but only the shoulder contacts with the plate, so the thermal input is lower. It seems like a thermal equilibrium is found between the temperature of the tool, its heat dissipation and the heat input by the welding tool at the end of the plate.

On the retreating side higher temperatures are measured than on the advancing side, while the center of the tool has temperatures between both sides. Maximum temperatures of are 260ºC where recorded near the plate. It should however be noted that these temperatures are not necessarily of the tool itself, but can be from barb that moves in front of the tool during the process and is also acquired by the camera.

It could be seen from this analysis, that even if the resolution of the available thermal imaging equipment is low, some interesting conclusions may be drawn as to the distribution of the temperature on the FS welding tool.

Test C - thermocouples and FBG sensors with different gluing methods

A third test with a National Instruments (NI) SCXI-1001 using strain gauges and thermocouples was also performed at an acquisition rate of 1 kHz. At the same time FBG sensors were used with a BraggMeter fiber sensing device capable of acquiring at a rate of 1 Hz in order to compare the performance of both measuring devices.

The main goal of this test is to determine wether the bonding method influences the obtained result. The FBG sensors were bonded in two different ways with the same cyanoacrylate based adhesive for comparison. Completely bonded and only bonded on their tips.

Figure 10 shows the instrumentation scheme for the FS weld. The red arrow indicates the direction of welding. 12 thermocouples and two strain gauges are used.

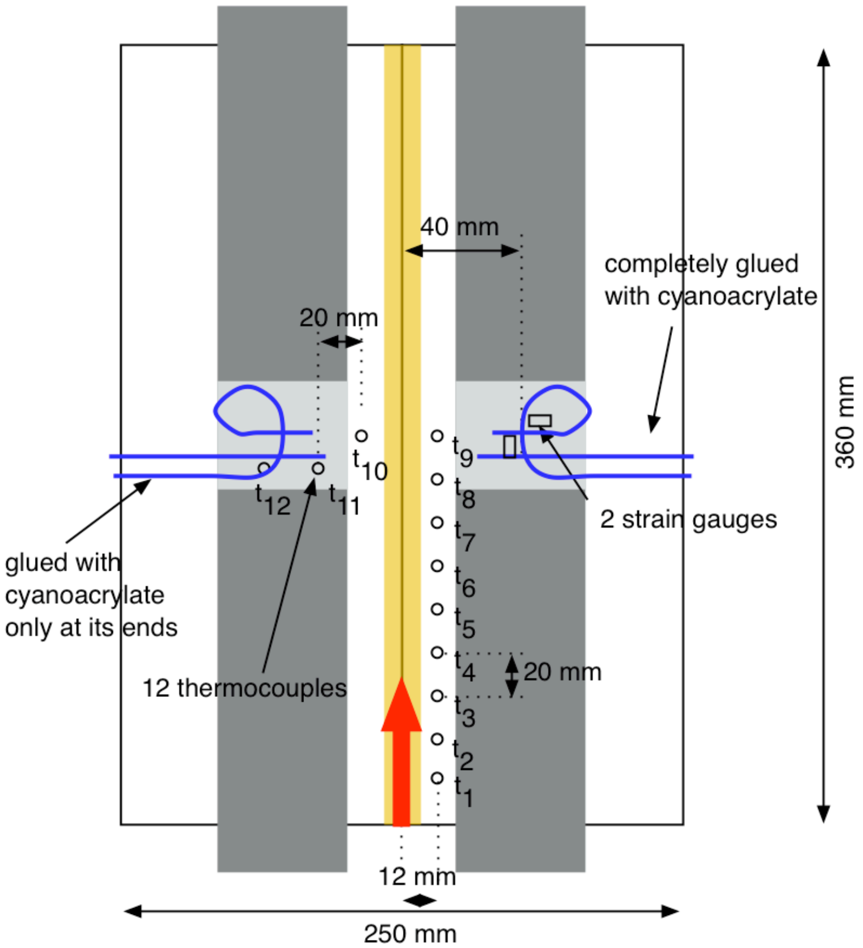

Fig. 10 - instrumentation scheme for FSW

FBG sensors are bonded in two different manners in approximately the same location on symmetric points relative to the welding line in order to be able to compare both bonding methods. For validation one half of the plate is instrumented with strain gauges and thermocouples as shown in Figure 10.

Temperature measurements along the FS welding line can be seen in Figure 11.

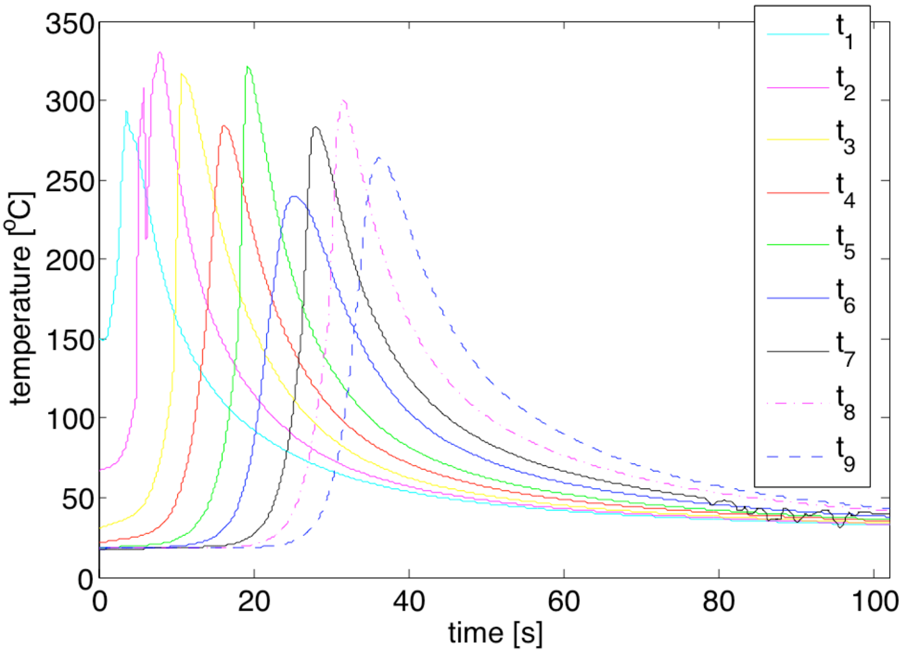

Fig. 11 - temperature measurements along the FS welding line

As it may be expected, the temperatures rise and fall progressively as the tool advanced in the welding direction from t_1 to t_9.

It should however be noted that no real tendency could be detected from one thermocouple to the next.

Perpendicular to the welding line, temperature was measured in the middle of the plate as shown in Figure 10. A representation of the obtained results can be seen in Figure 12.

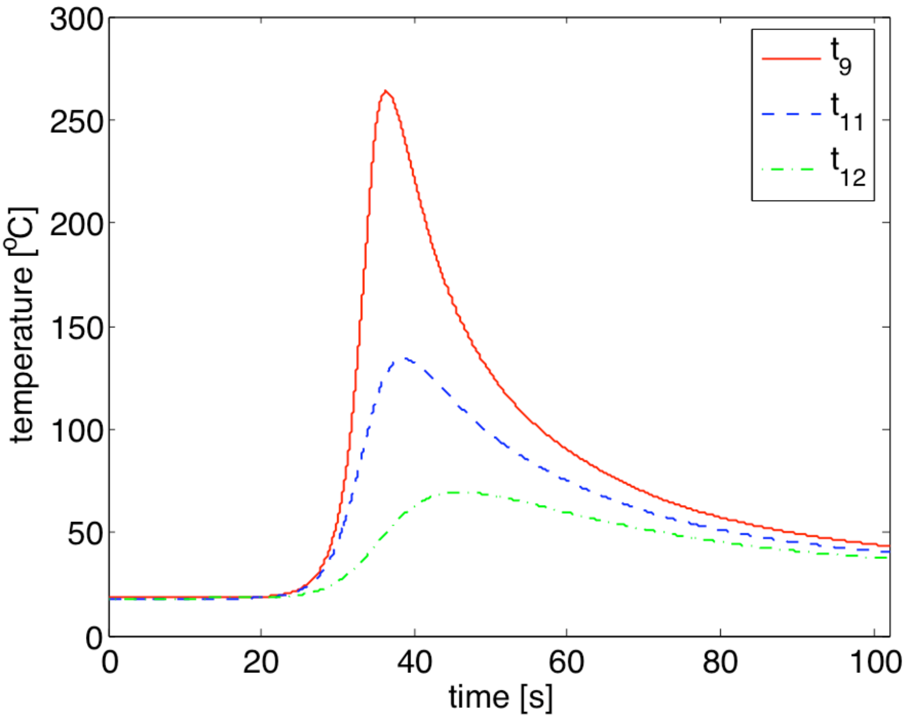

Fig. 12 - temperature measured using thermocouples at 12 mm, 32 mm and 52 mm for t_9, t_{11}, t_{12} respectively

Since one thermocouple had reading errors (t_{10}), its symmetric thermocouple (t_9) was used for this representation. No significant error is expected from this alteration. The temperature distribution measured follows the expected pattern; higher values are found near the welding line, and slower temperature increase rates are found with the more distant thermocouples.

The variation of the maximum temperature as a function of distance to the weld-center is represented in Figure 13.

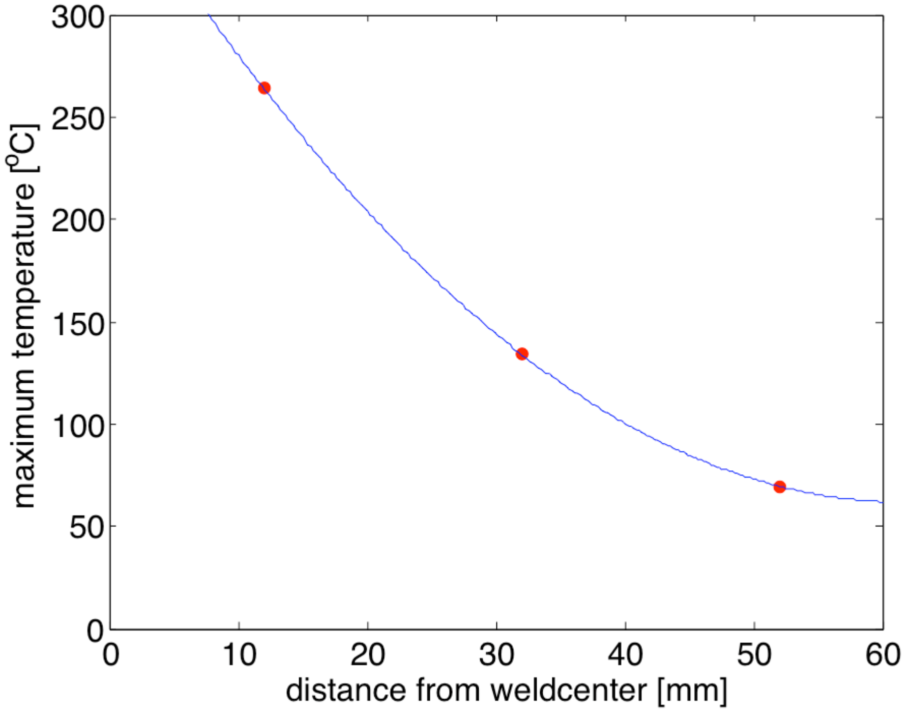

Fig. 13 - maximum temperature measured as a function of the distance to the weld-center

Figure 14 compares the temperatures measured by both symmetric thermocouples (t_9 and t_{10}).

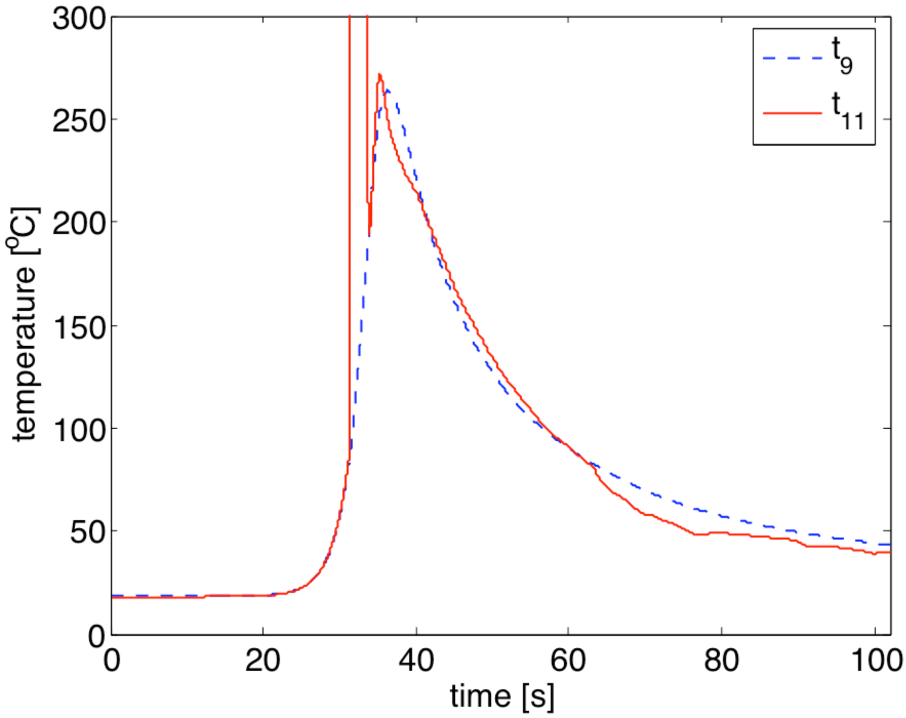

Fig. 14 - comparison of a good and a bad measurement result at two symmetric points

It may be noted that while the failing thermocouple approximates the good thermocouple quite well after its peaks, the shape of the curve is not perfect and should therefore be disregarded.

FBG sensors were also used on this plate using two different bonding methods. Figure 15 shows the obtained results at 40 mm from the welding line.

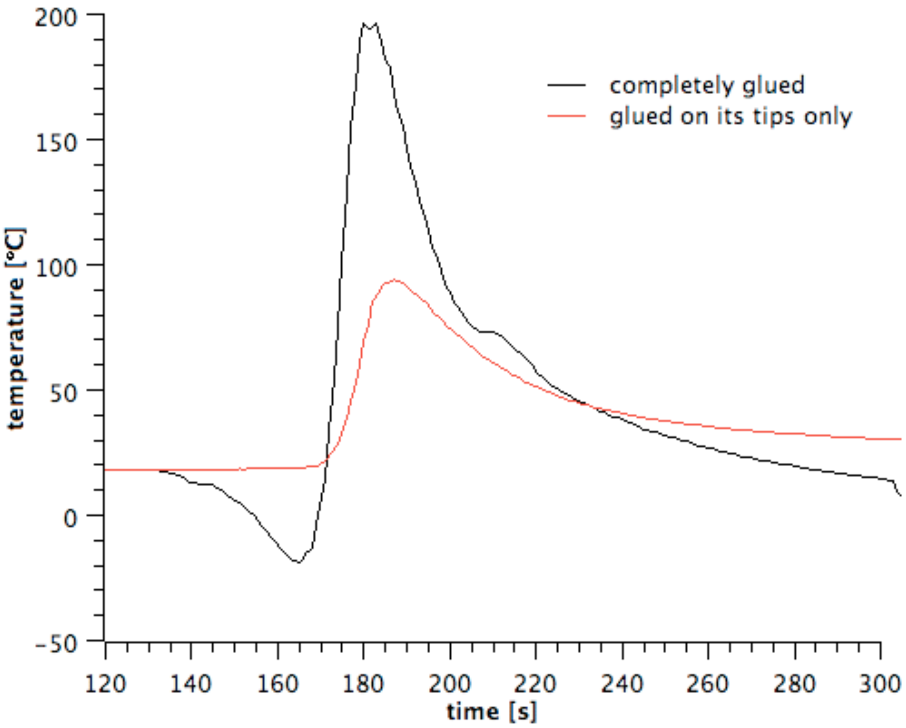

Fig. 15 - temperature measured using FBG sensors at approximately 40 mm distance from weld-center

As it could be verified in this tests, the FBG sensor bonded only at its tips shows a very reasonable result when compared to thermocouple measurements above. The completely bonded FBG sensor may not be used for temperature measurements, since the plate deformation influences the fiber deformation due to the adhesive.

Test D - thermal imaging of the tool and the plate

The main goal of this new thermal imaging test was to obtain better measurements of the tools surface temperature than in Test B. The camera is pointed perpendicular in the tools radial direction.

Figure 16 shows the evolution of temperature on 4 points of the tool.

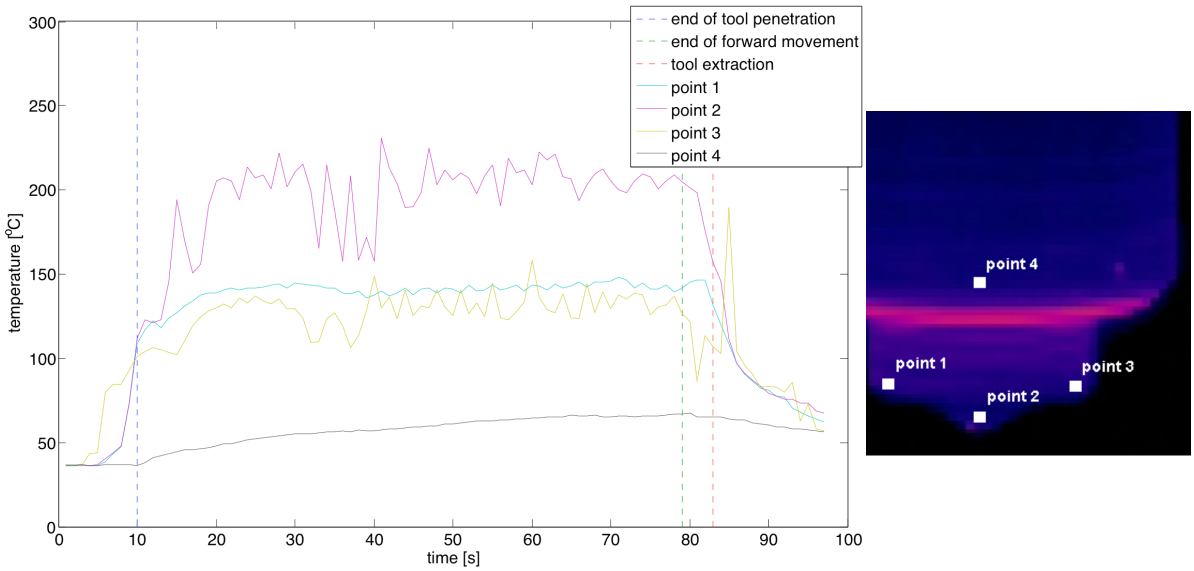

Fig. 16 - temperature evolution on four notable points of the FSW tool

It should however be noted that the temperature variation shown above is the temperature variation of the captured surface, which means that some of the welded material is also captured as it leaves the tool, especially on point 1 due to the clock-wise rotating direction.

As it can be seen in Figure 16, the temperature raises very quickly when the tool penetrates the material, and then stays approximately constant until the end of the welding. Because of the high thermal conductivity of Aluminium, the cooling time is also very short.

The short cooling time indicates a very local heating in contrast to the MIG welding process where cooling takes a long time, since the whole plate gets very hot as will be seen later on.

Slightly lower temperatures than in test B are obtained, see Figure 9. One main reason for this may be the fact that the welding was done with less penetration of the tool, due to a thicker plate (3.01 mm vs 2.95 mm). The quality of the weld however did apparently not suffer from this reduced penetration, although no mechanical testing is performed on this plate.

The aluminium plate has also been captured. Figure 17 shows one frame of the thermal imaging video.

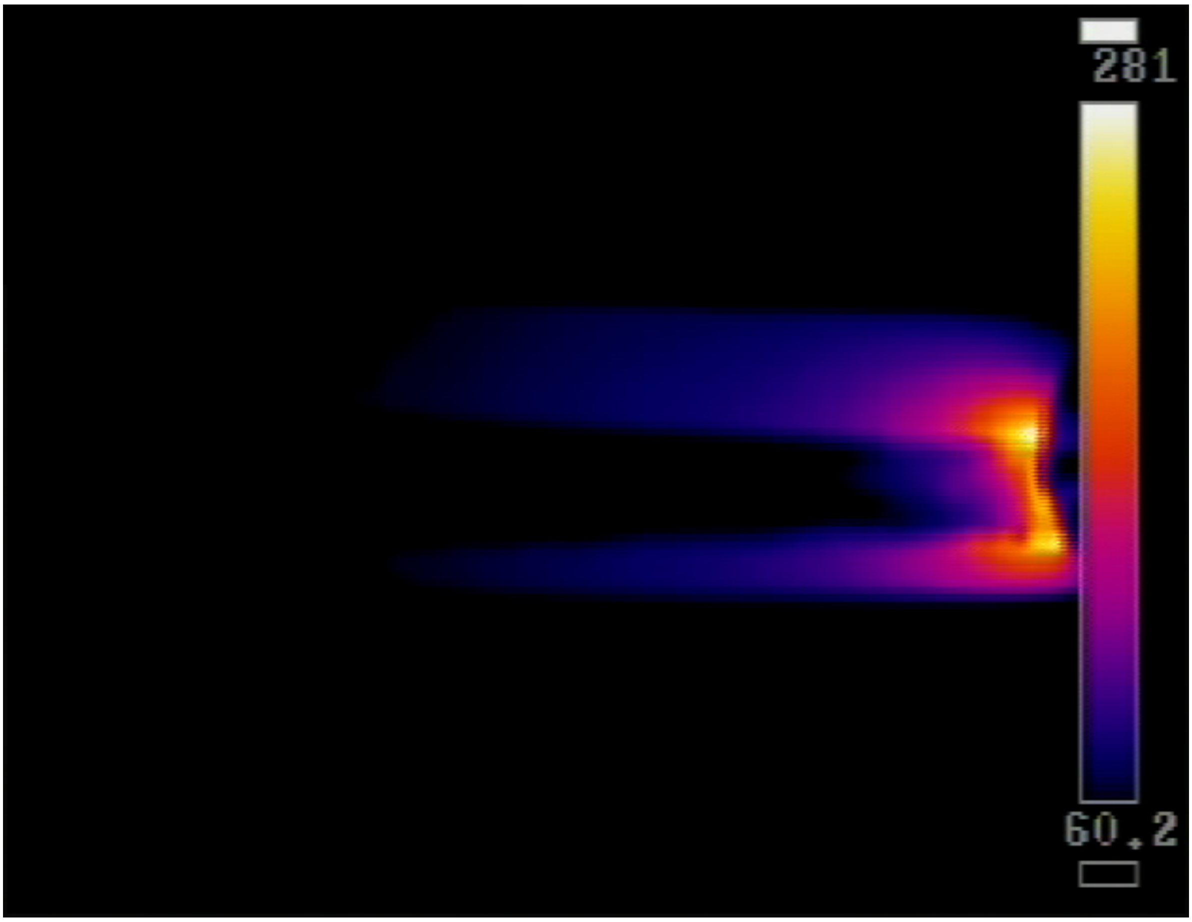

Fig. 17 - frame captured by the thermal imaging device on the plate during welding

While no quantitative information should be taken from Figure 16, some interesting facts can be seen. Isothermal lines may be drawn around the welding tool, keeping in mind that the reduced temperature measured in the center of the image is due to the different reflectivity of welded Aluminium from the black painted surface around it where no welding tool passes. It can very easily be seen that the temperature falls very quickly as the tool passes.

Test E

The main goal of this test is to try to validate different adhesives. Therefore the fibers intended to measure strain are bonded in duplicate, using two different adhesives; one cyanocrylate based, and the other a epoxy based structural adhesive with higher temperatures of usage.

As was already verified in test C, the better bonding method seems to be to only bond the tips of the fibers for temperature acquisition. For strain acquisition, this rule has still to be verified.

A fuse is also used for determination of the start of the welding. The goal is to synchronize the optical and electrical signals. Since the forward movement of the tool is less than 5 mm/s, the cables used as fuse did not brake immediately. For further tests, it would be recommended to use a simple opto-electronic sensing device for tool detection, which gives the same trigger signal to both acquisition systems.

The instrumentation scheme is represented in Figure 18.

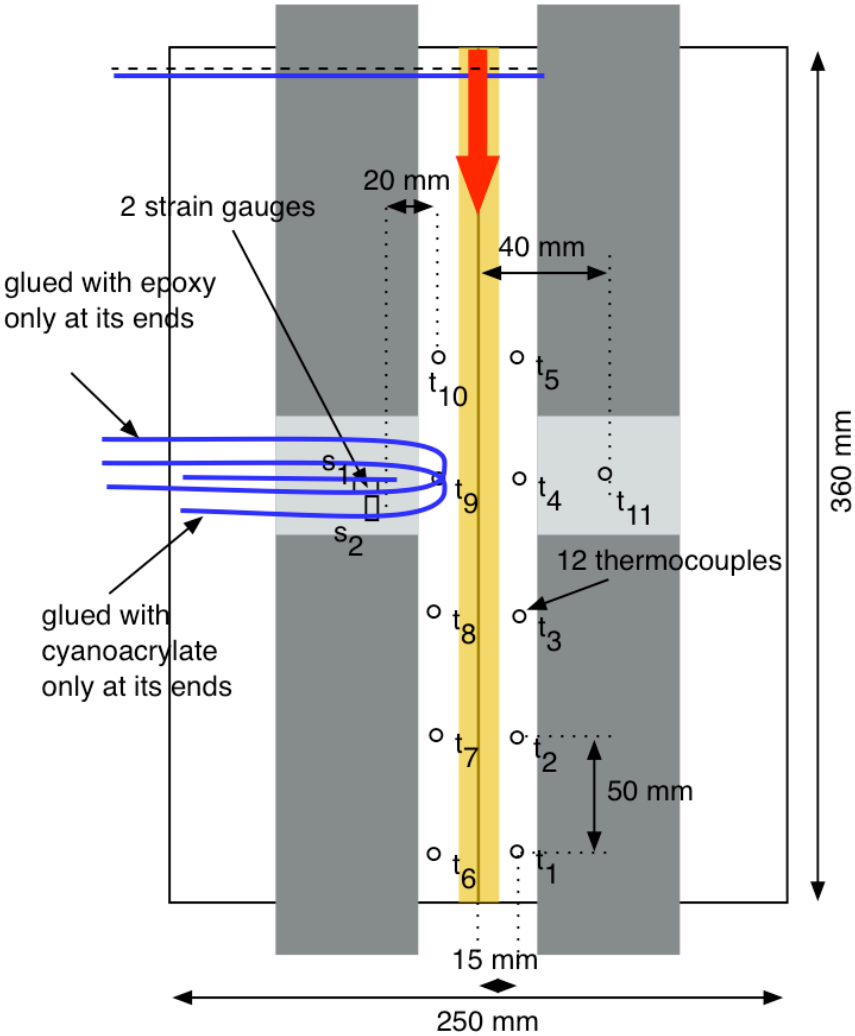

Fig. 18 - instrumentation scheme for comparison of two glue types

Temperature was measured along the welding line on symmetric positions in order to verify each measurement, since it is to be expected that the temperature variation is approximately symmetric. Temperature is also measured at 40 mm distance from the weld-center, where strain gauges are applied and FBG sensors are used. The strain gauges are used for FBG sensor verification, and for comparison with the results obtained in Test C.

The mean temperature of symmetric thermocouples along the welding line is represented in Figure 19.

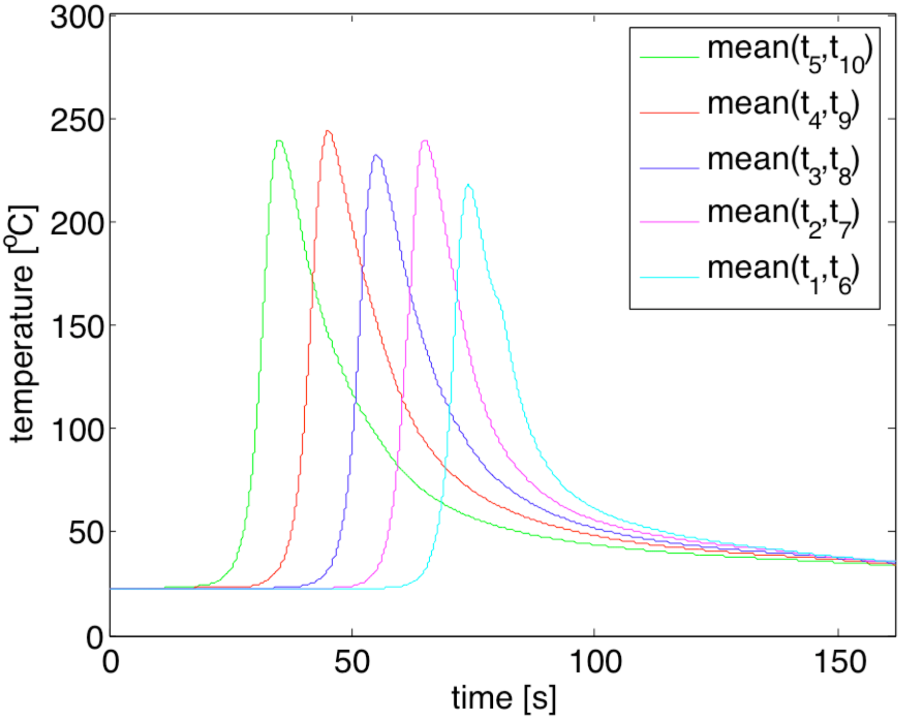

Fig. 19 - mean temperature of thermocouples along the welding line at 15 mm distance from the welding line center

It can easily be seen that the temperature gradient for growing temperatures is equal for all thermocouples. The maximum temperature is not equal, but very similar. The plate cools down very fast and below 50ºC almost uniformly across the whole plate .

The temperature on the advancing and retreating side of the FS weld is represented in Figures 20 and 21 respectively.

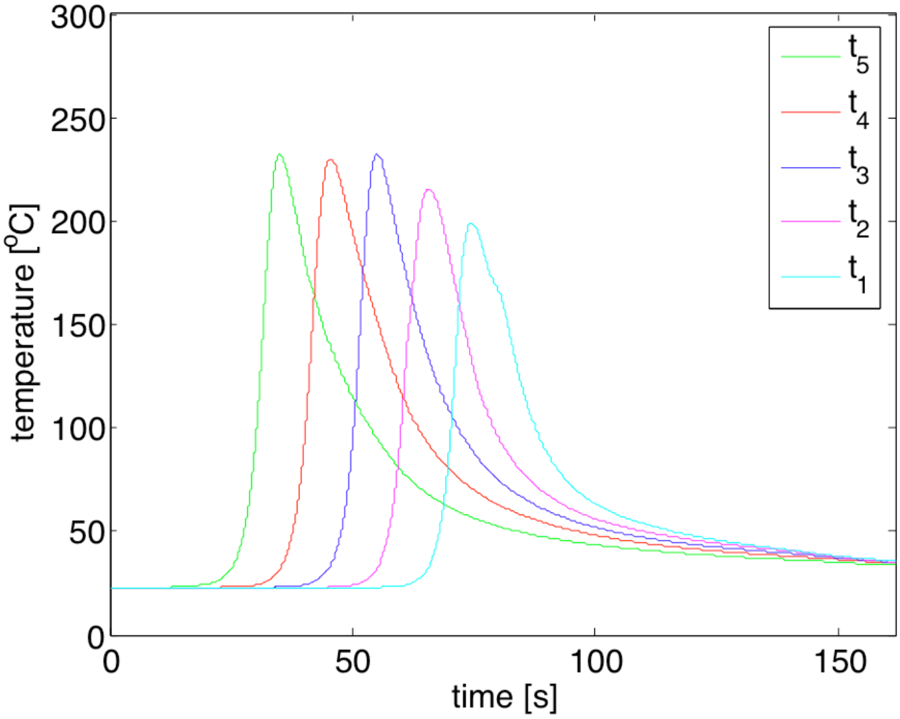

Fig. 20 - temperature variation along the welding line - advancing line

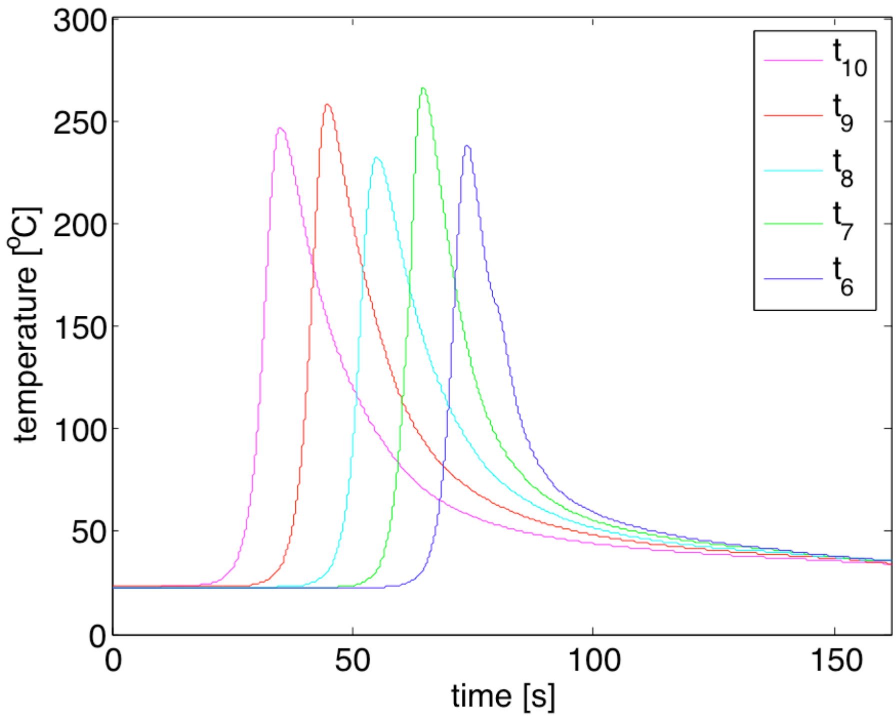

Fig. 21 - temperature variation along the welding line - retreating line

Slightly higher temperatures are measured on the retreating side, which may be explained by the higher relative velocity of the tool to the plate in contrast to the advancing side, where the tool tangential velocity is in the same direction as the plate movement.

At least on the advancing side, a slight tendency of measuring lower peak temperatures in the direction of the welding can be seen. Since this variation is very low in relation to the expectable error magnitude not too much attention should be paid to this phenomenon. Further test are necessary for its verification.

The temperature perpendicular to the welding line is represented in Figure 22. This data may be used for comparison with FBG sensor results presented later on.

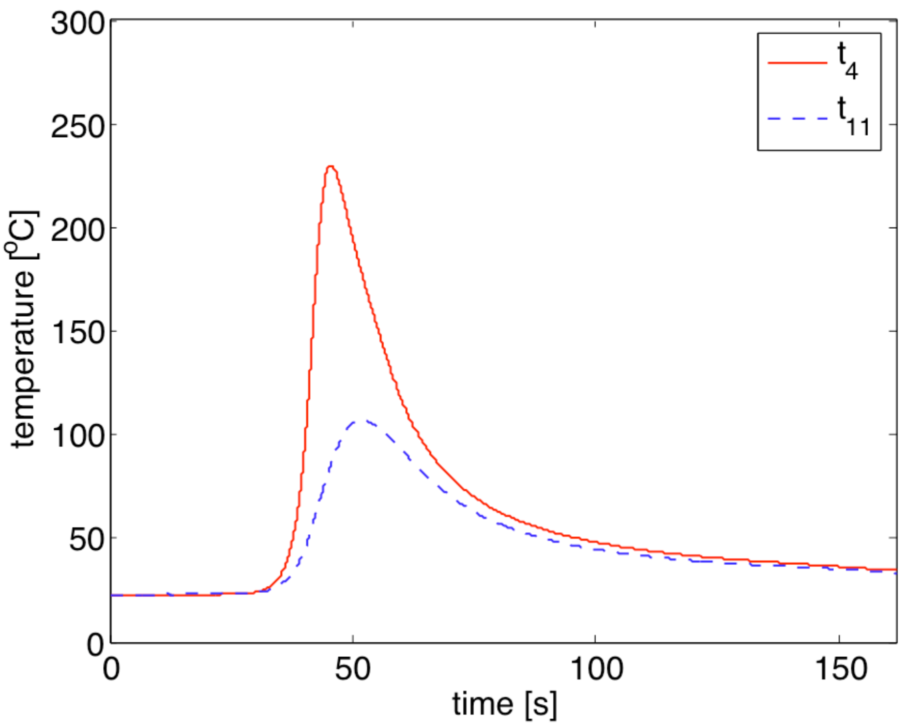

Fig. 22 - temperature variation on positions perpendicular to the welding line

The same temperature variation measured at 40 mm distance from the welding line center using FBG sensors is represented in Figure 23 on a symmetric position.

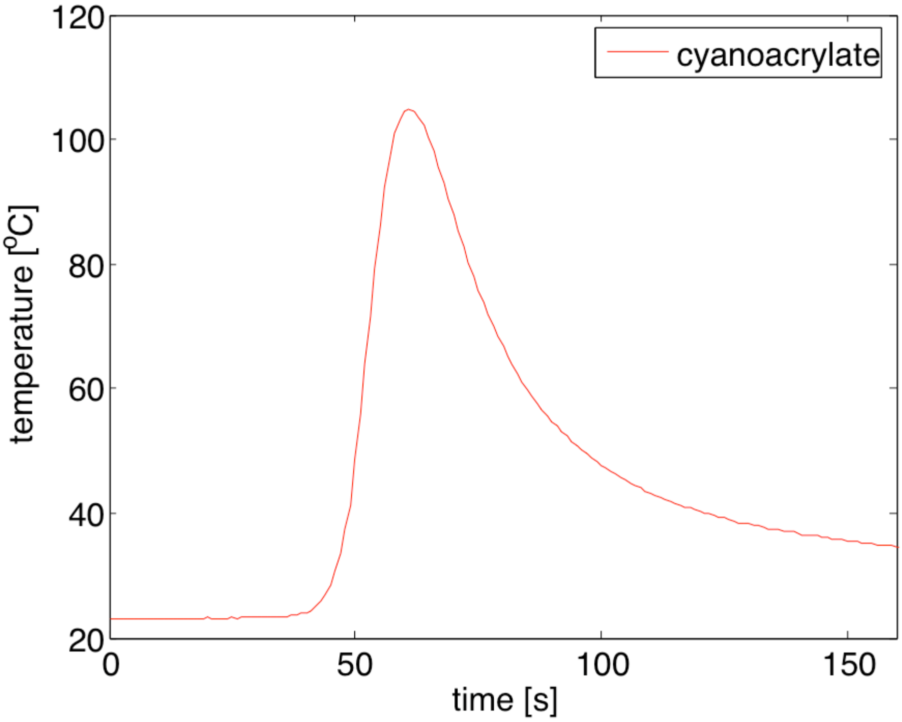

Fig. 23 - temperature variation measured at 40 mm from welding line using FBG sensors

The maximum temperature is very similar using both measuring techniques (see Figure 22, t_{11}). The temperature gradient seems to be captured adequately with both measuring techniques. The idea can therefore be reenforced that FBG sensors are capable of measuring temperature variations using a fiber glued only at its tips using simple cyanoacrylate glue, which dries fast and glues on almost every surface, since no force other than holding the fiber in place is required from the glue.

2.2.2. MIG

Temperature distribution during MIG welding was analyzed with two distinct methods: thermocouples and FBG sensors. Two tests are made, test A and test C.

Test A - thermocouples and FBG sensors

A first test was made with thermocouples and FBG sensors measuring temperature, and only FBG sensors measuring strain in the direction parallel to the welding line. Figure 24 shows the instrumentation scheme for this test.

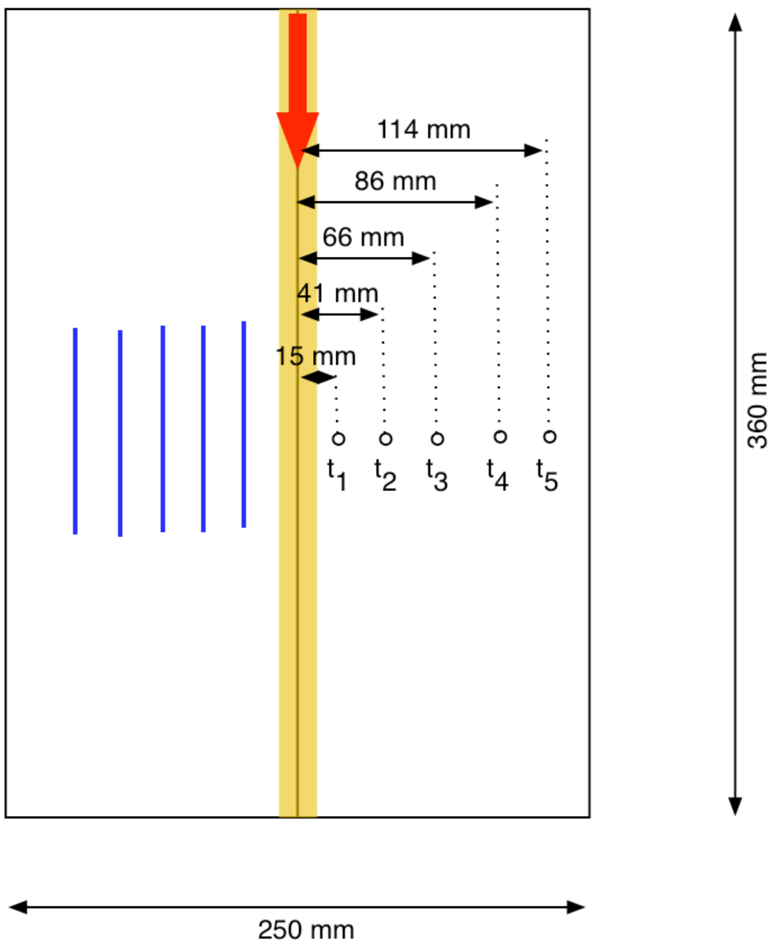

Fig. 24 - instrumentation scheme for the first instrumented MIG welding test

Results for thermocouples may be found in Figure 25.

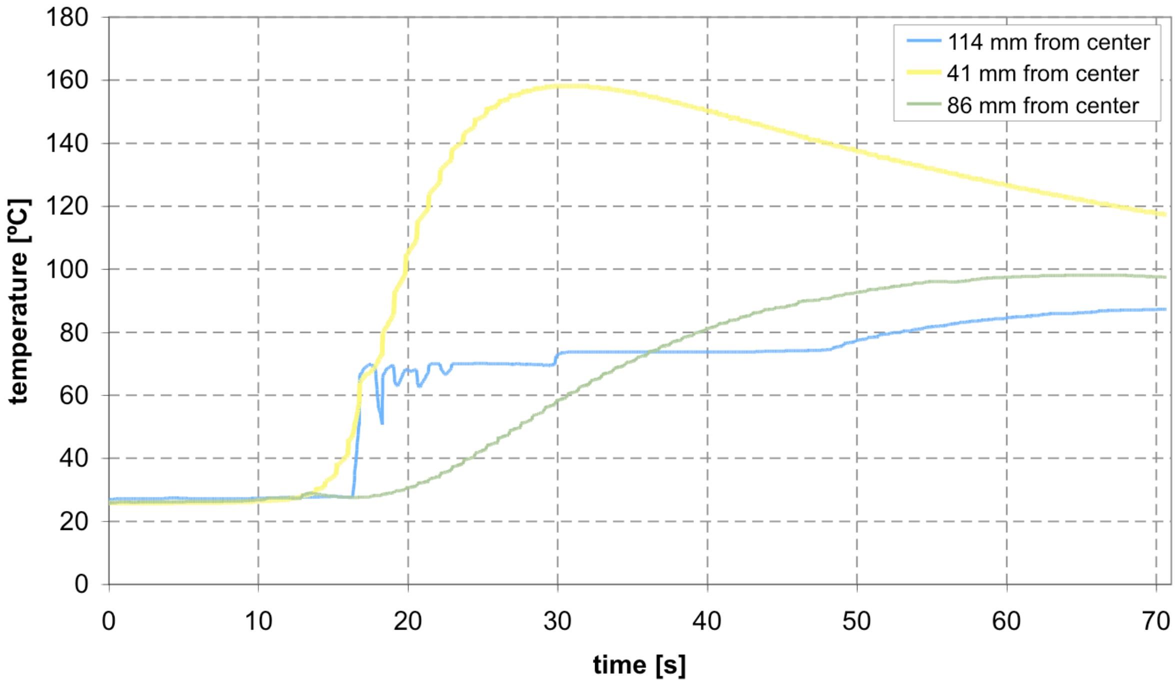

Fig. 25 - temperature measured using thermocouples

Since part of the thermocouples failed, only some results can be shown here. The device at 114 mm distance from the welding line is shown because it only failed partially, showing an important part of the curve.

Fiber Bragg grating sensors have been used to acquire temperature at symmetric positions from the thermocouples shown above. In Figure 26, temperature measured by FBG sensors is presented.

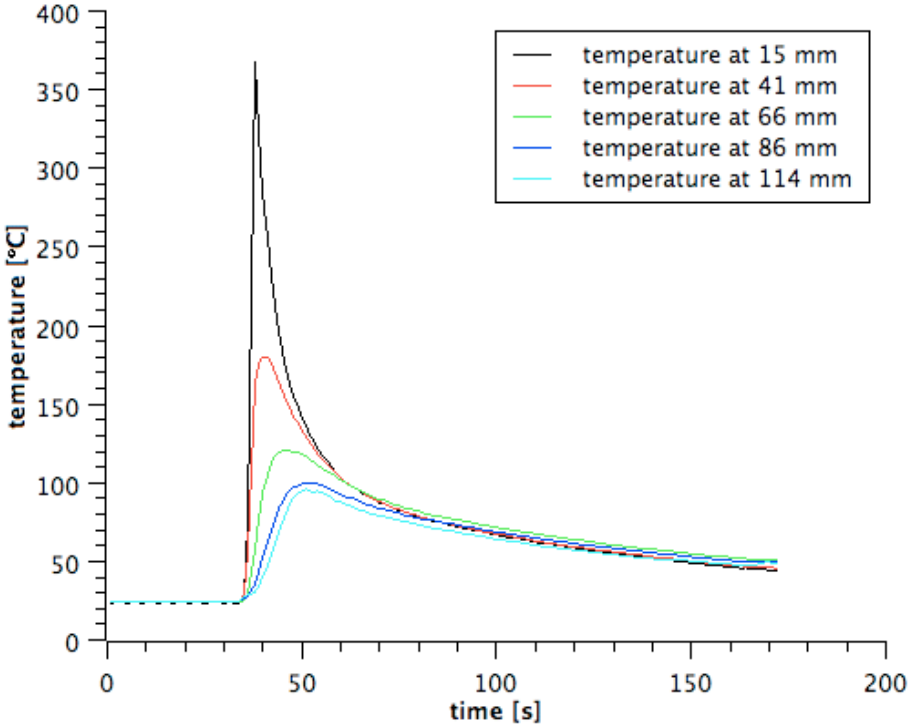

Fig. 26 - temperature measured using FBG sensors

Some differences can be found between both measurements, but both results seem to be realistic. A higher acquisition rate than 1 Hz would be preferred for FBG sensors for caption of temperature peaks.

One interesting result of these tests is that all sensors measure a relatively high temperature after the welding process. This means that in opposition to FS welding, the MIG welding process generates enough thermal energy to heat the whole plate.

In order to clarify some aspects of the use of FBG sensors, like the best way to guarantee contact between the sensors and the plate more tests are made.

Test C - thermocouples and FBG sensors with different gluing methods

Figure 27 shows the instrumentation scheme used used for the MIG weld. The red arrow indicates the direction of welding.

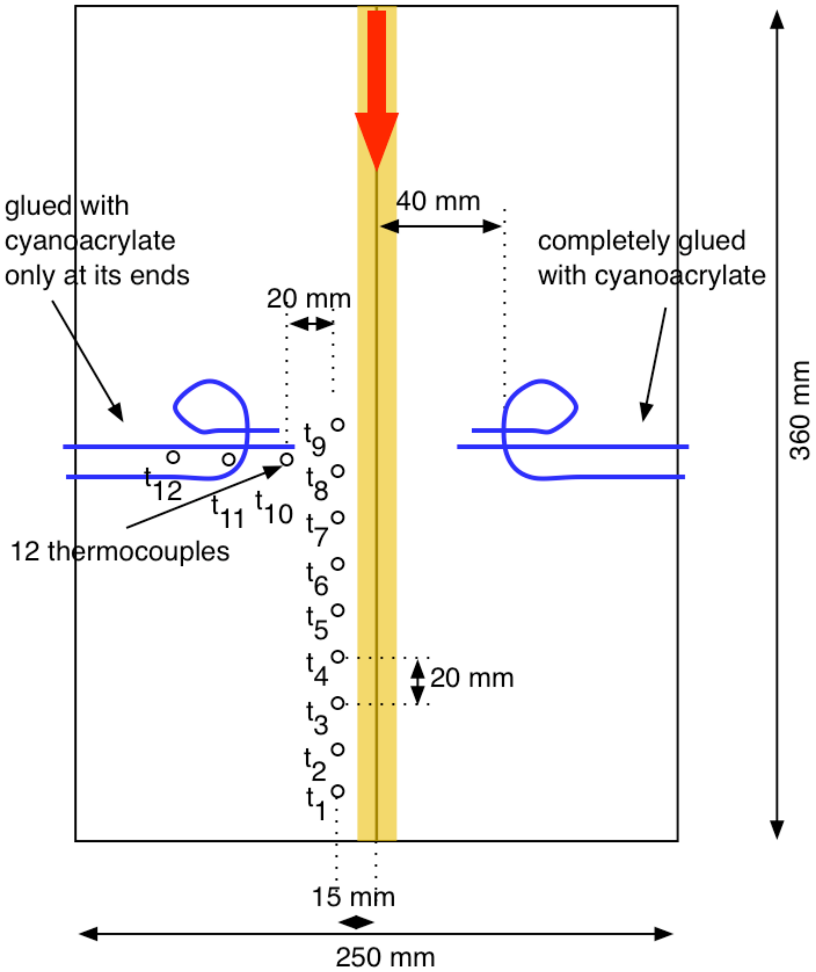

Fig. 27 - instrumentation for comparison between two gluing methods - MIG welding

The FBG sensors on one side are bonded in all their measuring extend, on the other only the tips of the measuring part of the fibers are bonded. Strain is measured in two perpendicular directions at two symmetric points of the plate using FBG sensors only. Strain gauges could not be used due to the high temperatures of this welding process. Thermocouples are used for temperature measurements on the same plate as shown in Figure 27.

The temperature distributions for MIG welding parallel and perpendicular to the welding line are shown in Figures 28 and 29 respectively.

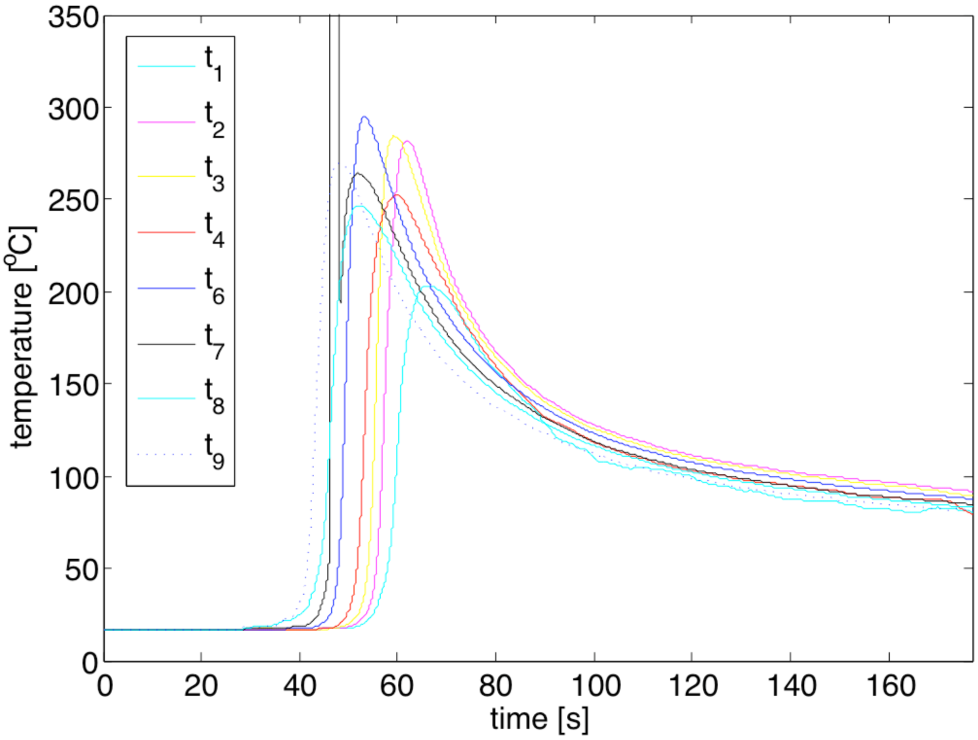

Fig. 28 - temperature measurements parallel to the MIG welding line

The temperature rises and falls as expected along the welding line from t_9 to t_1, but no clear tendency of variation between the thermocouples could be found.

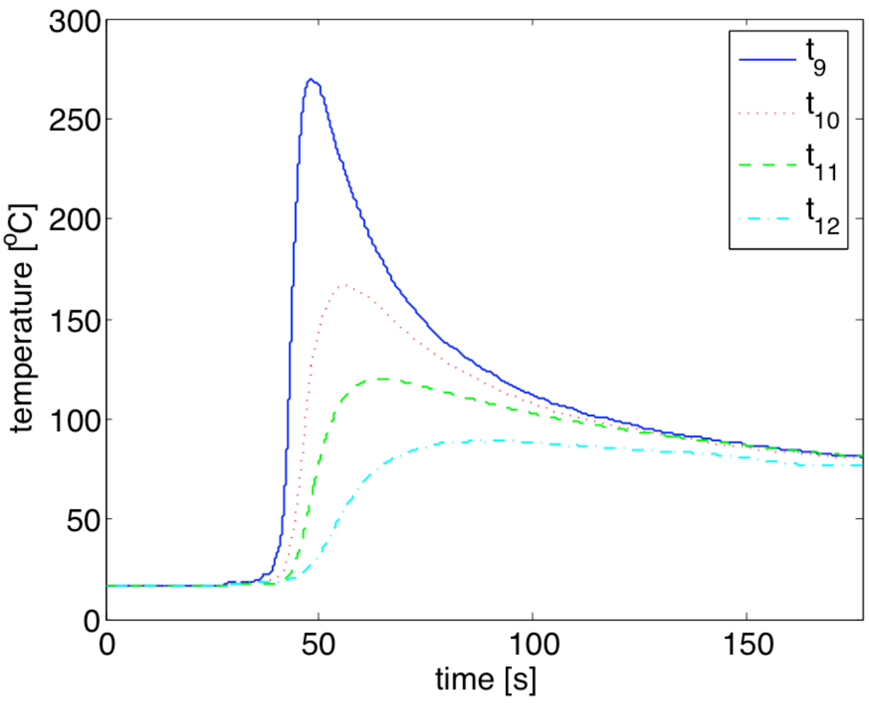

Fig. 29 - temperature measured using thermocouples at 15 mm, 35 mm, 55 mm and 75 mm for t_9, t_{10}, t_{11}, t_{12} respectively

Figure 29 shows that the temperature rising rate is lower on thermocouples which are more distant from the welding line. The temperature falls to the same level on all points very shortly after the torch passes the measuring point but takes very long to reach room temperature again. Figure 30 shows the evolution of maximum peak temperature as a function of distance to the center of the welding line.

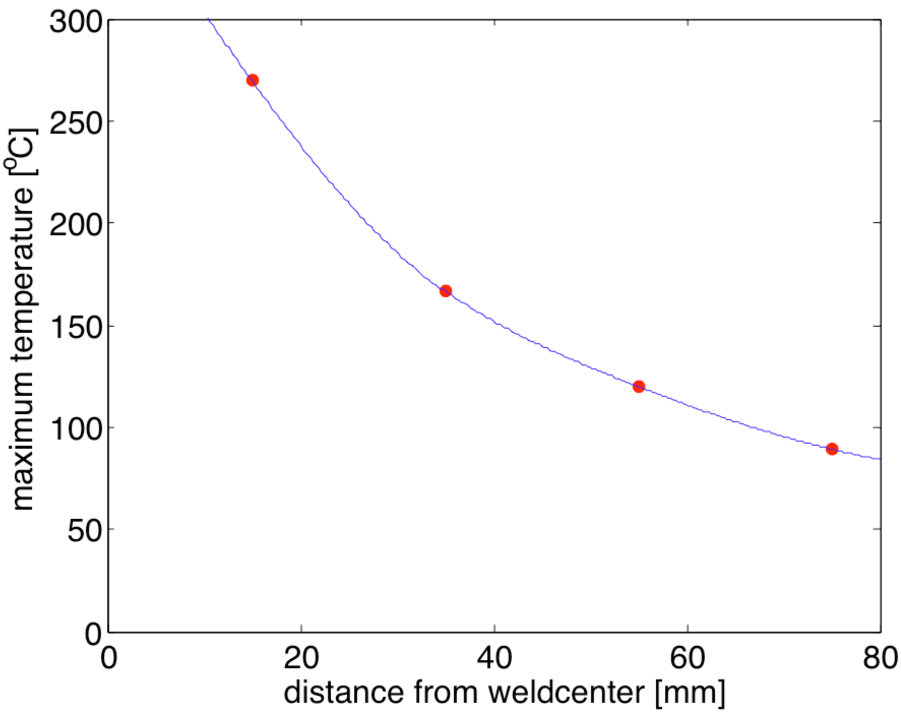

Fig. 30 - maximum temperature as a function of distance to the weld-center

FBG sensor results are given in Figure 31 for a distance of 40 mm from the welding line in the center of the plate.

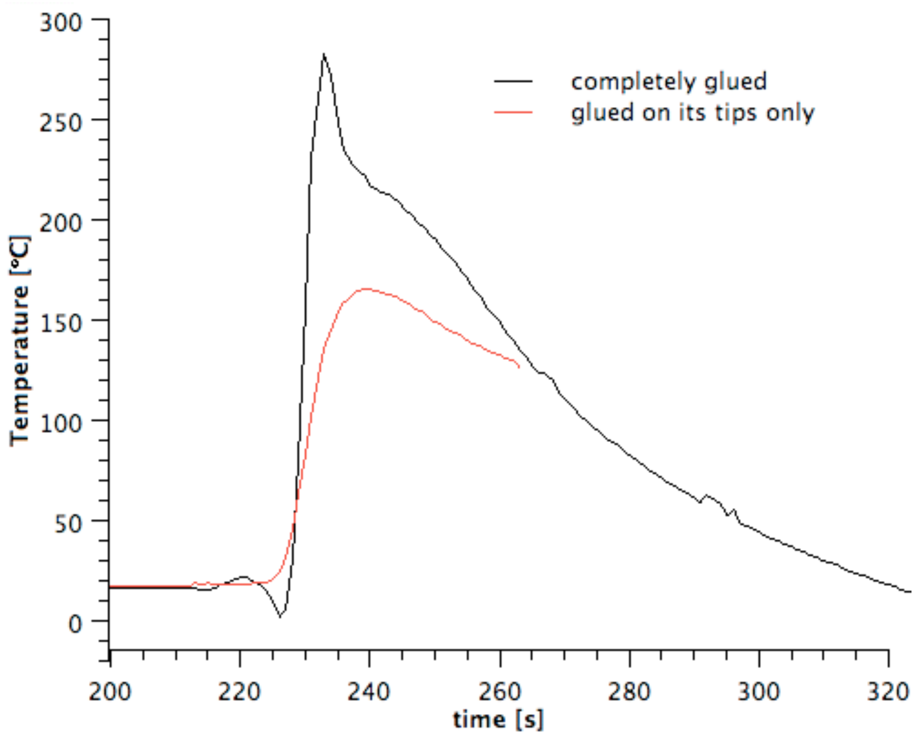

Fig. 31 - temperature measured using FBG sensors at approximately 40 mm distance from weld-center

The FBG sensor that was only bonded at its tips is perfectly comparable to the thermocouples, see Figure 30 for a comparison of maximum temperatures. The completely bonded FBG sensor may not be used for temperature measurements.

In MIG welds the thermocouples and FBG sensors have to be protected against the very high temperatures present during welding and the strong radiation created by the welding arc.

Since no common zero in terms of time was defined during the tests, the absolute measured time should not be directly compared. Further test with a defined common zero should be defined in order to be able to conclude on a possible delay of one of the sensor types. If no delay is detected, a common zero may be selected by analyzing the obtained temperature variations.

2.3. Deformation created by welding processes

2.3.1. FSW

Test A - FBG sensors

In the first tests, the instrumentation scheme of Figure 4 was used. Only FBG sensors where used for strain measurements perpendicular to the welding line at 4 different distances. Figure 32 shows the obtained results.

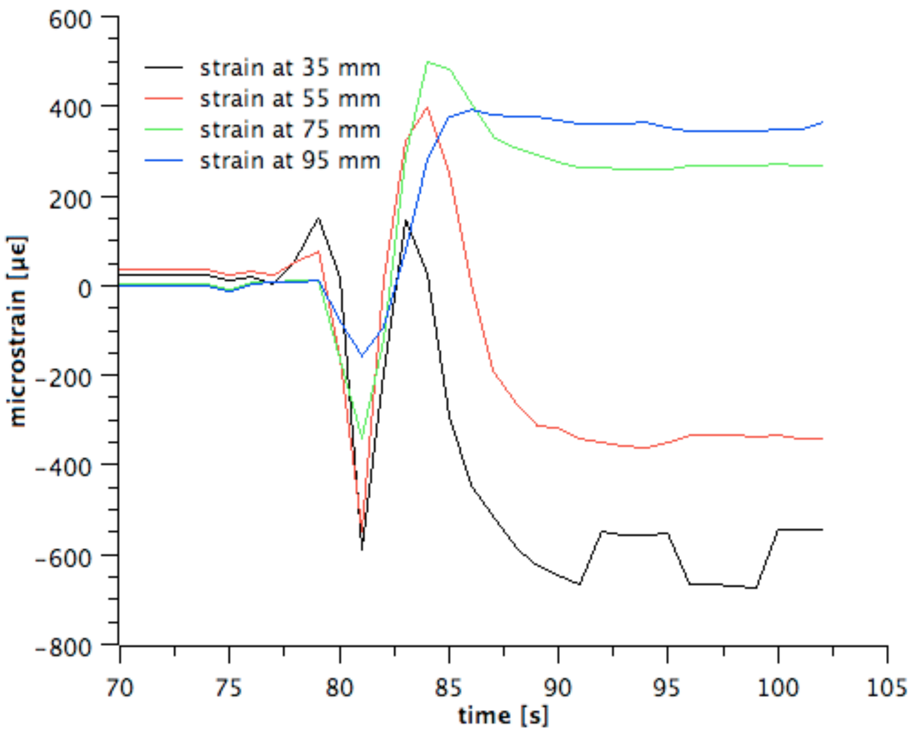

Fig. 32 - strain perpendicular to the FS welding line acquired by FBG sensors

Two important comments have to be made. First of all, the magnitude of the measured deformation has to be verified by some well understood method like for example by the use of strain gauges. Secondly, compressive stresses are verified in the moment when the tool passes the FBG sensors. A reasonable explanation for this effect seems to be the fact that the tool is squeezed between to plate halves which are heavily restrained, so no relative movement is possible. Only the compression of each plate half in the moment when the tool passes seems to happen.

Test C - strain gauges and FBG sensors with different gluing methods

Strain measurement is also performed with two different methods. Well established strain gauge technique is used for validation of FBG sensor results. FBG sensors are bonded using two different methods. Only the tips of the sensors measuring areas are bonded on one side, and the whole fibers are bonded in the other. The instrumentation scheme can be seen in Figure 10.

Strain is acquired in the center of the plate, at a distance of approximately 40 mm from the welding line in two perpendicular directions.

Figures 33 a) and b) show the obtained results in terms of strain and stress in direction perpendicular and parallel to the welding line.

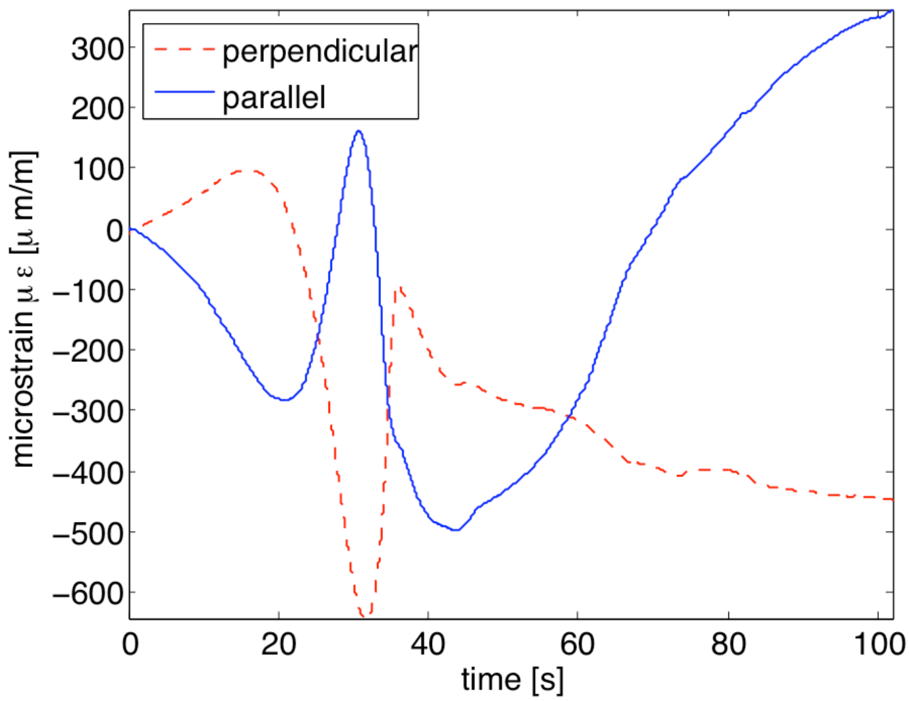

Fig. 33 a) - strain during FS welding measured using strain gauges perpendicular and parallel to the welding line at approximately 40 mm from weld-center

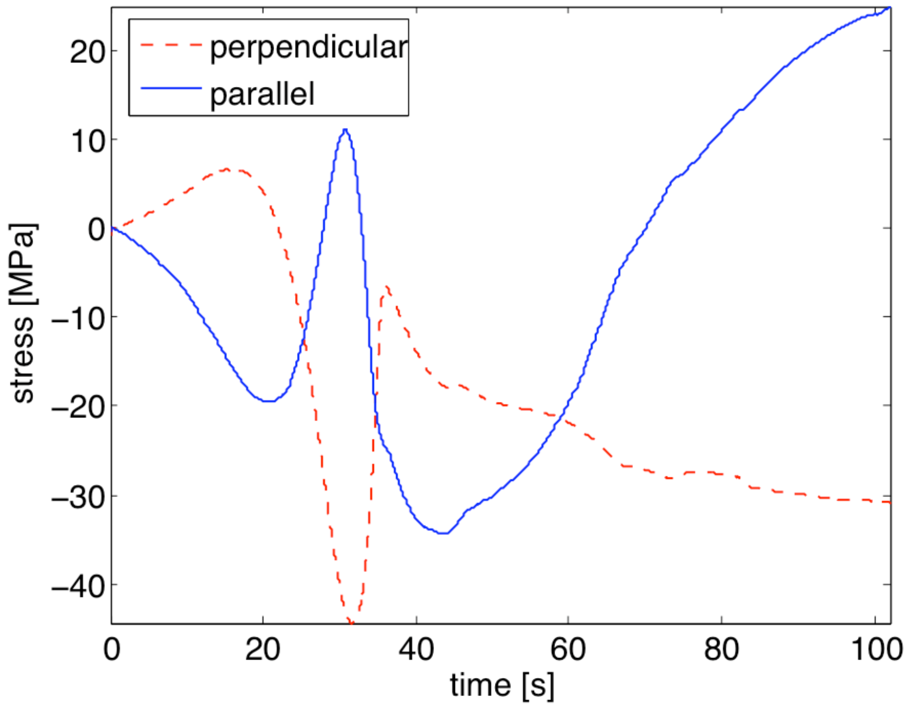

Fig. 33 b) - stress during FS welding perpendicular and parallel to the welding line at approximately 40 mm from weld-center

Measured stresses may eventually be related with residual stress measurements performed later on.

The peaks around 30 seconds happen when the tool passes the center where measurements are taken. Compressive stresses lower than -40 MPa are measured in the transversal direction, and maximum traction stresses of about 15 MPa are measured in the longitudinal direction.

More tests should to be performed to see the evolution of stress at different points and times in the welding.

FBG sensors have also been attached to the plate at 40 mm distance from weld-center. The measurements perpendicular and parallel to the plate with fibers only bonded at the tips are shown in Figure 34.

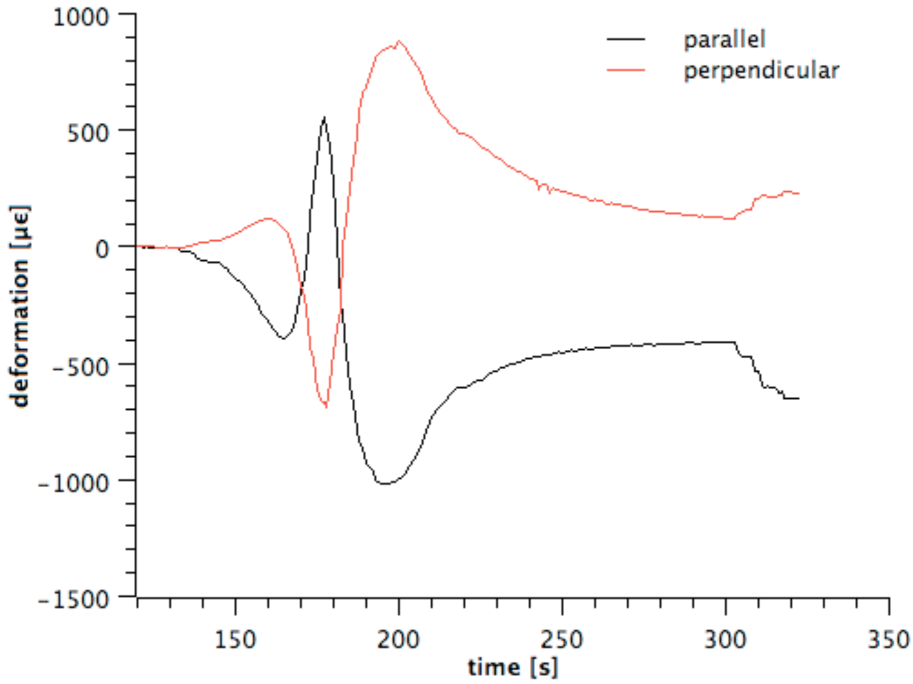

Fig. 34 - strain measured using FBG sensors glued only at their tips perpendicular and parallel to the welding line at approximately 40 mm from weld-center

The results presented in Figure 34 show a similar stress variation to the one measured using strain gauges, at least until short after the tool passes the center of the plate where measurements are taken. The magnitude of the measured deformations is not equal in both techniques; this difference has to be verified in further tests. The completely glued fibers broke during the test, and no information could be retrieved from them.

It was immediately verified during the welding tests, that the completely bonded FBG sensors did not perform well. A long response time and broken fibers were the result. It should also be noted that an adequate thermal insulation should be given because of the arc weldings high radiation. The best method for this seems to be to cover the sensors with silicon based thermal protection.

Test E - comparison of epoxy and cyanoacrylate

The instrumentation scheme may be seen in Figure 16. Strain was acquired with FBG sensors and strain gauges. The results obtained using traditional strain gauges are shown in Figure 35. As it can easily be seen, they are very similar to the ones obtained in test C using the same instrumentation.

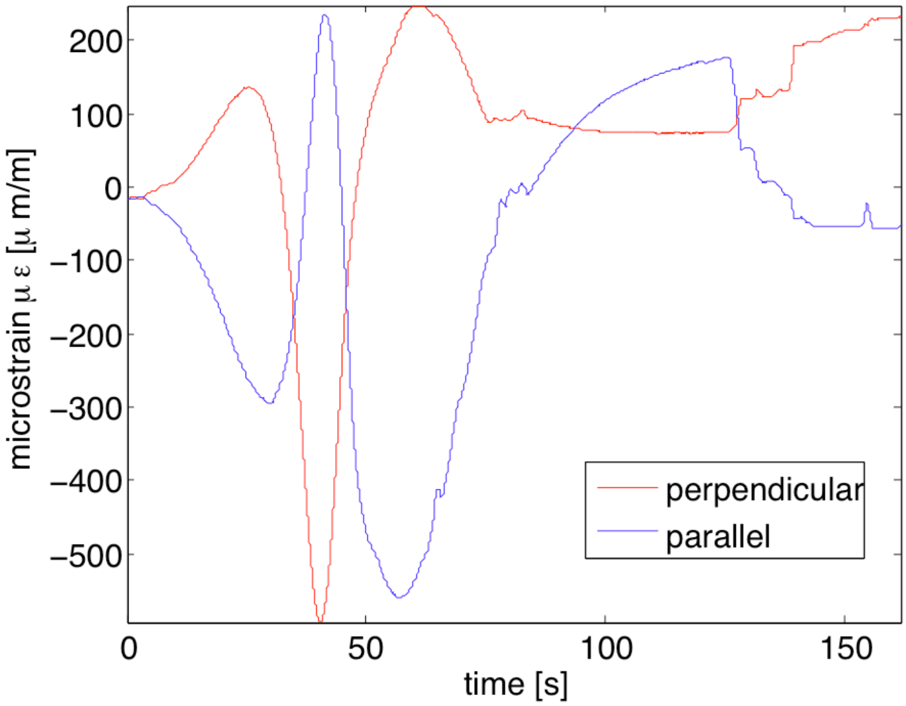

Fig. 35 a) - strain acquired using strain gauges at 40 mm distance from welding line center in two perpendicular directions - expressed as microstrain

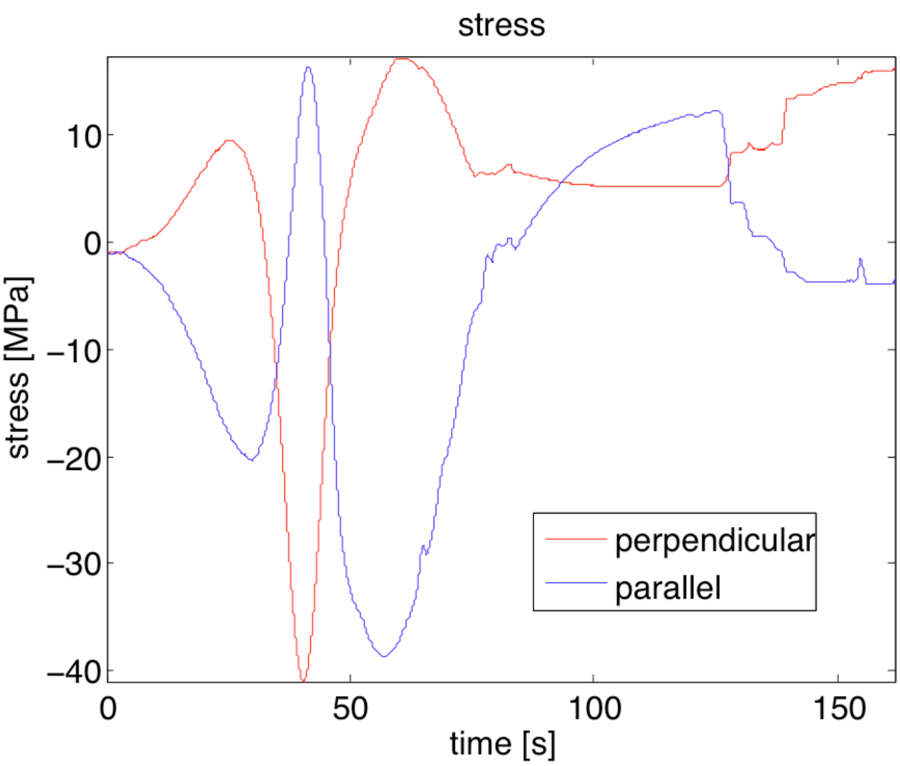

Fig. 35 b) - strain acquired using strain gauges at 40 mm distance from welding line center in two perpendicular directions - expressed as stress

The Figures above also show the relaxation of stresses when the fixation bars are removed from the FSW machine after about 120 seconds.

On the same location, FBG sensors are used for strain measurement in the perpendicular direction. Two different adhesives are used, and two measurements are made with each adhesive type in order to get results for comparison purposes. Only the tips of the fibers are glued onto the plate as was decided after seeing results of previous tests, but further experimentation has to be done. If the adhesive does not influence results, all four measurements should lead to approximately the same results. Figure 36 shows the obtained results for comparison.

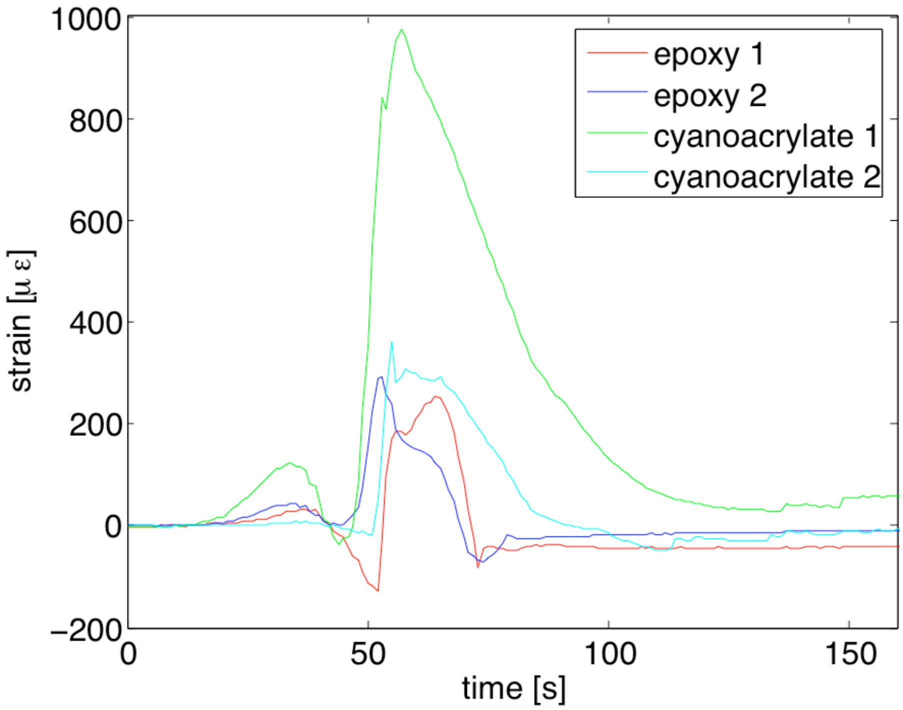

Fig. 36 a) - strain at 40 mm distance perpendicular to the welding line measured with FBG sensors

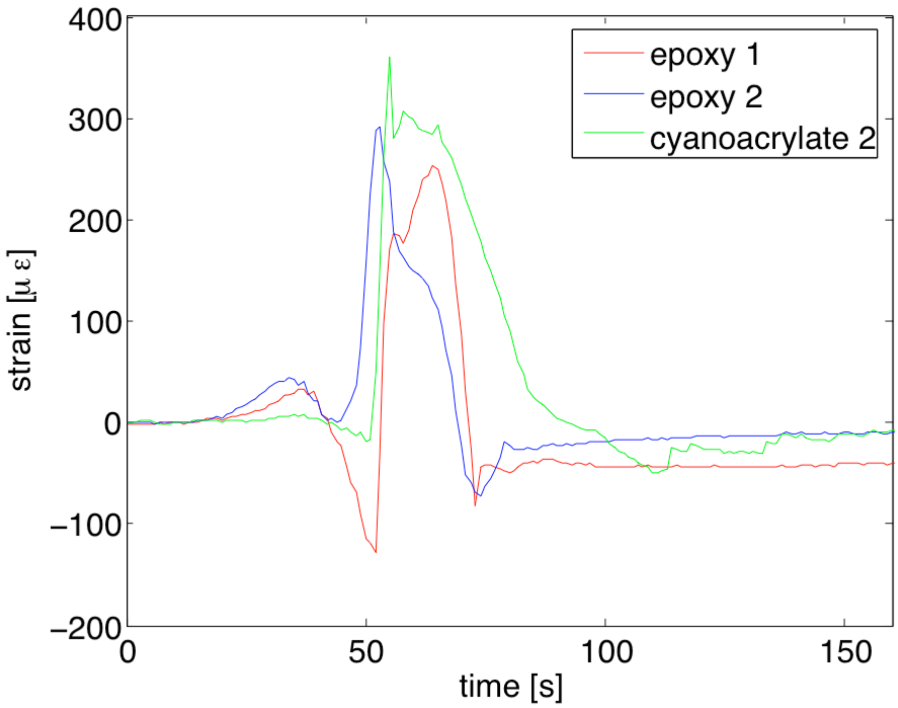

Fig. 36 b) - strain at 40 mm distance perpendicular to the welding line measured with FBG sensors, excluding the third sensor with high discrepancy to the other measurements

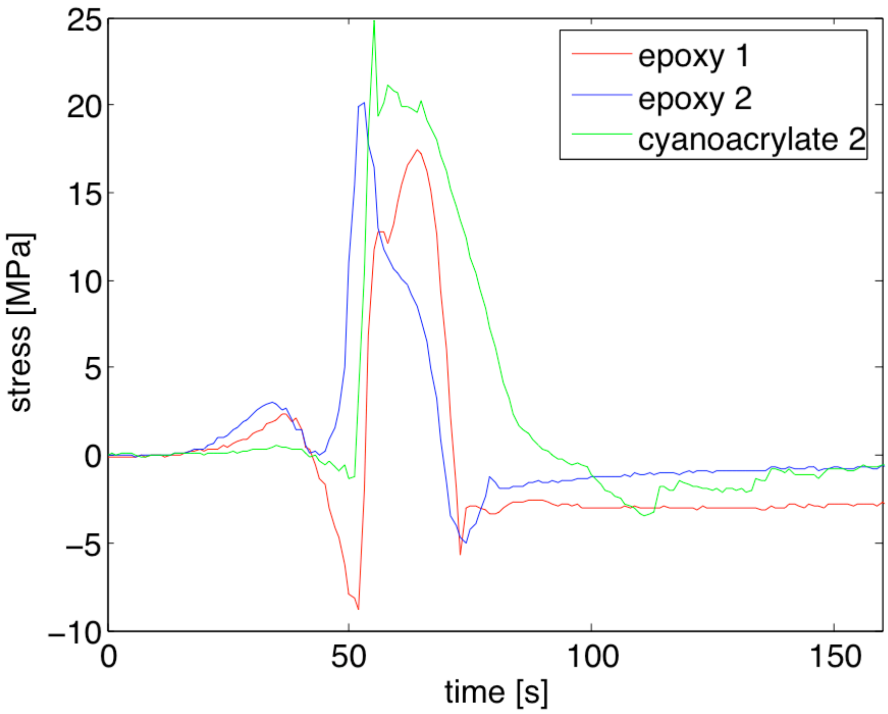

Fig. 36 c) - stress at 40 mm distance perpendicular to the welding line; calculated using Young's law from the results of Figure 36 b)

All four results are different, so no real conclusion can be drawn from here. Figure 36 b) shows only the more similar results. Using Young's law, it is possible to represent these measurements in terms of stress, see Figure 36 c). More tests have to be made in order to gain confidence in these measuring devices.

Repeatability of strain measurements using FBG sensors has to be greatly improved.

2.3.2. MIG

Strain in MIG welding is only measured using FBG sensors, since the high temperatures do not allow the usage of normal strain gauges and special high temperature strain gauges are not available up to this date.

Test A - FBG sensors

In the first test, strain was acquired using FBG sensors in the direction parallel to the welding line as defined in Figure 24. The obtained result may be seen in Figure 37.

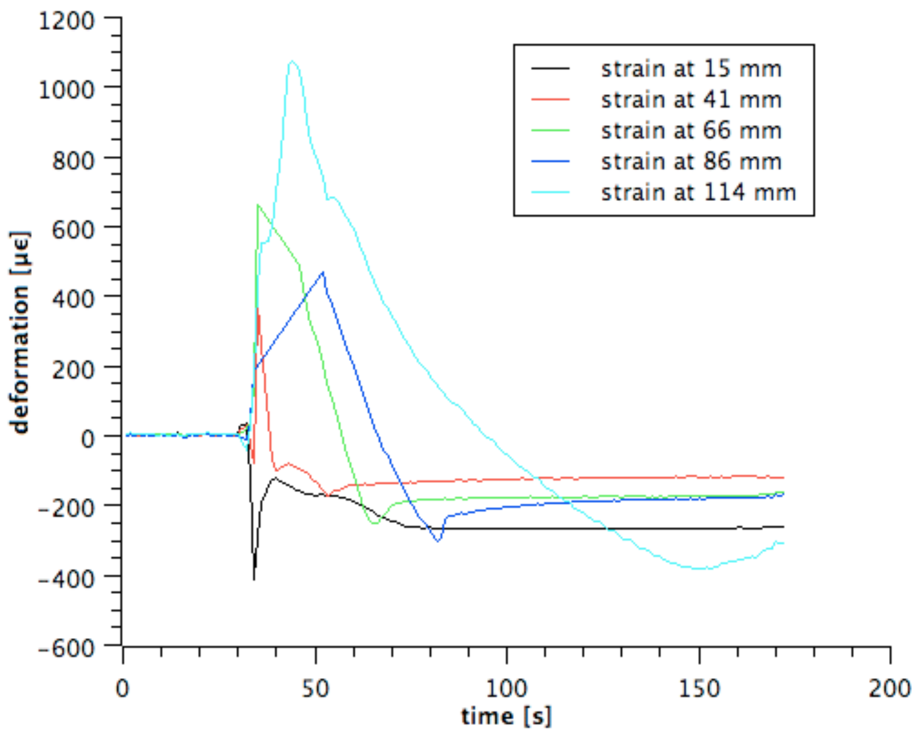

Fig. 37 - strain parallel to the MIG welding line acquired by FBG sensors

Due to the high failure rate of the FBG sensors and the absence of strain gauge measurements for validation of the measured magnitude, few conclusions may be drawn. Nevertheless it seems to be reasonable to conclude that tensile stress is measured in the welding direction when the torch passes the sensorial area. This can be explained by the momentary material expansion when the electric arc melts the filler and base material.

Since only the tips of the FBG sensors where bonded to the plate using a cyanoacrylate based adhesive, it should be verified if this method guarantees a complete transmission of tensile and compressive deformations of the plate surface to the fibers.

Test C - FBG sensors with different bonding methods

For verification of the effect of different bonding methods on measured strain, two different methods are compared. The instrumentation scheme is presented in Figure 27.

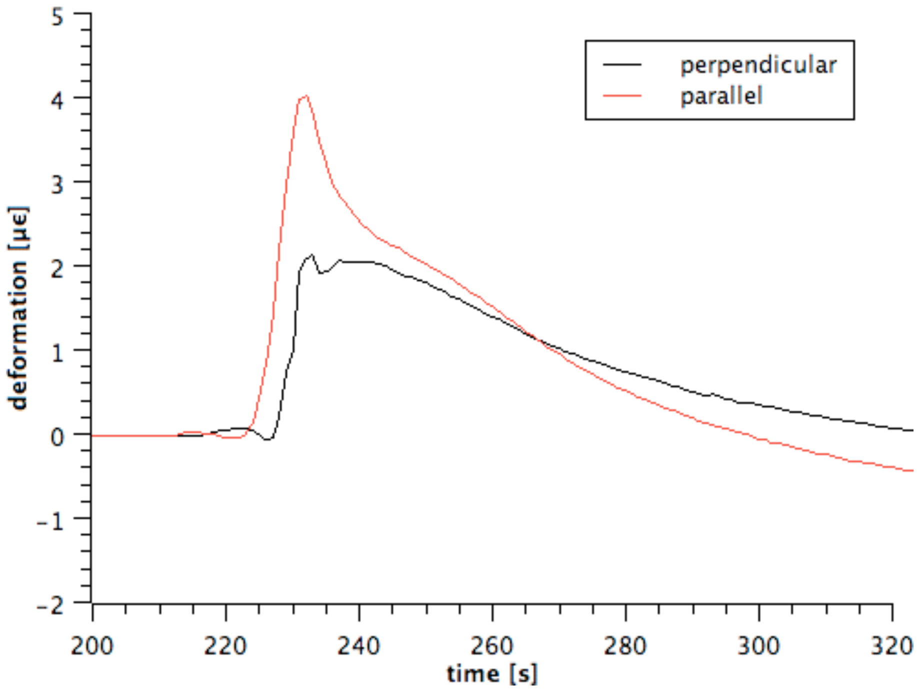

Fig. 38 - strain measured using FBG sensors completely glued perpendicular and parallel to the welding line at approximately 40 mm from weld-center

Results are presented in Figure 38. The results shown are from the completely bonded fibers, because the ones bonded only at their tips broke during measurement and no data could be retrieved. This results should be taken with care, since completely bonded fibers have shown to be a bad solution for temperature measurement. In terms of strain measurement no clear decision against completely bonding the fibers to the plate could be taken so far.

Since not enough thermal protection in the form of a silicon based gel was used in these tests, some FBG sensors have broken. In further tests, this protection should be taken with grater care, since in MIG welding the torch emits a very strong radiation.

2.4. Forces acting during FS welding

Since FS welding is a solid state thermomechanical joining process, forces acting during the process heavily influence the final weld quality, residual stresses and deformation. For MIG welding knowing the forces that may be acting on the plate during welding is almost irrelevant, since they are essentially of thermal type.

A Kistler Type 9272 three-axial load cell was used for this experiment. Figure 39 shows an image of the test setup. A National Instruments analog to digital converter and acquisition system is used to record the data using a NI LabView virtual instrument. Acquisition rate is 100 Hz.

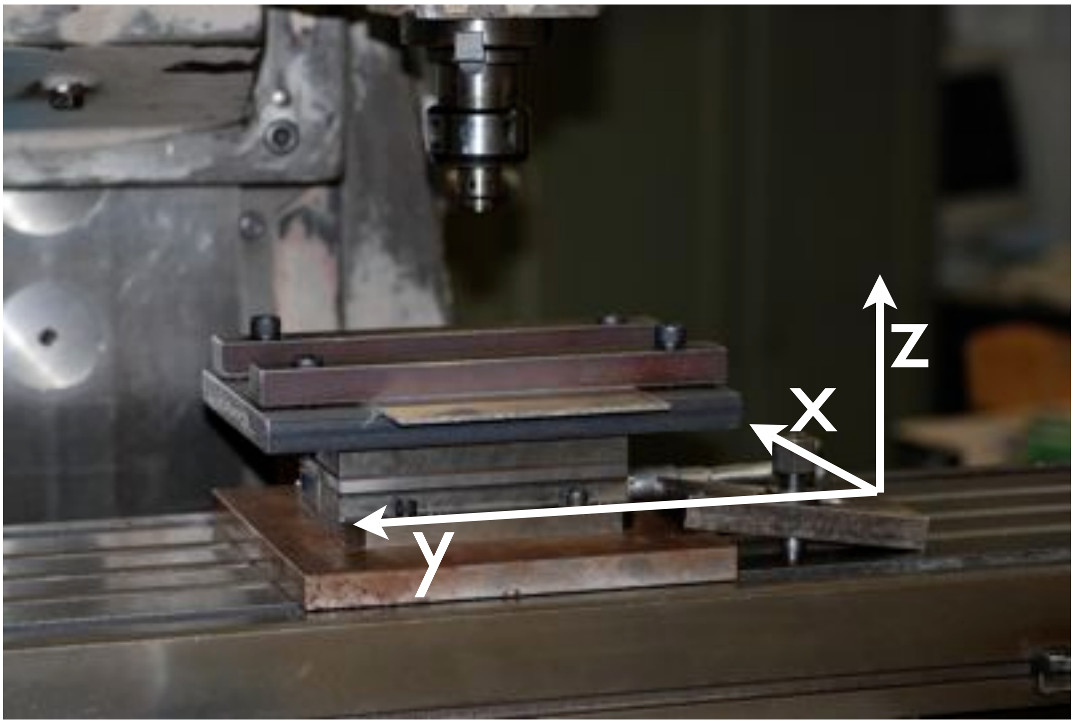

Fig. 39 - image of the test setup on the INDUMA milling machine

In order to find the scale value for the measurements, known forces are measured and the measured values are registered. Steel masses ranging from 0 to 60 kg are used for this goal. In Figure 40 the calibration graph is represented. The determined constants are the scale factors for each load cell axis.

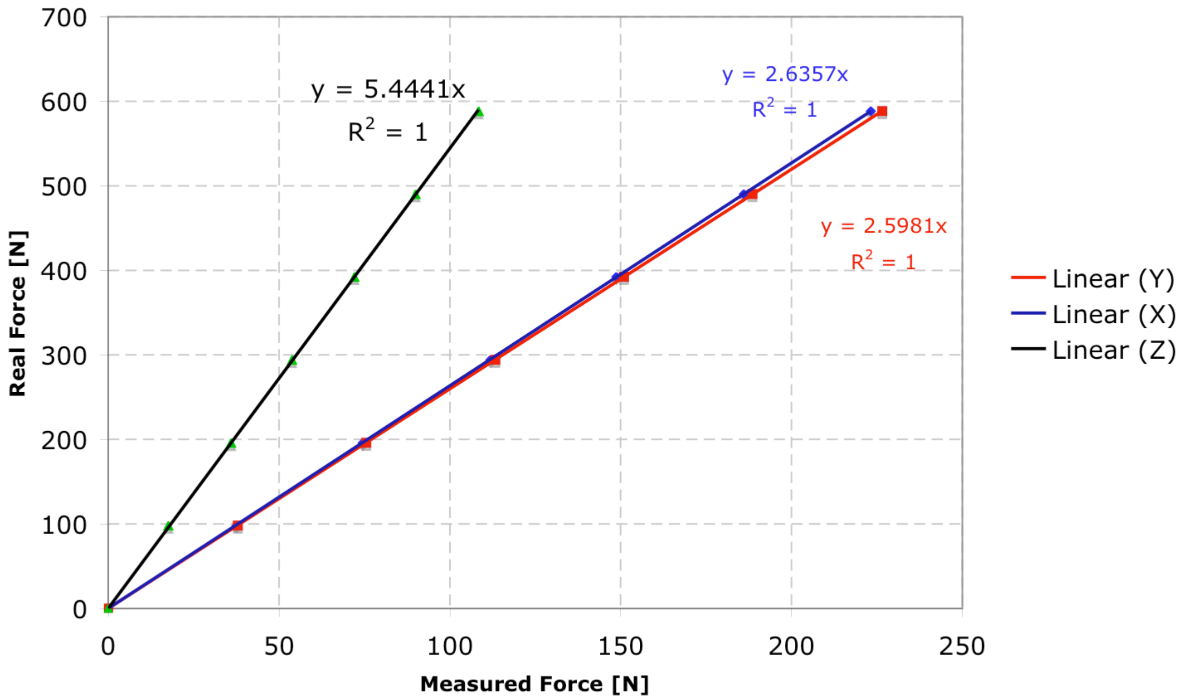

Fig. 40 - calibration of the Kistler Type 9272 load cell

Knowing these values, force in three axis may be measured during FS welding. Since a Kistler load cell is a high quality measuring device, it is sufficient to verify the calibration factor for a low force range - evolution is linear as is demonstrated by the $R^2 = 1$. The moment applied on the tool would be very important to know, but no device for this measurement is available at this time. Obtained results are shown in Figure 41.

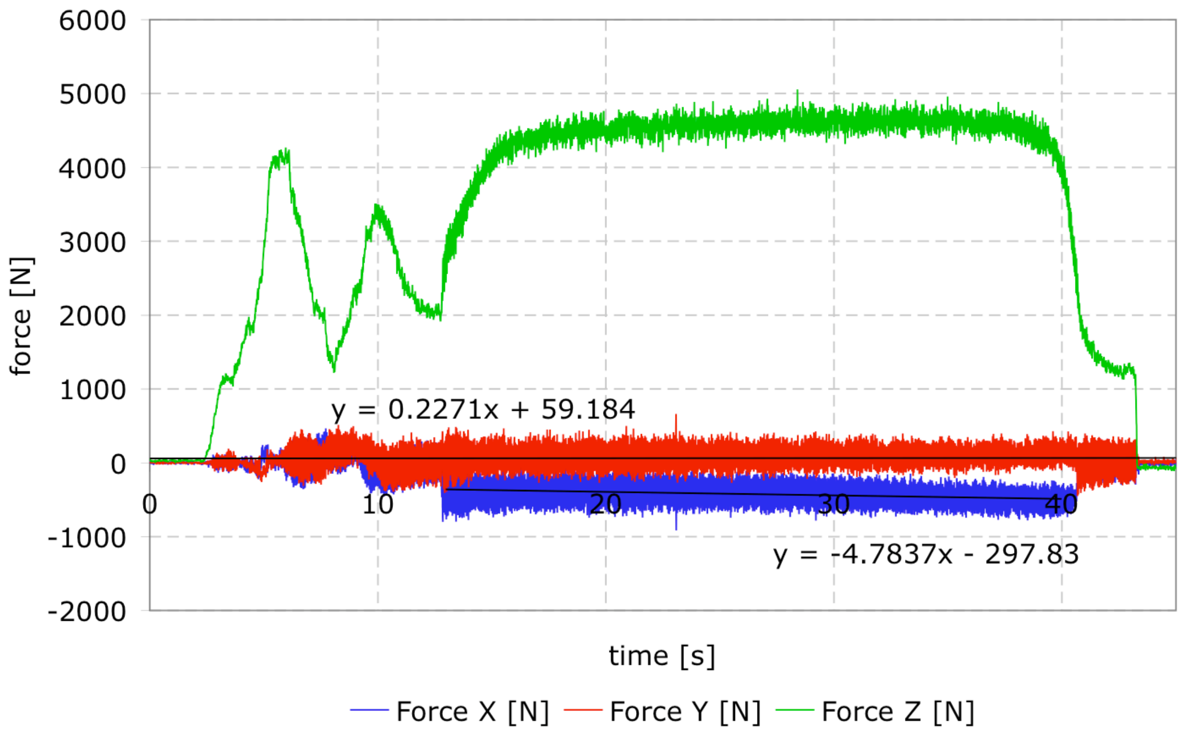

Fig. 41 a) - forces measured during FS welding

A maximum vertical force of almost 5 kN was measured in the opposite direction of the welding tool penetration, since compression of the stirred material takes place. Similar forces have already been measured on a specialized FS welding machine with equivalent plates of the similar material, but with higher advancing speeds and lower rotating speed [19, 20]. Only vertical force is taken for comparison for this reason. While the magnitude of forces is different due to different material properties, in [21, Figure 7] a similar tendency is visible for force evolution during the welding process. It is clearly visible that a transverse force exists and that transverse and advancing forces are around 10 % of the axial force. This however depends greatly on the particular welding process and material surface properties and is therefore not compared in terms of magnitude.

Opposite to the welding direction a mean reaction force of about 60 N was measured. This effect remains to be explained, it should however be noted that the variation around this mean value is quite strong. In the perpendicular direction to the welding line, about 300 N act in the direction of the advancing side. This transverse force does not contribute to the welding itself, but could potentially lead to misalignment in the work-piece or the welding equipment.

As it can be seen, the mean force in the X direction doesn't seem to be constant along the welding line. This is most likely due to a misaligned load cell. Figure 41 b) shows a augmented view of the above Figure where the variation of the X and Y forces can be seen.

The Z component seems to be affected by a lot of noise, which may originate from reaction forces of the tool and the plate surface.

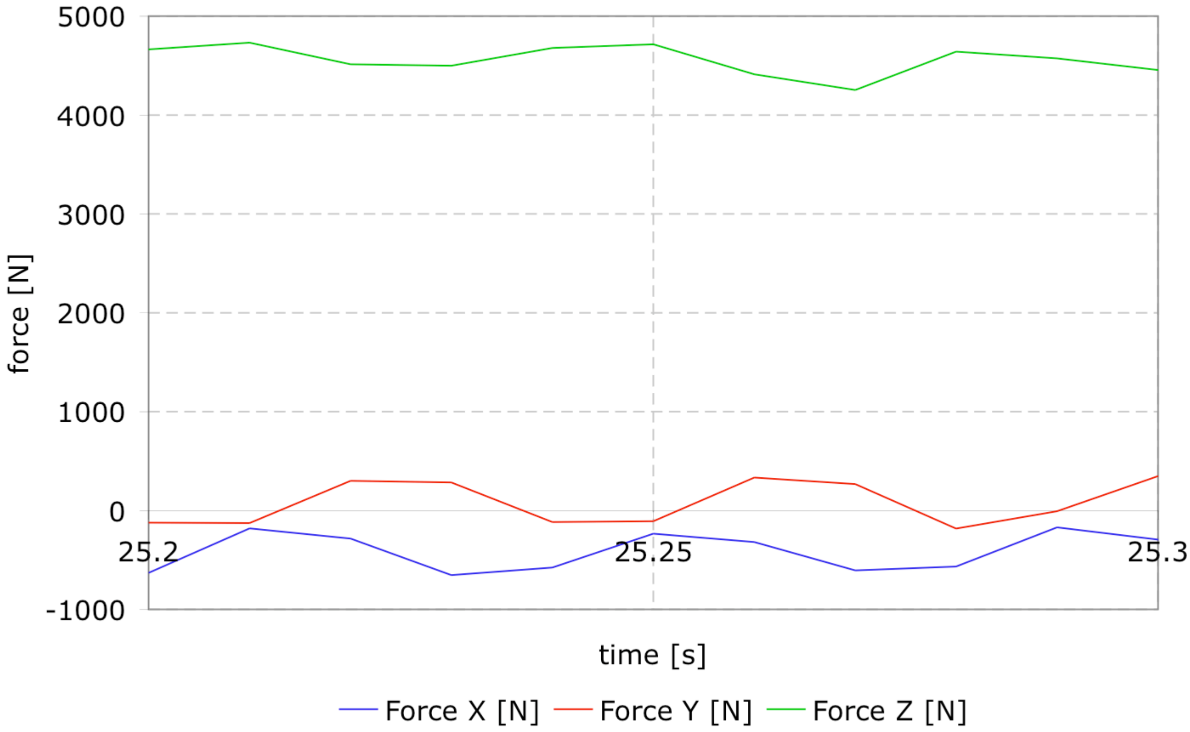

Fig. 41 b) - forces measured during FS welding - magnification of Figure 27.7 a)

A rotating speed of 1500 rpm is equivalent to 2.5 rotations per 0.1 s represented in Figure 41 b). It is appreciated that the X and Y forces vary with the rotation of the tool as could be expected. The force in Z direction doesn't seem to be as regular, which means that this force variation is not directly related to the tool rotation. The variation in Z-direction is most likely related to noise created by the friction of the shoulder on the Aluminium plate.

A higher acquisition rate would be preferred in order to verify these observations.

Knowing the forces which act during the welding process also helps to prevent broken tools, since the forces are applied through this tool.

3. Fatigue

Many engineering applications, as in aeronautical industries, require durability under cyclic loading, i.e. fatigue strength. Two types of tests are presented in this work. The first one concerns crack growth, relevant for damage tolerance studies; the second type of tests is concerned with fatigue life until crack initiation.

3.1. Material property characterization

3.1.1. CT - fatigue crack growth rate determination

Al6056-T6 and Al6056-T651

Crack growth behavior is analyzed by compact tension (CT) tests. The obtained material parameters may later be used for crack growth modeling by semi-empirical laws.

Two types of AA6056 specimens are analyzed in this work. The first ones were obtained by reducing a 30 mm thick plate in the T651 condition to the final thickness of 4 mm by high speed machining (HSM), and the second set of specimens was obtained by machining a 5 mm thin plate in the T6 condition (LBW) to the same final thickness. Values in the Paris regime (10-5 < da/dN < 10-3 mm/cycle) are obtained by using CT specimens of 4 mm thickness.Tensile test have also been performed on these materials for test-parameter definition.

A more detailed description of these tests may be found in [22].

The CT specimens dimensions are presented in Figure 42 and follow the ASTM E647 standard [23]. Fatigue testing is carried out on a servo-hydraulic MTS 321.31 machine using a 5 kN load cell at a frequency of 20 Hz in laboratory air. Crack length is optically measured at both specimen surfaces with a resolution of 0,01 mm.

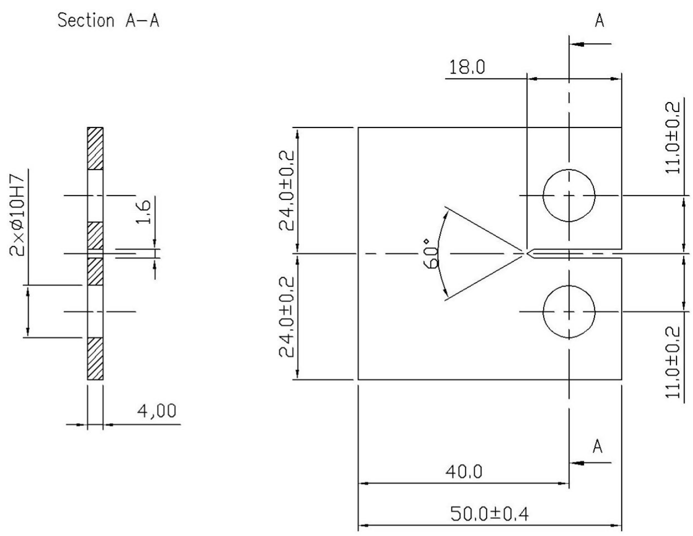

Fig. 42 - Compact tension (CT) specimen (dimensions in mm)

Fatigue crack propagation behavior of the AA6056 in the conditions described above is investigated for two different R values (R = 0,1 and R = 0,5).

Two specimens for R = 0,5 and four specimens for R = 0,1 are tested for HSM material. A good agreement between data obtained using different specimens is found for tests performed at both R values. Nevertheless a greater scatter appears for R = 0,1 which lead to the evaluation of more specimens than for R = 0,5. A MATLAB based data treatment algorithm may be found in [Annex C].

Two specimens for both R values of LBW material are tested and a good agreement is found between each pair of tests.

The fatigue crack propagation behavior for the AA6056 material in both conditions and tested at both R values is shown in Figure 43. Each one of the four curves presented corresponds to all the data points obtained for the specified situation.

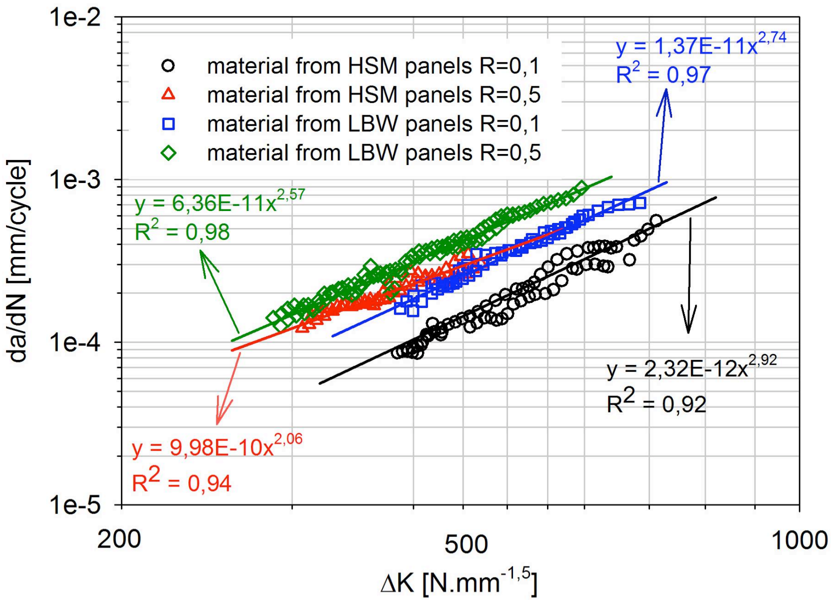

Fig. 43 - Crack propagation data obtained with HSM AA6056-T651 and LBW AA6056-T6 CT specimens

In Figure 44 it is shown that the results obtained for the LBW CT specimens are in accordance with the values found by Vaidya et al. [24] testing AA6056-T6 specimens with a thickness of 4 mm. For the HSM material no comparison values could be found in the literature.

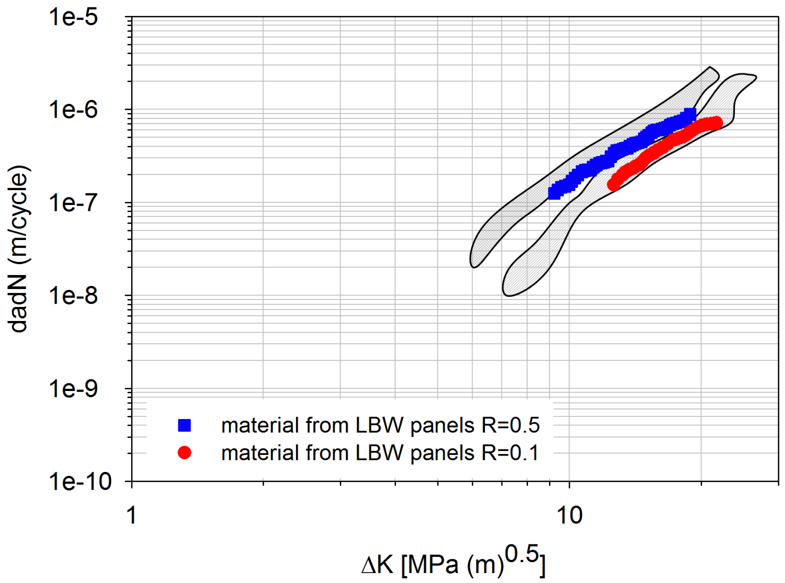

Fig. 44 - Comparison of results obtained with LBW CT specimens and results presented by Vaidya et al., [24]

The specimens in both material conditions shown in Figure 45 present a different crack surface which also justifies the difference found in da/dN vs. ΔK.

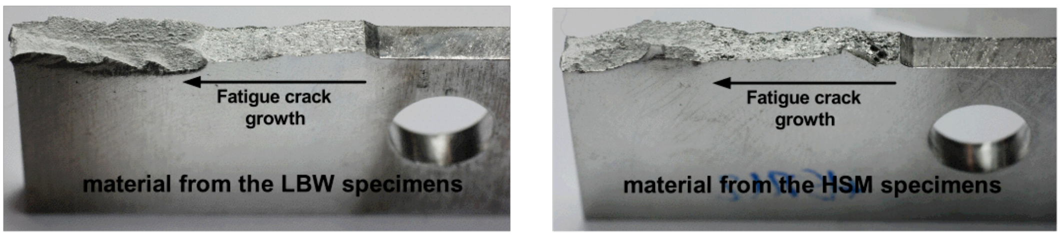

Fig. 45 - Fracture surface of CT specimens in both material conditions

The fracture surface of the HSM CT specimen presents a roughness and heterogeneity not found in the LBW CT specimens. This may be due to the fact that HSM CT specimens are machined from very thick material, so that they actually correspond to one of the surface layers of the thick material. Such a situation does not occur with the LBW specimens, which are machined from thinner material. This seems to be reflected in the more homogeneous features displayed by their fracture surfaces.

The crack growth results presented in Figure 43 are fitted using a power law whose coefficients correspond to the Paris law coefficients described later on, see Table 4.

Table 4 - C and m Paris law parameters for the AA6056 from HSM and LBW specimens

$\left[\frac{Nmm^{-1.5}}{mm/cycle}\right]$	HSM AA6056-T651		LBW AA6056-T6	
	R = 0.1	R = 0.5	R = 0.1	R = 0.5
C	2.32E-12	9.98E-10	1.37E-11	6.36E-11
m	2.92	2.06	2.74	2.57

These values can be used for crack growth prediction using the Paris law. Other parameters necessary for further laws may be derived from the raw test results presented before.

3.1.2. SN - fatigue life determination

Uniaxial fatigue tensile tests were carried out on specimens extracted from laser beam welded butt joints, and are expressed as stress range Δσ (MPa) versus the corresponding life to failure (N) for each aluminium alloy analyzed.

AA 6061-T6

Fatigue life in LB welded specimens was analyzed by SN tests. Macrogpraphs, micrographs and microhardness measurements of the welding were taken. Fractographs were also used for defect determination.

In order to define the fatigue testing levels, tensile tests of the welded specimens are performed. ASTM E8-03 standard was followed [25]. The tensile test curve for each specimen is presented in Figure 46 compared to the curve of the base material.

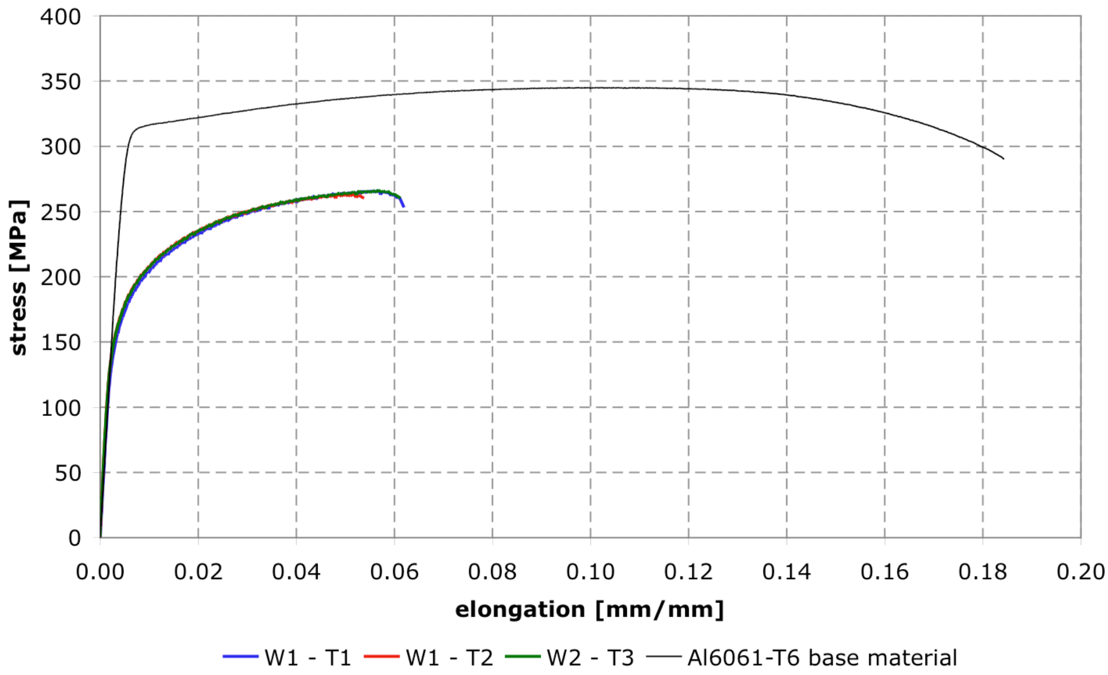

Fig. 46 - tensile test curve

From the tests mentioned above, the material properties in Table 5 can be determined. These are properties of the mixture of base and filler material.

Table 5 - welded material properties

yield strength	171 MPa
rupture stress	264.50 MPa
Young's modulus	72.2 GPa
elongation	4.35%

As expected, these values are different from the base material's properties in Table 6.

Table 6 - base material properties [26]

yield strength	> 240 MPa
rupture stress	> 290 MPa
Young's modulus	69 GPa
elongation	10.0%

MTS 312.31 (PID 5.8/0.58/0.0004) and MTS 810 (PID 20/2/0.04) servo-hydraulic instruments were used for these tests.

Fatigue tests were performed with the stress levels indicated in Table 7 as percentage of yield strength determined before by tensile-tests.

Table 7 - data used for fatigue testing

	110%	100%	90%	75%	60%	55%	50%
σ_{max}	188.0	171.0	153.9	128.3	102.6	94.1	85.5
R	0.1	0.1	0.1	0.1	0.1	0.1	0.1
σ_{min}	18.8	17.1	15.4	12.8	10.3	9.4	8.6
F_{max}	8606	7823	7041	5867	4694	4303	3912
F_{min}	861	782	704	587	469	430	391
F_{mean}	4733	4303	3873	3227	2582	2367	2152
F_{amp}	3873	3520	3168	2640	2112	1936	1760

Infinite fatigue life was defined as being more than 10 million cycles. Only one specimen at 50% and two at 55% were analyzed, since infinite life was measured in one of these tests.

For all other stress levels, three specimens were tested; the fracture occurred for a number of cycles inferior to the considered fatigue threshold.

Table 8 resumes the results that were obtained in the fatigue test program for AA6061-T6.

Table 8 - results obtained in the fatigue test

speci-men	stress [MPa]	%yield	R	frequency [Hz]	cycles	test equipment
W1-F1	153.9	90	0.1	10	59796	MTS 810
W1-F2	102.6	60	0.1	20	858062	MTS 312.31
W1-F3	102.6	60	0.1	20	731978	MTS 312.31
W1-F4	153.9	90	0.1	14	94921	MTS 312.31
W1-F5	102.6	60	0.1	20	1120369	MTS 312.31
W1-F11	153.9	90	0.1	20	86100	MTS 312.31
W1-F6	85.5	50	0.1	20	10247343(did not break)	MTS 312.31
W1-F7	94.1	55	0.1	20	4188714	MTS 312.31
W1-F8	94.1	55	0.1	20	10000000 (did not break)	MTS 312.31
W1-F10	128.3	75	0.1	13	167160	MTS 810
W2-F1	128.3	75	0.1	16	271819	MTS 312.31
W2-F2	128.3	75	0.1	13	364282	MTS 810
W2-F3	171	110	0.1	9	19430	MTS 810
W2-F4	171	110	0.1	9	31903	MTS 810
W2-F5	171	110	0.1	9	29346	MTS 810

The scatter of results for each stress level is normal in fatigue tests of welded material specimens. Nevertheless only three specimens were tested at each level, since only a limited number of specimens was available for this analysis.

The SN curve of the fatigue tests is shown in Figure 47.

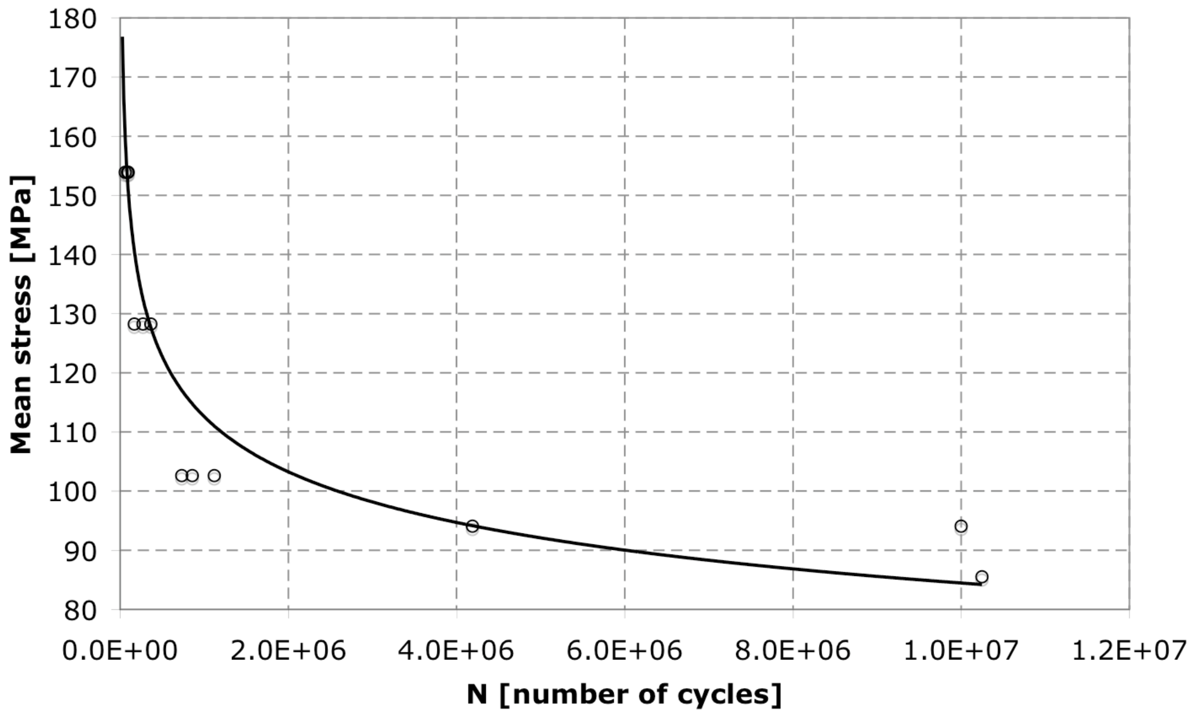

Fig. 47 a) - SN-curve

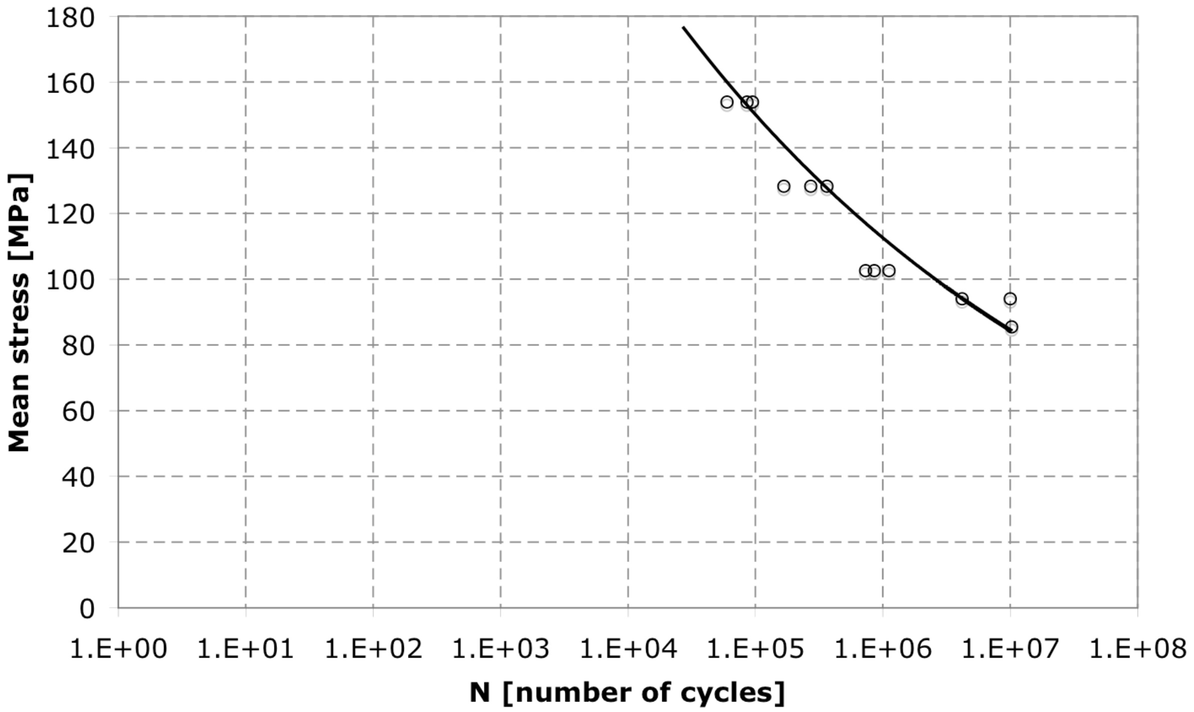

Fig. 47 b) - SN-curve - logarithmic scale

As can be seen by the shape of the curve, the tests seem to give good results. A comparison with another alloy will be given later on.

In Figure 48 the fracture surfaces of some fatigue coupons can be seen.

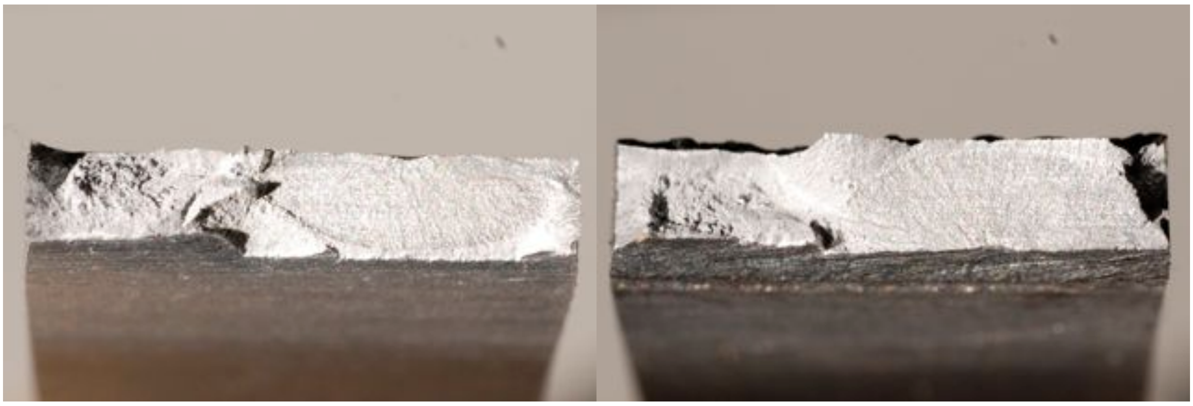

Fig. 48 a) - fracture surface of fatigue specimen W1-F3

On the right side of the above images a fatigue zone can be seen. The left side shows ductile failure.

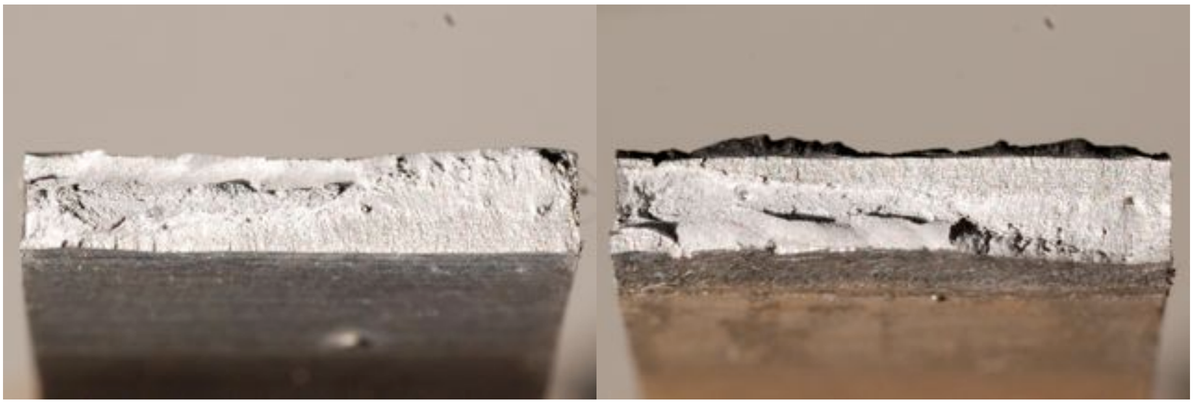

Fig. 48 b) - fracture surface of fatigue specimen W1-F10

The bottom zone of the fatigue specimen has the typical flat aspect of brittle fatigue fracture surfaces. The top side failed due to ductile failure.

All fractures occurred in the HAZ (heat affected zone) near the weld bead.

A micro-hardness measurement was performed on the specimen represented in Figure 50. The result is represented in Figure 49.

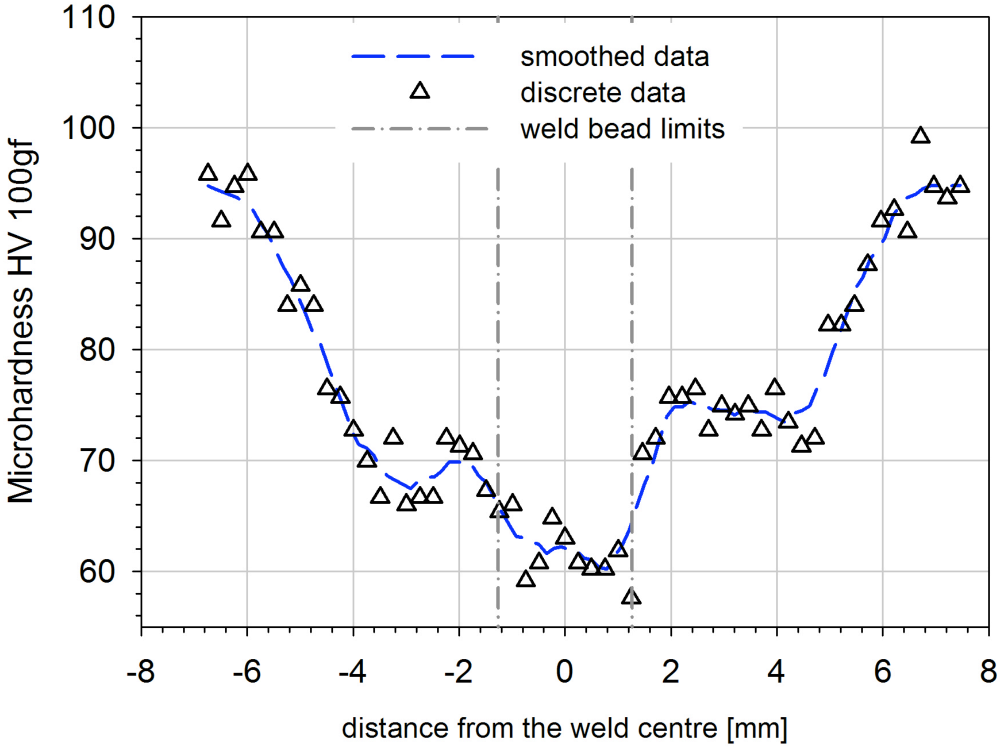

Fig. 49 - micro-hardness measurement of Al6061-T6 LBW welded specimen

Three different hardness zones can be identified. The highest values are measured in the base material. A lower level is found in the heat affected zone, and lowest hardness values are measured in the weld metal.

The materials' microstructure is also analyzed. Figure 50 shows a macrography of the welding area where microstructures represented in Figure 51 were taken.

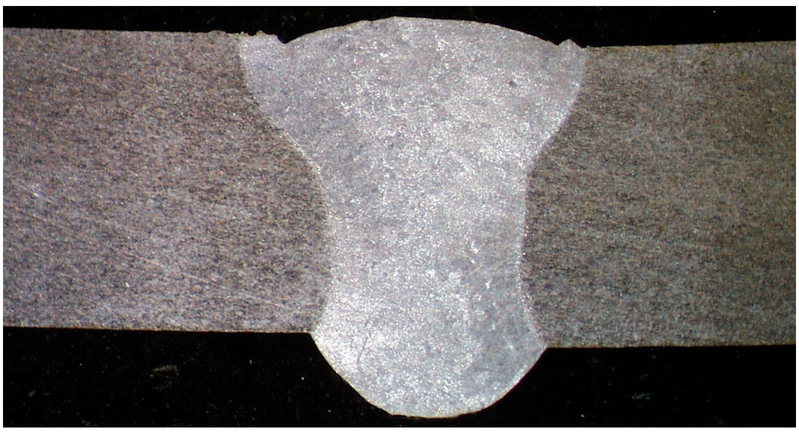

Fig. 50 - macrography of welding zone

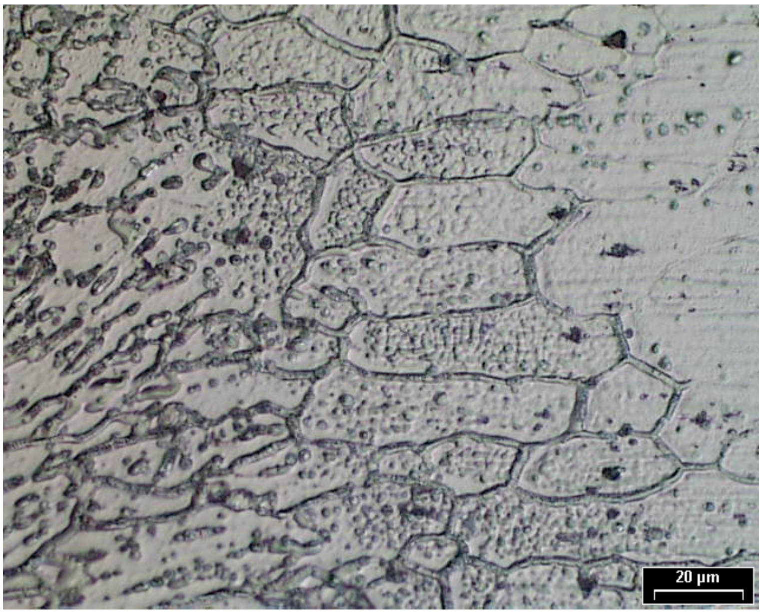

Fig. 51 a) - microstructure Al6061-T6: transition zone

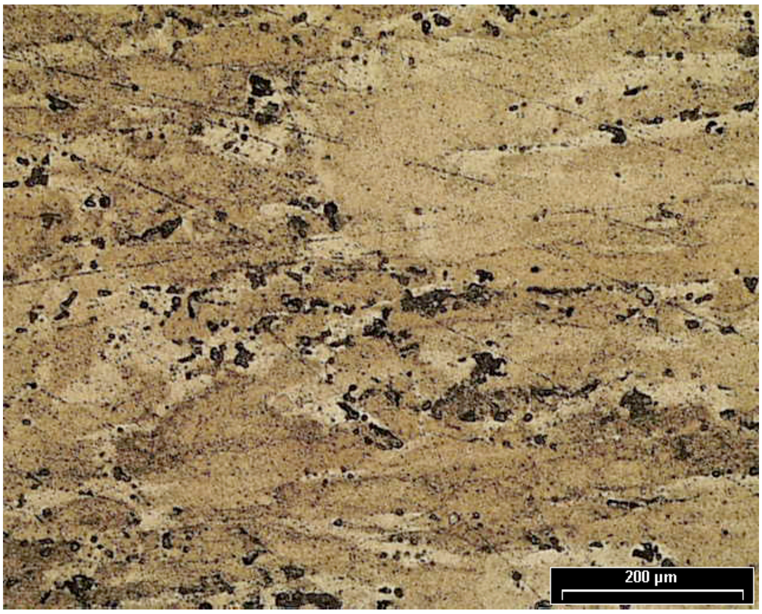

Fig. 51 b) - microstructure Al6061-T6: base material

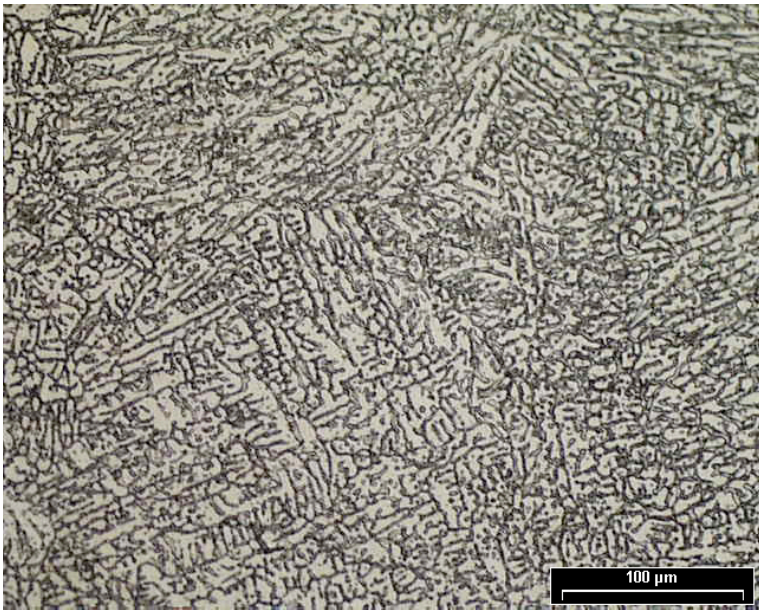

Fig. 51 c) - microstructure Al6061-T6: weld metal

A typical solidification structure can be found in the welding pool area.

AA 6082-T6

AA 6082-T6 has shown to be more difficult to weld than AA6061-T6. Therefore some defective welds have been received as well. Since the main interest of this part of the work is fatigue life characterization, a comparison between supposedly good welds and defective welds is also performed.

In order to define the fatigue test levels, tensile tests of the welded specimens are performed. The tensile test curve for each specimen is presented in Figure 52 compared to the base materials test curve.

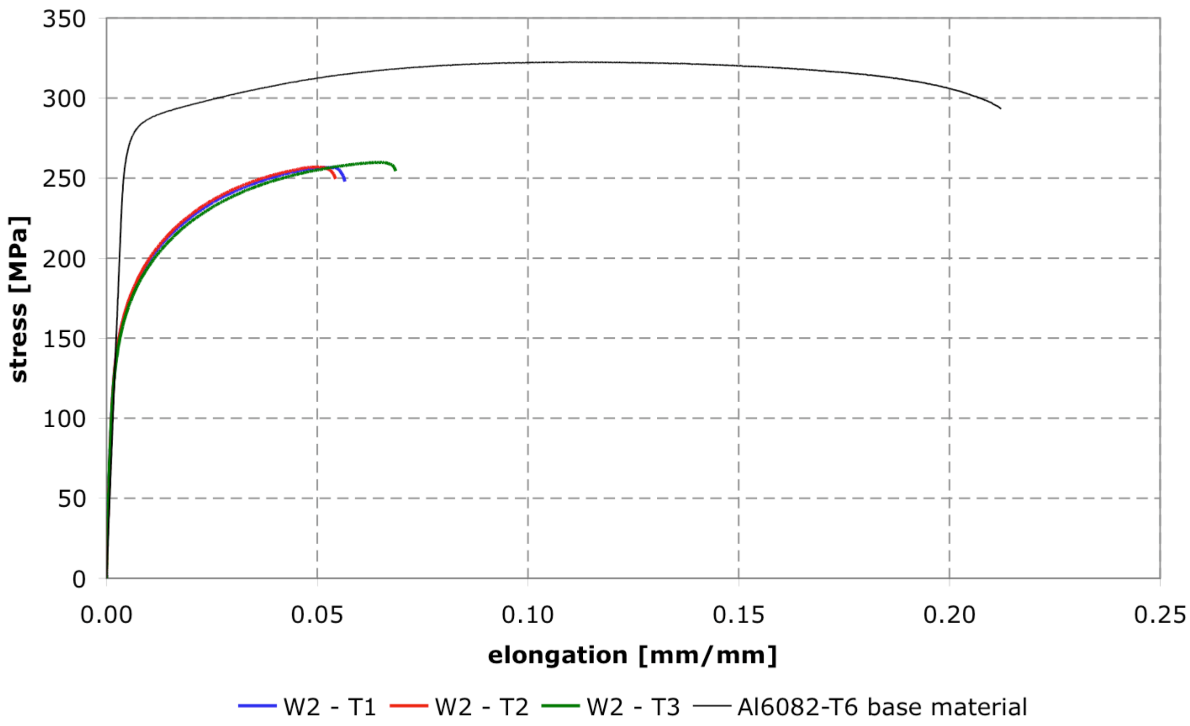

Fig. 52 - tensile test curve for AA6082-T6

From the tests mentioned above, the material properties in Table 9 can be determined. These are properties of the mixture of base and filler material.

Table 9 - welded material properties

yield strength	162.4 MPa
rupture stress	259.5 MPa
Young’s modulus	71.5 GPa
elongation	4.50%

As expected, these values are different from the base materials properties in Table 10.

Table 10 - base material properties [27]

yield strength	323 MPa
rupture stress	376 MPa
Young's modulus	64.9 GPa
elongation	17.5%

An MTS 810 servo-hydraulic instrument is used for the fatigue tests described below.

Fatigue test are performed with the stress levels indicated in Table 11 as percentage of yield strength determined before by tensile-tests.

Table 11 - data used for fatigue testing

	110%	90%	75%	60%	50%
σ_{max}	178.6	146.2	121.8	97.4	81.2
R	0.1	0.1	0.1	0.1	0.1
σ_{min}	17.9	14.6	12.2	9.7	8.1
F_{max}	8173	6687	5572	4458	3715
F_{min}	817	669	557	446	371
F_{mean}	4495	3678	3065	2452	2043
F_{amp}	3678	3009	2508	2006	1672

Additionally to the above mentioned tests, one defective specimen was tested on each stress level below tensile strength.

Table 12 resumes the results of the fatigue tests made.

Table 12 - fatigue tests done on AA6082-T6 LBW specimens

Speci-men	%yield	R	frequency [Hz]	cycles	equipment	plate nr
W3-F1	60%	0.1	15	109347	MTS 810	3
W3-F2	60%	0.1	15	625283	MTS 810	3
W3-F3	60%	0.1	15	615550	MTS 810	3
W3-F4	50	0.1	15	891777	MTS 810	3
W3-F5	50	0.1	15	693555	MTS 810	3
W3-F6	50	0.1	15	1298464	MTS 810	3
W3-F7	75	0.1	12	302632	MTS 810	3
W3-F8	75	0.1	12	217447	MTS 810	3
W3-F9	75	0.1	12	138278	MTS 810	3
W3-F10	90	0.1	11	46486	MTS 810	3
W3-F11	90	0.1	11	58420	MTS 810	3
W3-F12	90	0.1	11	54235	MTS 810	3
W3-F14	110	0.1	9	22692	MTS 810	3
W3-F15	110	0.1	9	16579	MTS 810	3
W3-F16	110	0.1	9	49365	MTS 810	3
W3-F13	60	0.1	15	535650	MTS 810	2
W2-F1	50	0.1	15	240666	MTS 810	2
W2-F2	60	0.1	15	44134	MTS 810	2
W2-F3	75	0.1	12	29949	MTS 810	2
W2-F4	90	0.1	11	9053	MTS 810	2

This data may be presented in a SN-curve like Figure 53.

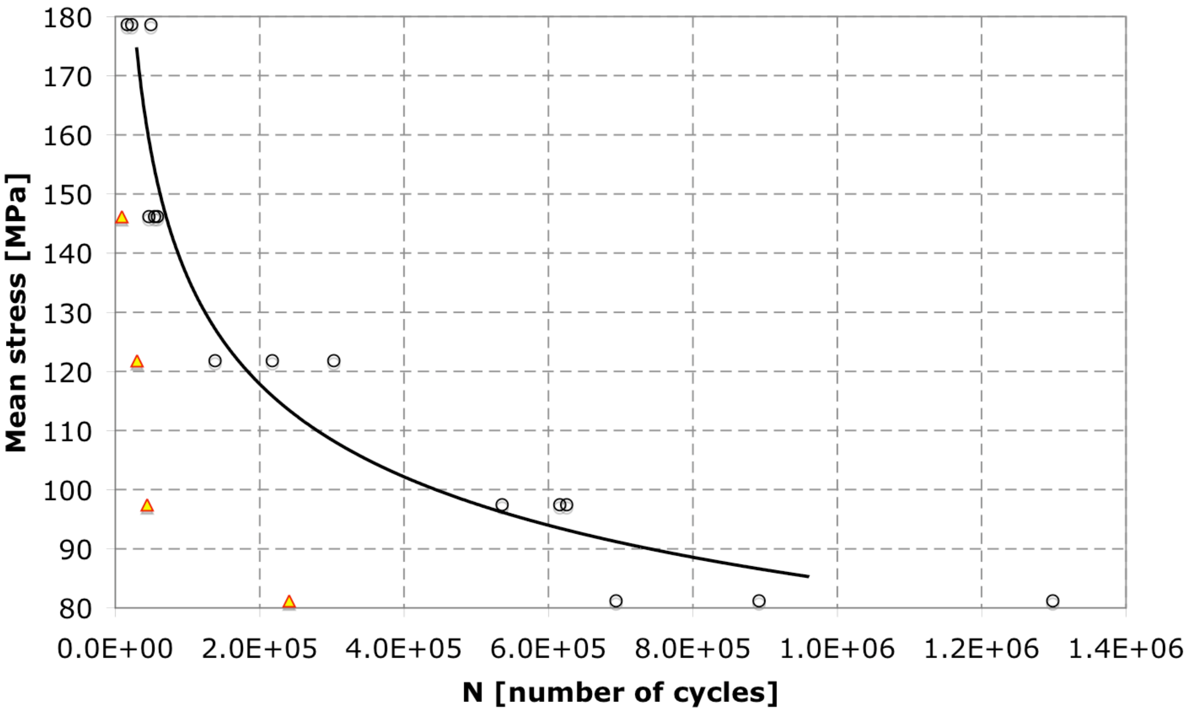

Fig. 53 a) - SN curve for Al6082-T6 LBW

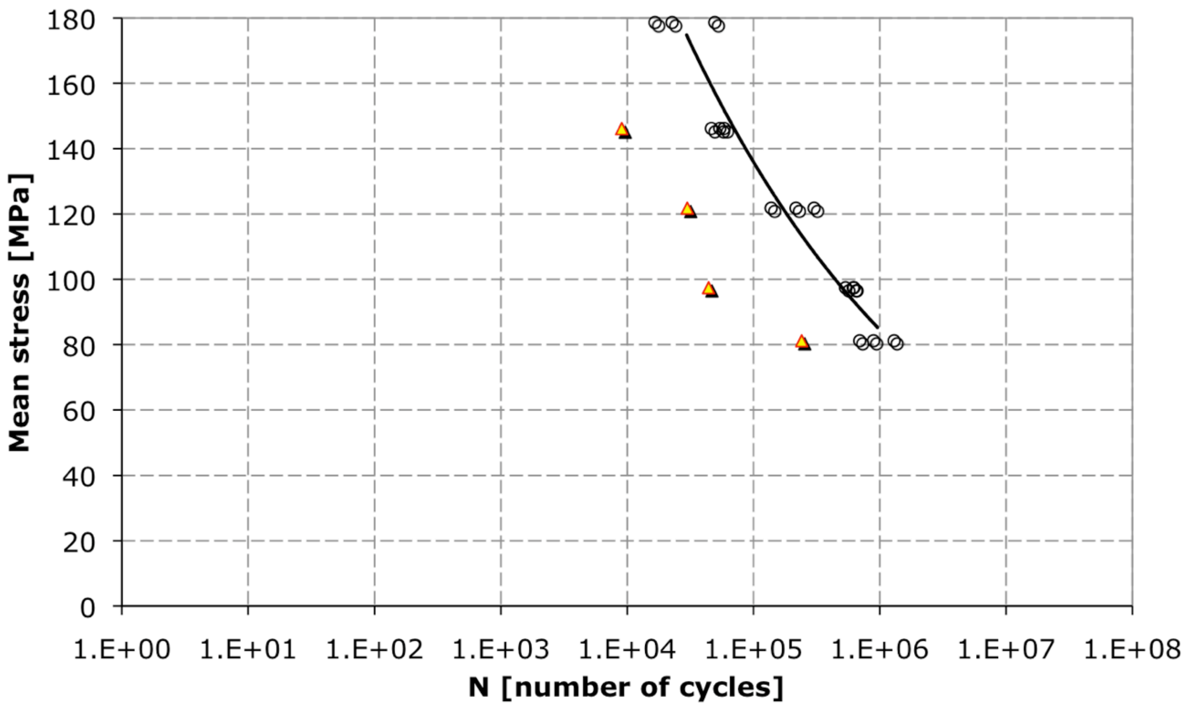

Fig. 53 b) - SN curve for Al6082-T6 LBW - logarithmic scale

As can be seen, welding defects strongly affect fatigue life, reducing the expected life by almost five times.

Figure 54 shows some of the fracture surfaces of “intact” LB welded 6082-T6 specimens.

Fig. 54 a) - fracture surface of fatigue specimen W3-F2

The fatigue zone is well defined as it is also the case in AA6061-T6.

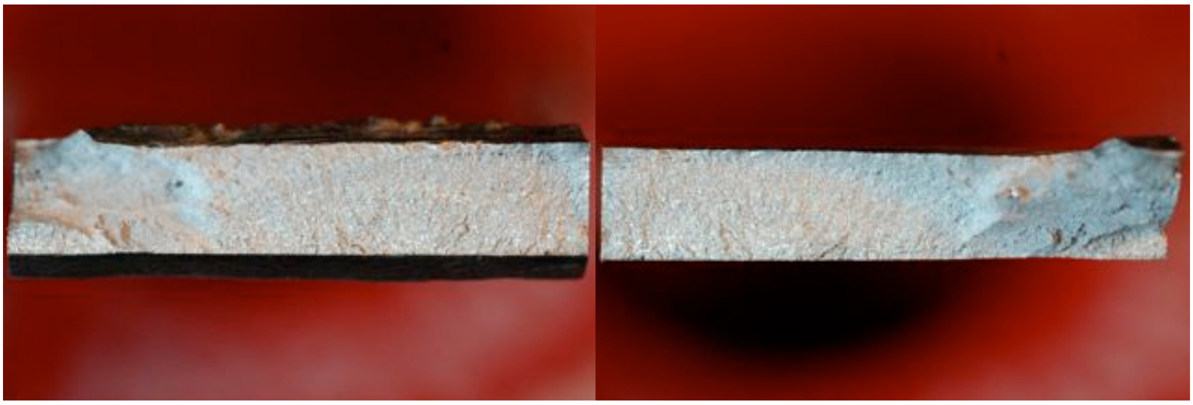

Fig. 54 b) - fracture surface of fatigue specimen W3-F5

As can be seen, the extend of the fatigue cracking zone is rather high in these specimens.

Figure 55 shows a defective specimen before the fatigue tests. Welding defects can be seen by naked eye, but their influence on fatigue life is difficult to predict from this point of view.

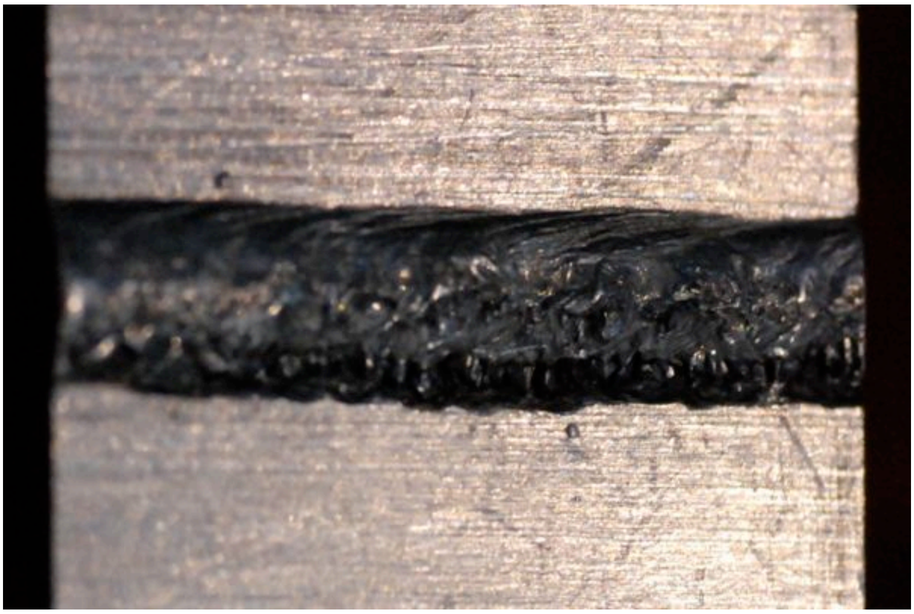

Fig. 55 - macrography of the specimen with welding defects - W2-F2

These defects have a very detrimental effect on fatigue life, as can be seen in Figures 53.

The actual fracture surface of some of the defective specimens may be seen in Figure 56.

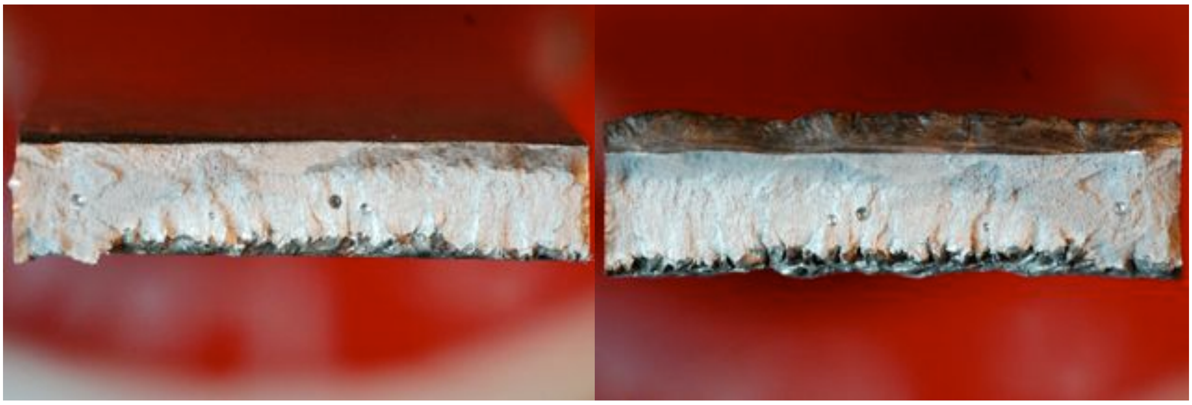

Fig. 56 - fracture surface of specimen W2-F2

Comparing the surfaces of Figure 56 to the ones presented in Figure 54, it is understandable that this specimens didn't last as long as the intact ones during fatigue testing, since a lot of stress concentration points can be found, and the actual resistive area is smaller than on an equivalent normal specimen.

Microhardness measurements are performed in the center-line of the weld as can be seen in Figure 57 in order to characterize the extent of the zone affected by welding.

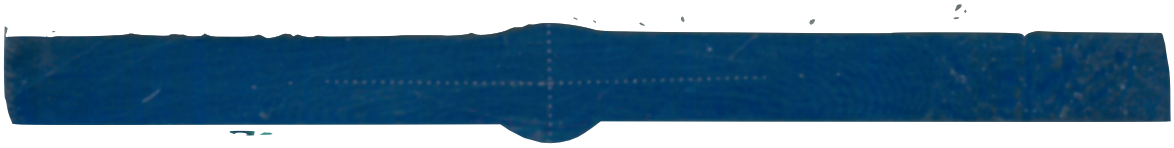

Fig. 57 - microhardness measuring location

The result of these measurements are shown in Figure 58.

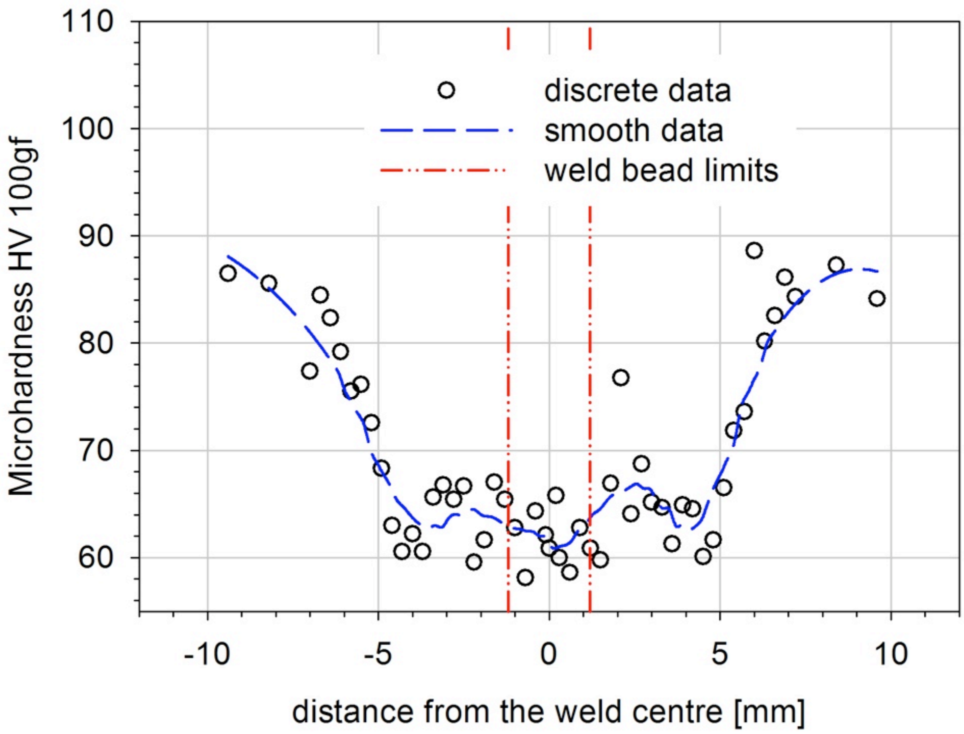

Fig. 58 - microhardness measurements of laser beam welded AA6082-T6

As can be seen, the hardness drops about 30% when reaching the heat affected zone of the laser beam weld. The hardness profile across the welding is almost linear, but always on low hardness levels.

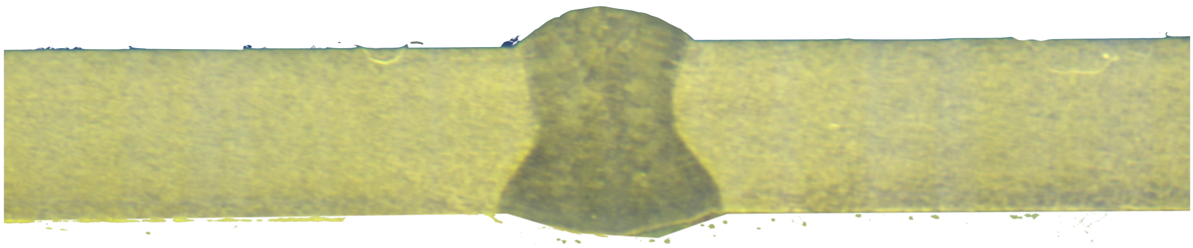

Fig. 59 - macrography of the laser beam welded specimen

The weld metal can easily be distinguished from the base material in Figure 59. Figures 60 a) to c) show the microstructure at three points of the above specimen after a 25 second chemical attack with 8% solution Hydrofluoric acid (HF).

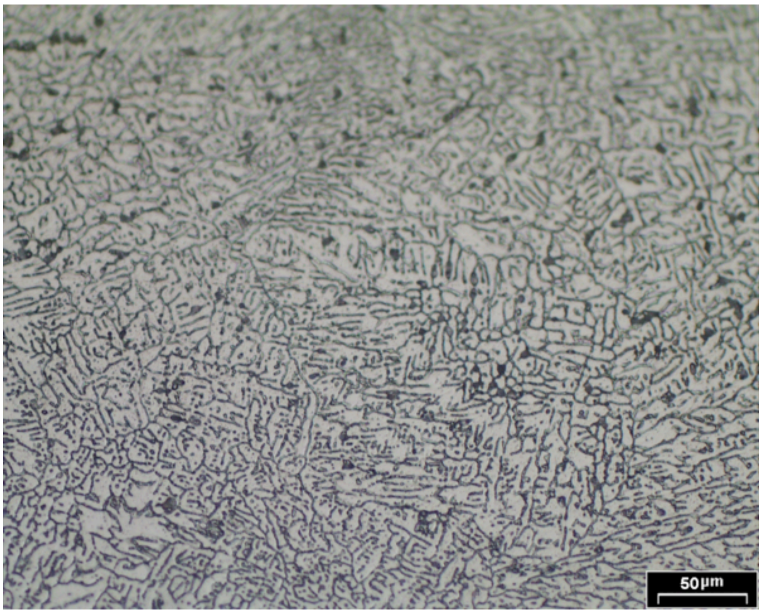

Fig. 60 a) - microstructure in the center of the welding line

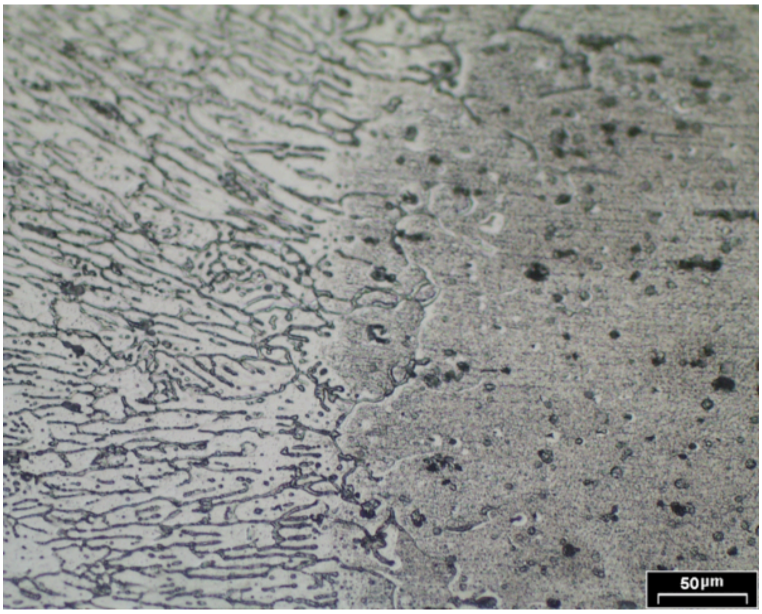

Fig. 60 b) - microstructure of the transition zone

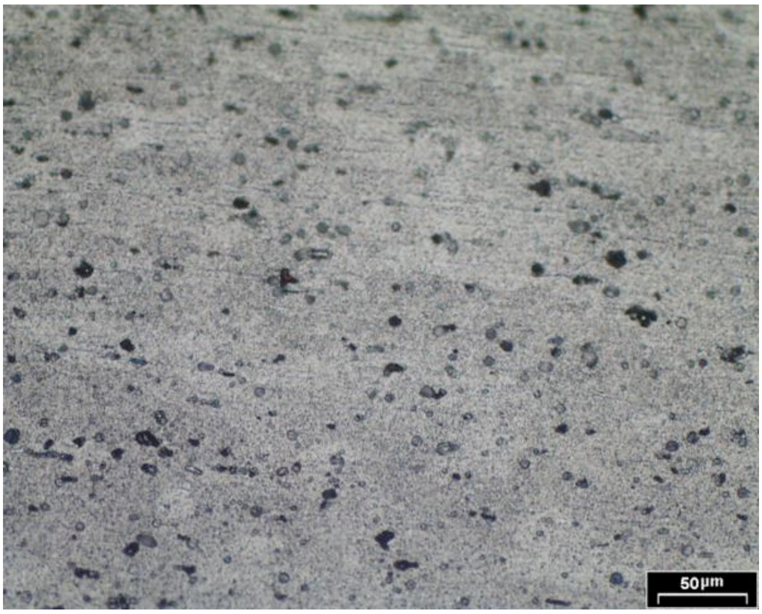

Fig. 60 c) - microstructure of the base material

As can be seen, the influence of a laser beam in welding is very localized as opposed to MIG and even FS weldings. As could also be seen, the quality of the weld depends on the base and filler material and the process parameters used.

3.2. Fatigue life prediction

In order to determine material depended properties such as crack growth rate, measurements are carried out on specimens of several types, as for example the CT-specimens presented in section 1.

3.2.1. Crack growth laws - a review

Different crack growth laws exist for different needs. Complexity and precision varies from case to case. The present comparison is made, because life prediction considering residual stresses is sometimes needed, and not every equation may be used for this case.

In Figure 61, a typical crack growth rate dependency on ΔK is shown.

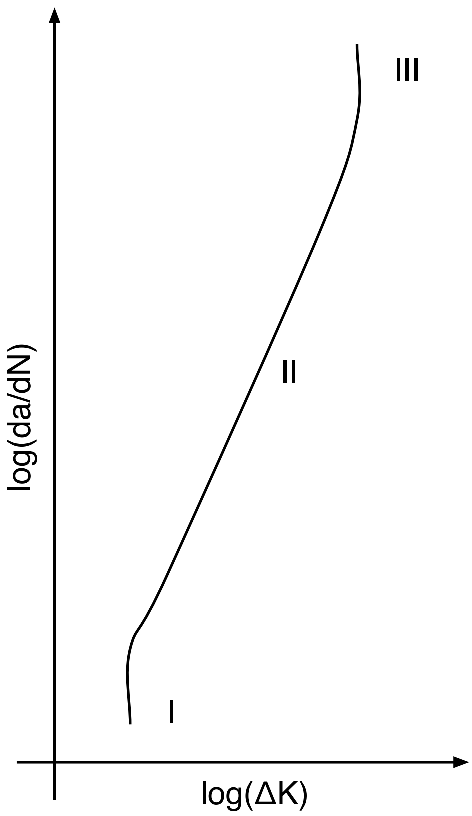

Fig. 61 - typical crack growth rate evolution as a function of ΔK

The curve in Figure 61 may be described by various laws, some of which are presented below. Different constants have to be determined from experimental results depending on the selected law.

Effects of residual stress for example, have to be introduced into these laws using the R ratio. $R=K_{min}/K_{max}$, being $K_{max} = K_{res} + \Delta K_{applied}$ and $K_{min} = K_{res}$. This means that ΔK is not affected by residual stress.

Paris law

The Paris law [28], named after Paul Paris, is a simple relation which describes the second stage of crack growth rate.

C and m have to be known for the R of interest. This means that normally only constant R problems may be analyzed by this law. Residual stress problems tend to have varying R and the use of this law is therefore not recommended.

$$\frac{da}{dN} = C\Delta K^m \tag{2}$$

Constants have to be determined from experimental results. Since only 2 constants are unknown, a linear approximation for the required R ratio in the second stage of the crack growth rate is sufficient for the parameter determination.

Walker law

The crack growth law developed by Walker introduces the dependence of crack growth rate with R. The constants C and m from the Paris law have to be known, but R also affects the results directly.

$$\frac{da}{dN} = C(\frac{\Delta K}{(1-R_{eff})^n})^m \tag{3}$$

This law is known to super-estimate the R-effect.

Constants have to be determined from experimental results in the same way as for the Paris law, but for different R levels. The parameter “n” is chosen in a way that guarantees a good fit to experimental data for different R ratios.

Forman law

Forman refined the known crack growth laws with the dependence on R and acceleration in the end of the specimens life. This law exhibits a good balance between simplicity of the equation and prediction capabilities.

$$\frac{da}{dN} = \frac{C\Delta K^m}{(1-R_{eff})K_c - \Delta K} \tag{4}$$

Constants have to be determined from experimental results for at least two R ratios, since they depend on R.

NASGRO equation

The NASGRO database [29] uses a very complex equation which describes both the initial stage and the final stage of crack growth rate additionally to phase II.

$$\frac{da}{dN} = C[(\frac{1-f}{1-R})\Delta K]^n \frac{(1-\frac{\Delta K_{th}}{\Delta K})^p}{(1-\frac{K_{max}}{K_c})^q} \tag{5}$$

In this law the parameters are given by the following equations when R > 0:

$$f = max(R_{eff}, A_0 + A_1 * R_{eff} + A_2 * R_{eff}^2 + A_3 * R_{eff}^3) \tag{6}$$

$$A_0 = (0.825 - 0.34 * \alpha + 0.05 * \alpha^2) * (cos(\frac{\pi}{2}\frac{S_{max}}{\sigma_0}))^{(\frac{1}{\alpha})} \tag{7}$$

$$A_1 = (0.415 - 0.071 * \alpha)\frac{S_{max}}{\sigma_0} \tag{8}$$

$$A_2 = 1 - A_0 - A_1 - A_3 \tag{9}$$

$$A_3 = 2A_0 + A_1 - 1 \tag{10}$$

All needed constants are given in the NASGRO database and can be derived from various tests at different stress levels.

3.2.2. Life prediction

The quality of life-prediction results depends upon the goodness of the function that describes experimental data for the analyzed material. The example below shows the effect of using different laws to predict the life of a MIG welded Aluminium plate, with residual stresses introduced by the production process, see [2].

Figure 62 shows the crack growth rate as determined by experimental results and as predicted by different laws for the case without residual stress.

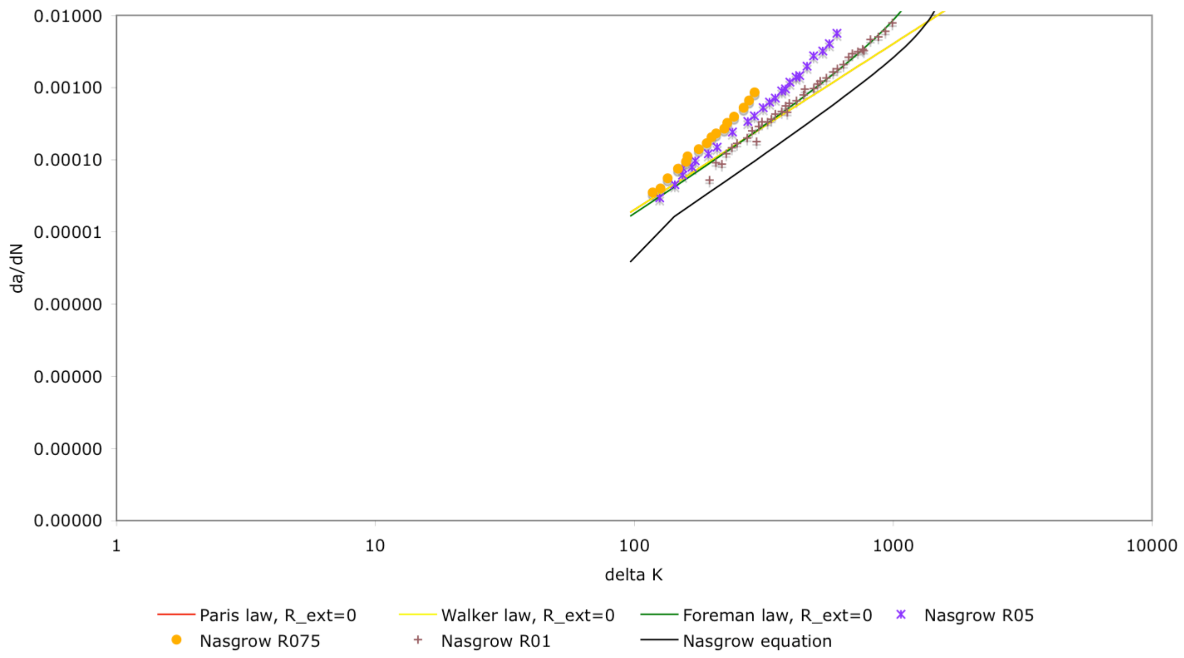

Fig. 62 - crack growth rate without residual stress

The life predictions of the different laws presented above are shown in Figures 63 through 66.

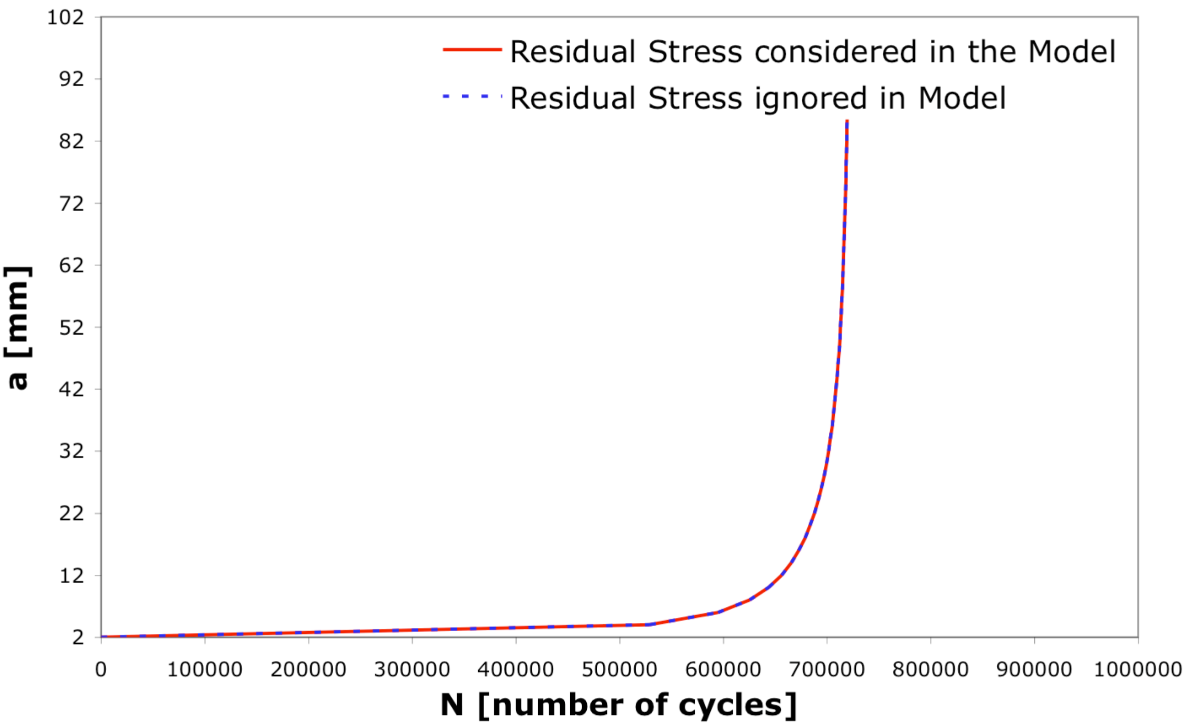

Fig. 63 - fatigue life prediction according to Paris law

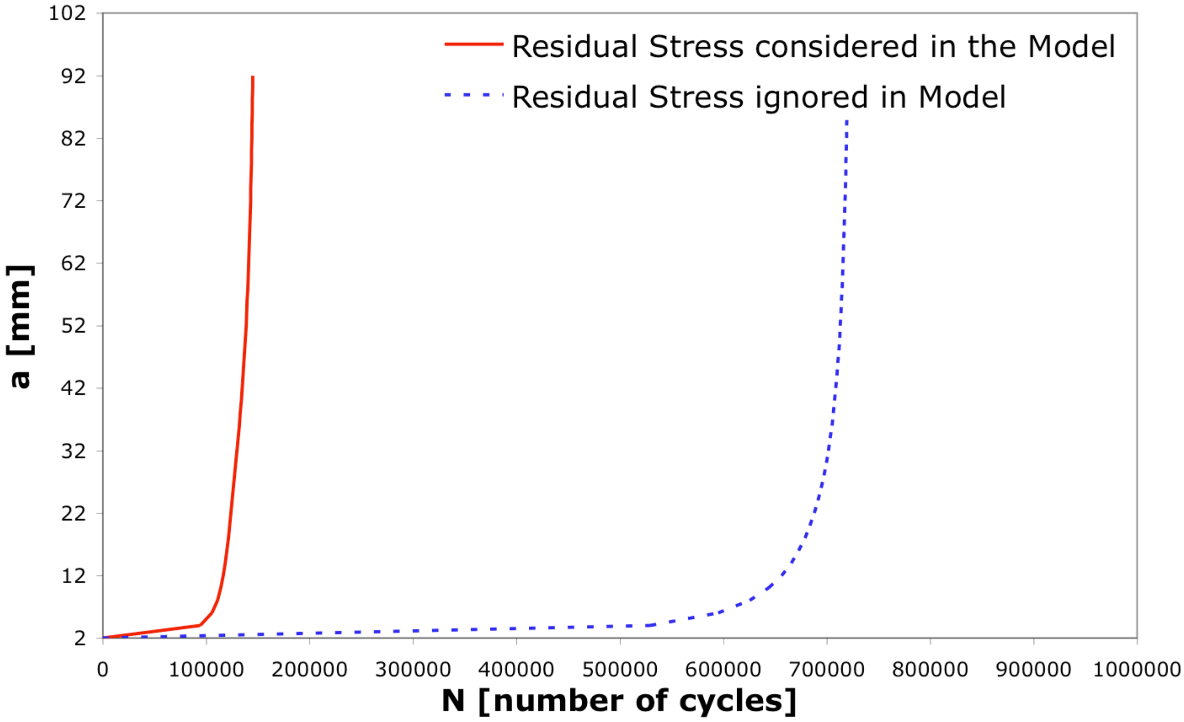

Fig. 64 - fatigue life prediction according to Walker law

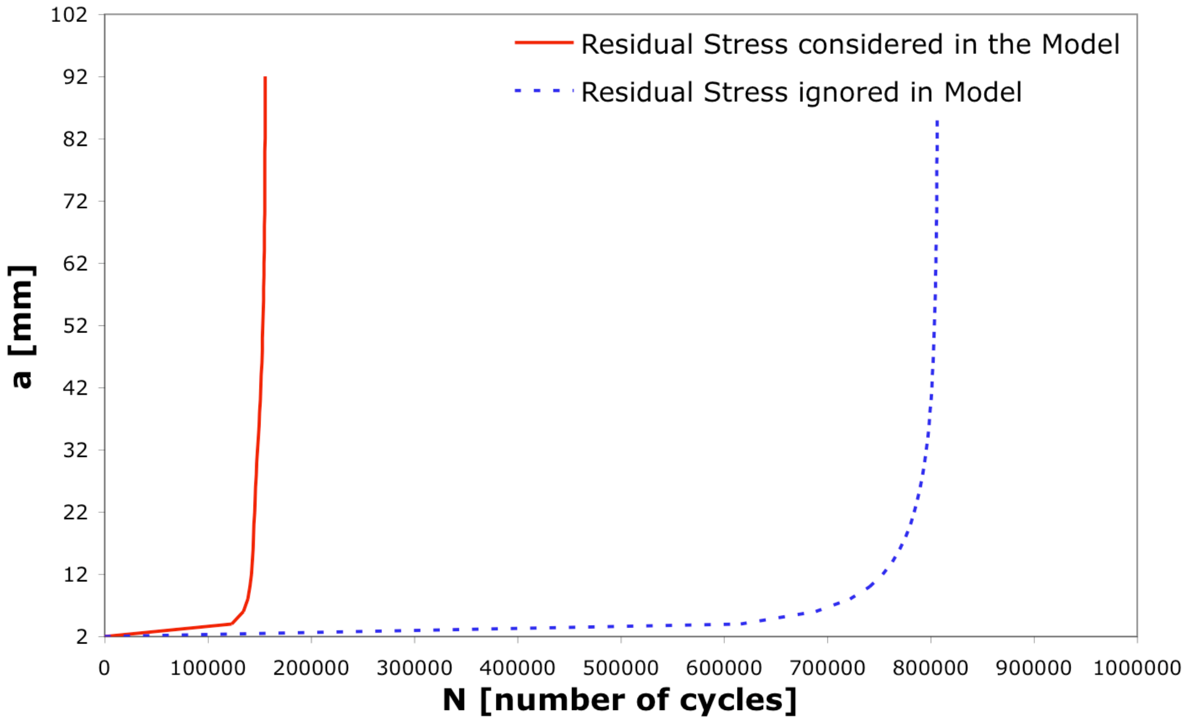

Fig. 65 - fatigue life prediction according to Foreman law

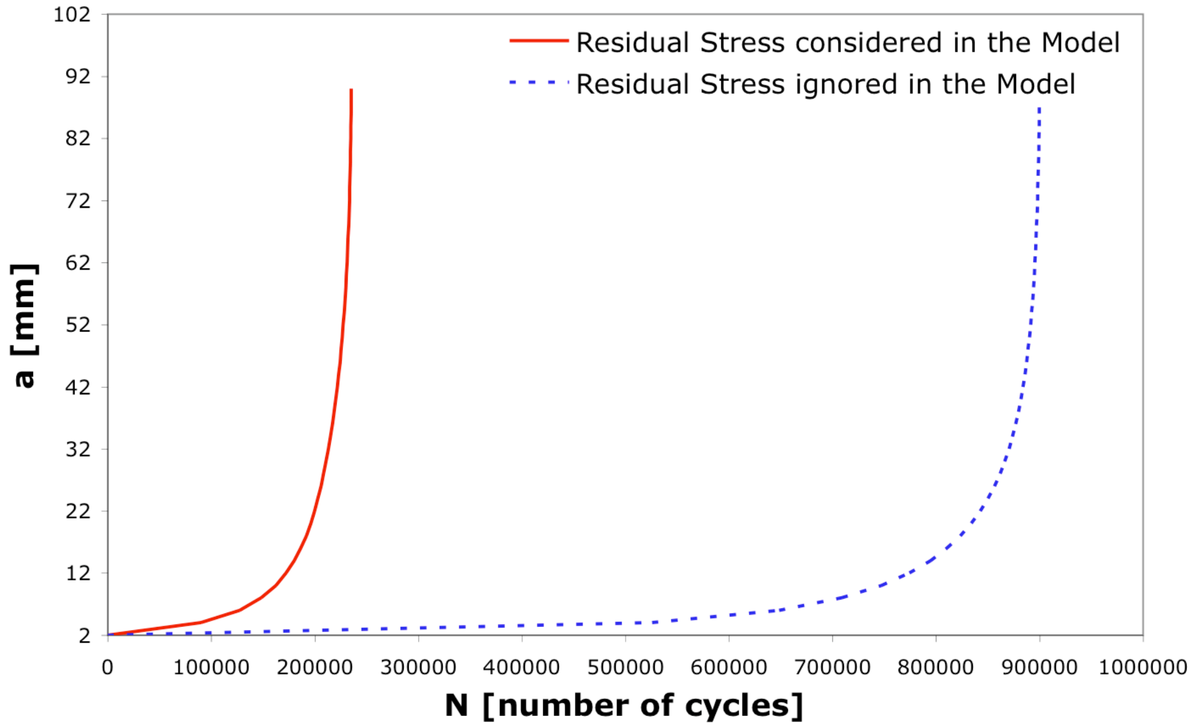

Fig. 66 - fatigue life prediction according to NASGRO equation

As can be seen, the NASGRO equation predicts the longest life for the current material, which may be due to the quality of the fit to the experimental data, which is also obtained from the NASGRO database.

4. Residual stress

As a result of the selected joining process, residual stresses may arise. These are stresses which remain locked in the interior of the body after all exterior solicitations are removed. Due to the superposition principle, it is very important to know the residual stress state of a body before applying external loads, since effects may be beneficial or detrimental to normal operation.

This part of the work aims to present and apply a method capable of obtaining the residual stress map on an arbitrary plane in the selected specimen. The destructive Contour method is used for this purpose.

4.1. MIG

Information regarding the Contour method may be found in [2]. This destructive residual stress determination process is based on the measurement of a deformation due to relaxation after a cut. This part of the work aims to complement the work presented in [30].

4.1.1. Description of the smoothing process used

The Contour method for residual stress determination is based on the measurement of a surface on which residual stresses were present before the cut was made. This method is described in another section.

The data preparation process itself starts by taking the mean value and aligning the measured data cloud to a horizontal line.

After that, the surface has to be smoothed. Since it is a very irregular surface, the smoothing is rather difficult. The following steps were taken, using a very sparse grid (parameter set: 50, 50, 4, 3) to simplify representation in the example below:

- The measured point cloud is stored in a matrix format with all three coordinates. Figure 67 shows the data-cloud, and a surface representation of the same data.

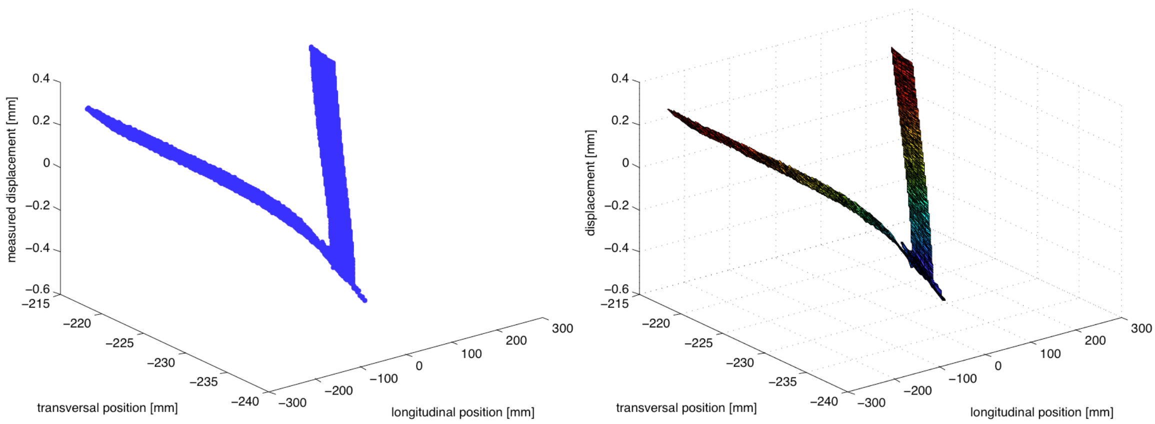

Fig. 67 - original data cloud

- Since the MATLAB surface smoothing algorithm SPAP2 only accepts regularly gridded surfaces, the measured data is extrapolated onto a regular grid which extends around the real data. For better representation, a very sparse grid was chosen for Figure 68.

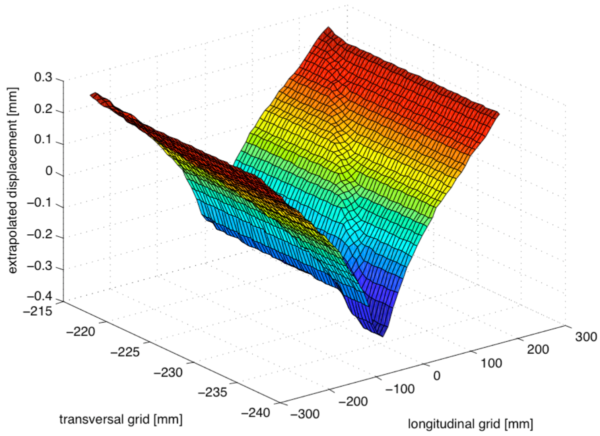

Fig. 68 - extrapolated surface measurement data

- This data can now be smoothed by the SPAP2 routine within MATLAB. The result is represented in Figure 69. On the left side in the same Figure, a representation of the “cut out” real surface is given.

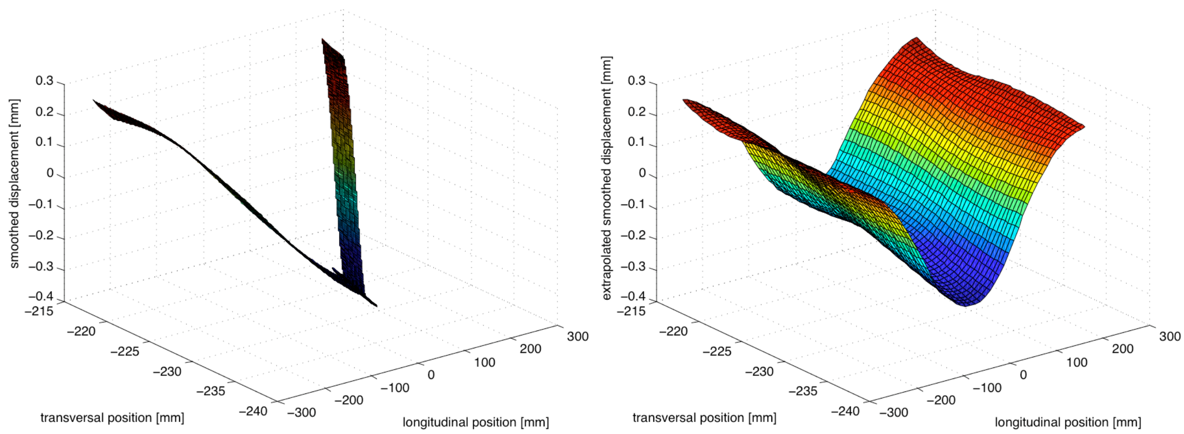

Fig. 69 - smoothed surface

- In order to verify the quality of the smoothing, it is compared to the originally measured data on 6 lines along the specimens length throughout its thickness, see Figure 70.

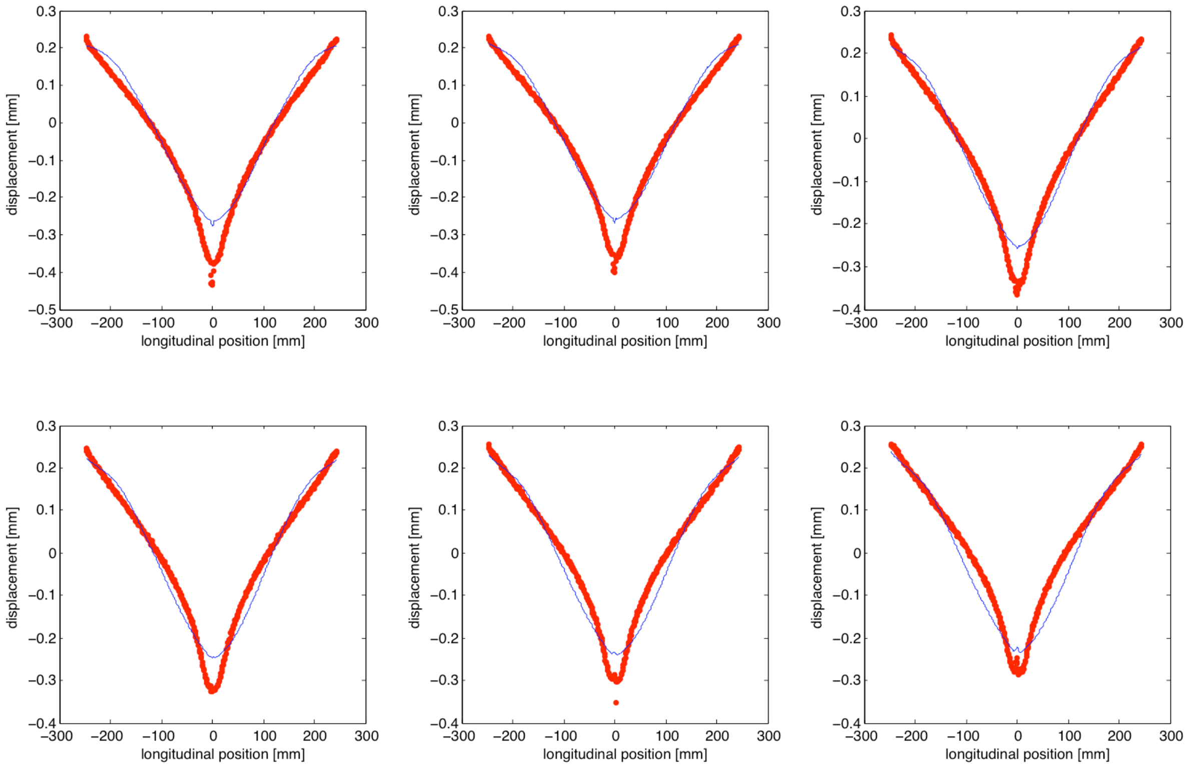

Fig. 70 - verification of the quality of the surface smoothing

The R^2 value is also calculated for each line, and the mean is taken for parameter comparison. In the example presented above, the smoothing function represents 95.36% of the measured surface.

It should be noted that the smoothing quality depends upon the distance of grid points in the regular matrix (Figure 69) and the number of polynomials used in each direction for the smoothing process. This is studied in the present report, therefore, for each parameter set, a FE analysis is run, and the stress distribution obtained is analyzed.

4.1.2. Parametric study of smoothing parameters

The MATLAB function SPAP2 can be written as:

```
z_smooth=spap2(knots,[k k],{x,y},z);
```
(11)

where knots is an array which defines the number of polynomial pieces in each direction (second two parameters analyzed), k is the order of the polynomials used in each direction of the surface and {x,y} defines the grid over which the function will act (first two parameters analyzed). As can be seen later on, four parameters have to be more thoroughly analyzed: x, y, knot(x), knot(y).

Value of k (order of polynomial pieces)

The order of the polynomial pieces used for the fitting is determined by two factors. First of all the continuity in the first derivative has to be guaranteed, since stresses are to be calculated using the smooth displacement surface. And secondly, in order to reduce the waviness in the surface, which would have a very noisy influence on the calculated stresses, the order has to be as low as possible.

From these two factors, it is determined that the polynomials have to be of second order, since it is the lowest order polynomial function which guarantees continuity in its first derivative. This is introduced as k=3 into the SPAP2 function.

Mesh density and number of polynomial pieces

At least four parameters can be changed in order to define the smooth surface. As a good way to see the fits quality is to look at the resulting stresses, one FE analysis has to be run for each parameter set. This would lead to a very high calculation time, since for each iteration it takes some time to calculate the smooth surface, and afterwards this surface has to be applied to the FE model, where a solution has to be calculated, which takes approximately another 15 minutes on a G4 with 867MHz. For this reason, only a limited number of iterations can be done, and no fully automatic routine was used for the parameter determination. Furthermore, it is difficult to create a routine capable of verifying the waviness of a surface, which is rather simple by hand.

In a first step only the deformations obtained after the smoothing algorithm were compared, then FE models were solved and the obtained stress distributions were analyzed.

Since stresses are the first derivative of displacements, a small waviness in the used surface will lead to high stress fluctuations. Since for a good fit a high number of polynomial pieces have to be used, introducing at the same time a high waviness, the smoothing process turns out to be quite complicate.

The goodness of the fit was determined in two ways. First in a visual way, to guarantee the least waviness possible in the displacement and calculated stresses, and then by determining the R-square value of the displacement fit, defined as

$$R^2 = 1 - \frac{\sum_{i=1}^{n} (z_i - (z_{smooth,i}))^2}{\sum_{i=1}^{n} (z_i - \bar{z})^2} \tag{12}$$

for each analyzed path along the plate's length. The closer this factor gets to 1, the better is the fits goodness.

With this method, it was verified and demonstrated that the fit will generally be better for finer grids and lower knot numbers.

A grid with a distance of 0.2 mm in X and 0.04 mm Y seems to give the best fit for the data. At the same time the knot number in the X and Y direction was limited to 11 and 2, since this seems to give a reasonable good fit with low waviness.

The parameter set mentioned are composed of four parameters: grid density in the X direction, grid density in the Y direction, number of polynomial pieces in the X direction and number of polynomial pieces in the Y direction.

The R^2 value for some fits is shown in Table 13. The obtained results are discussed below.

Table 13 - R^2 values

parameter set	R^2
40, 200, 4, 20	0.9591
160, 120, 60, 12	0.9987
11, 5, 9 , 3	0.991
2500, 500, 9, 3	0.9933
2470, 100, 9, 3	0.9932
2500, 500, 10, 4	0.9912
2500, 500, 8, 2	0.9854
2500, 500, 11, 3	0.9938
2500, 500, 11, 2	0.9919
2500, 500, 11, 1	0.9895
2500, 500, 12, 2	0.9906
2500, 500, 9, 2	0.9917

As can be seen, the higher waviness can also reduce the fit goodness and not only introduce a lot of noise into the stress calculation.

In order to reduce the number of possible parameter sets, it was arbitrarily defined, that the smoothed surface had to represent more than 99% of the measured data.

In Figure 71 some stress-results are represented along longitudinal paths on the specimens surface.

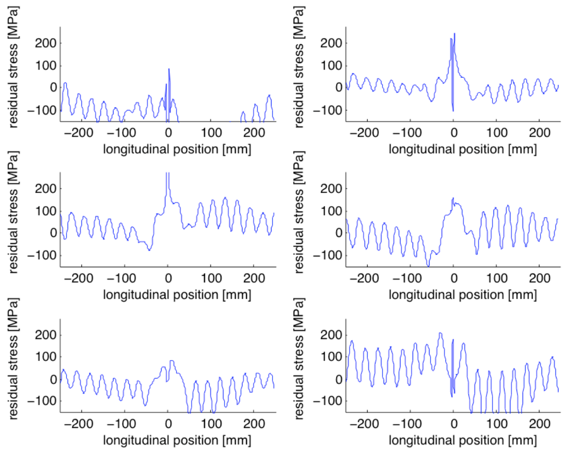

Fig. 71 a) - parameters: 160, 120, 60, 12

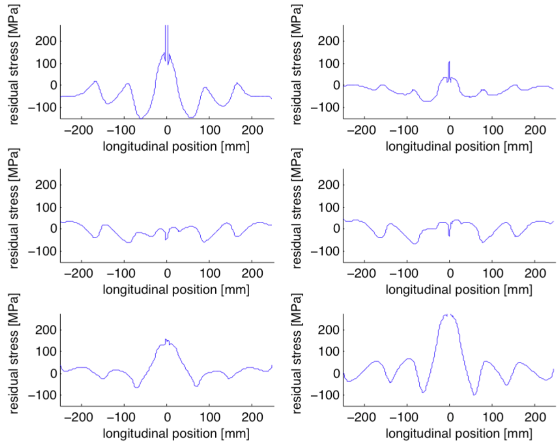

Fig. 71 b) - parameters: 2500, 500, 9, 3

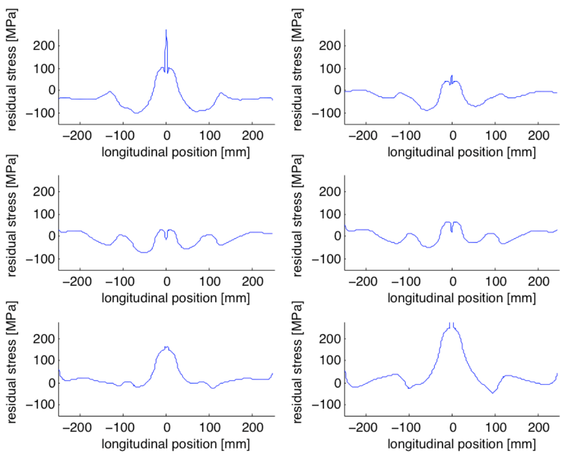

Fig. 71 c) - parameters: 2500, 500, 9, 2

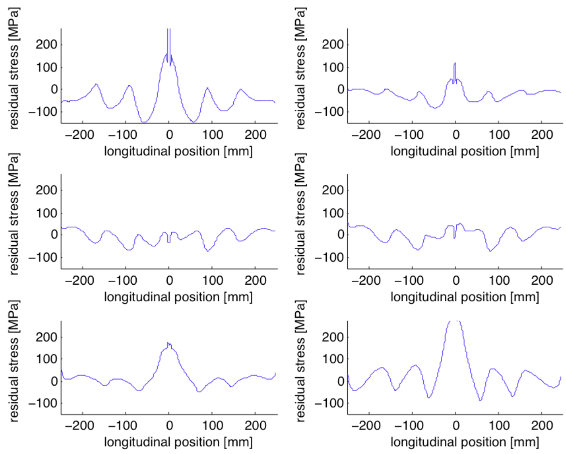

Fig. 71 d) - parameters: 2500, 500, 11, 3

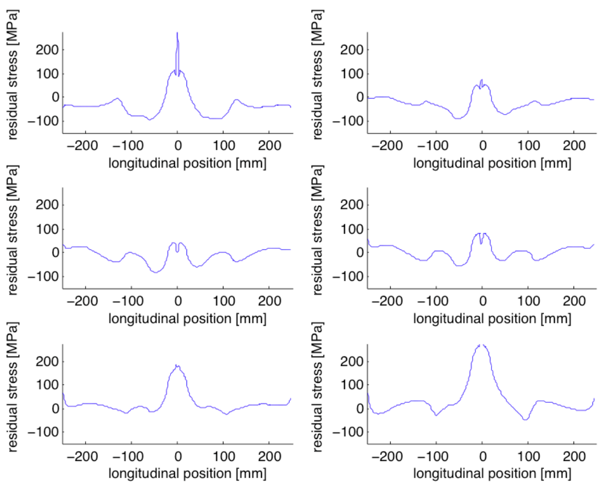

Fig. 71 e) - parameters: 2500, 500, 11, 2

From the alternatives shown above, the best fit seems to be given by the parameter set 2500, 500, 11, 2, since along with 2500, 500, 9, 2 it has the least waviness but a better goodness in terms of R^2.

Final smoothing parameters

The best fit was determined to be given by the grid x = 2500, y = 500, using 11 polynomial pieces in the X direction, and 2 in the Y direction. This leads to a surface-fit which approximates the real measured data with 99.2% accuracy, which seems to be reasonable. The waviness could not be reduced any more without loosing fit goodness.

Figures 72 show the complete representations of the stresses calculated by the selected fit on longitudinal and transversal cross-sections of the analyzed specimen.

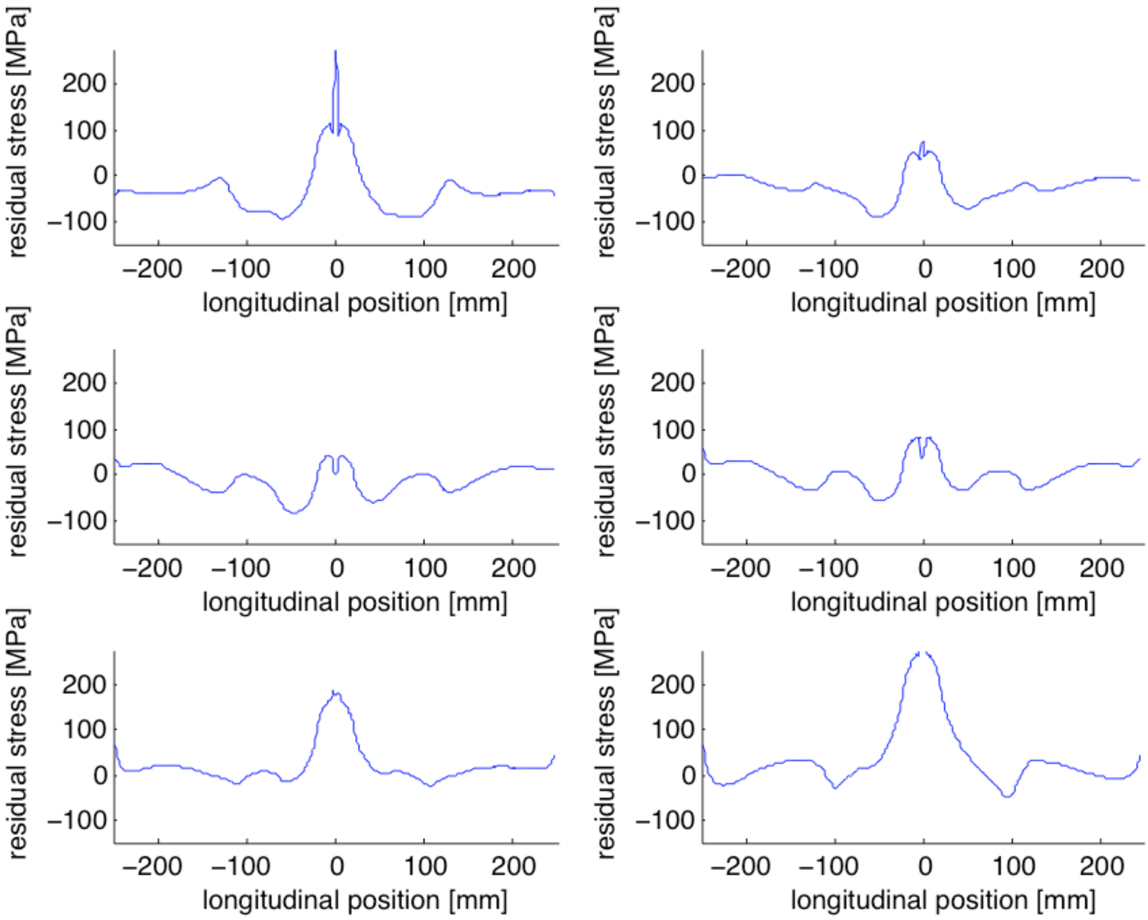

Fig. 72 a) - longitudinal stress distribution

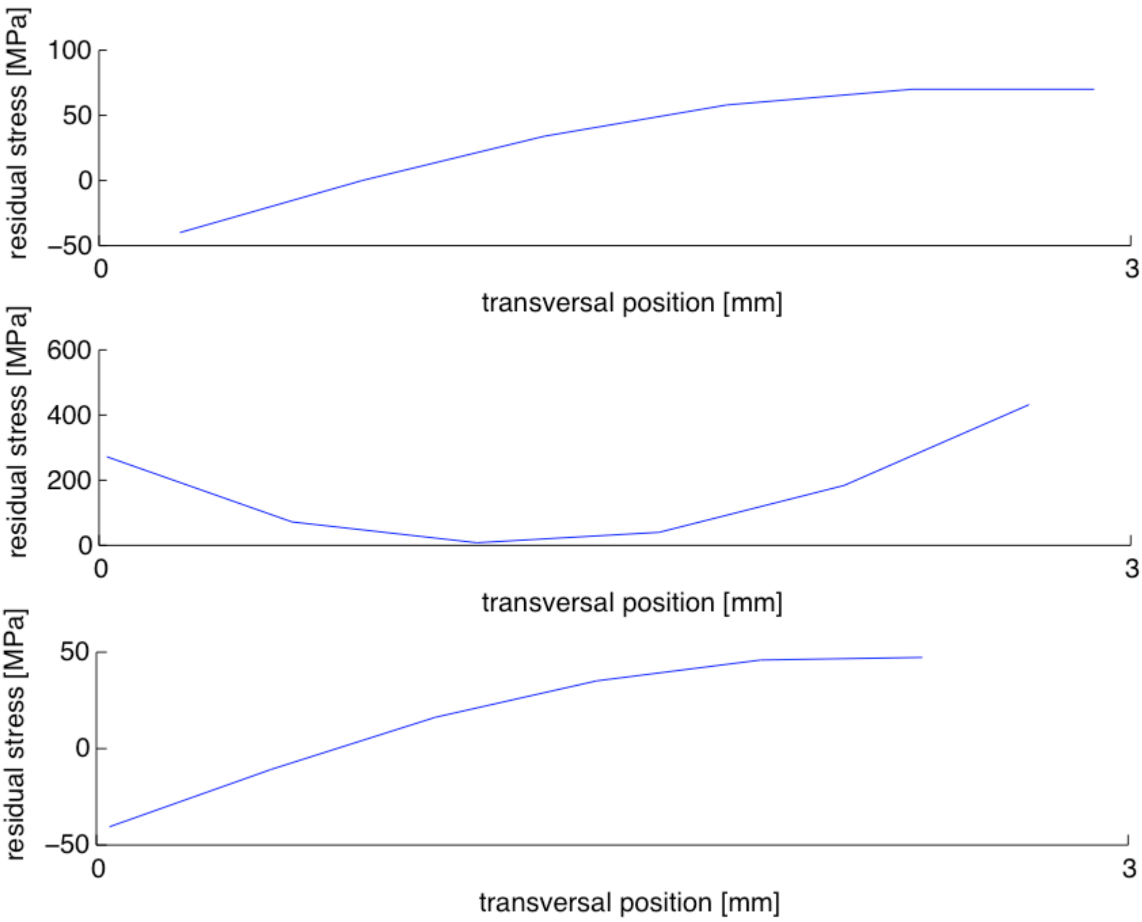

Fig. 72 b) - transversal stress distribution

Figures 73 show the surface and contour plots of the calculated longitudinal residual stresses.

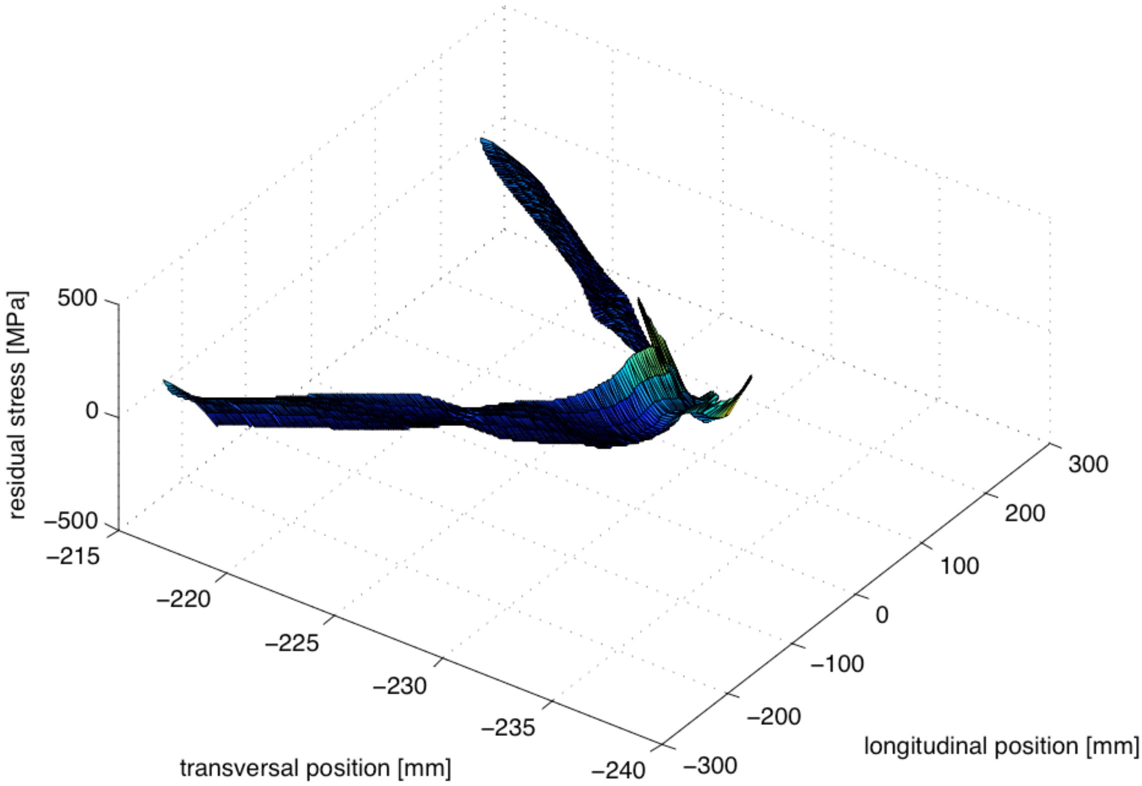

Fig. 73 a) - 3D view of the stress distribution

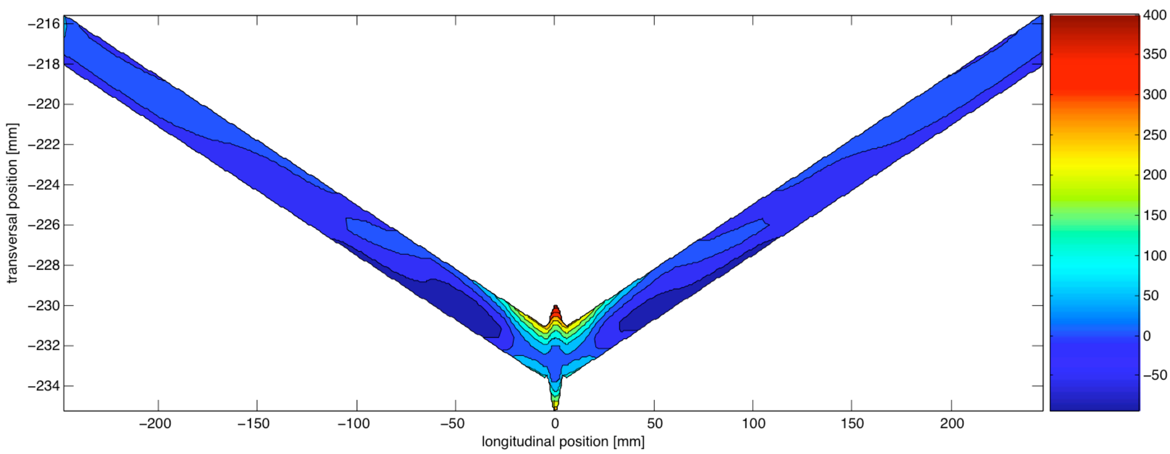

Fig. 73 b) - contour map of the stress distribution

When viewing these figures, it should be kept in mind, that the FE model used for residual stress calculation, does not consider plasticity, which would certainly happen for these high stresses.

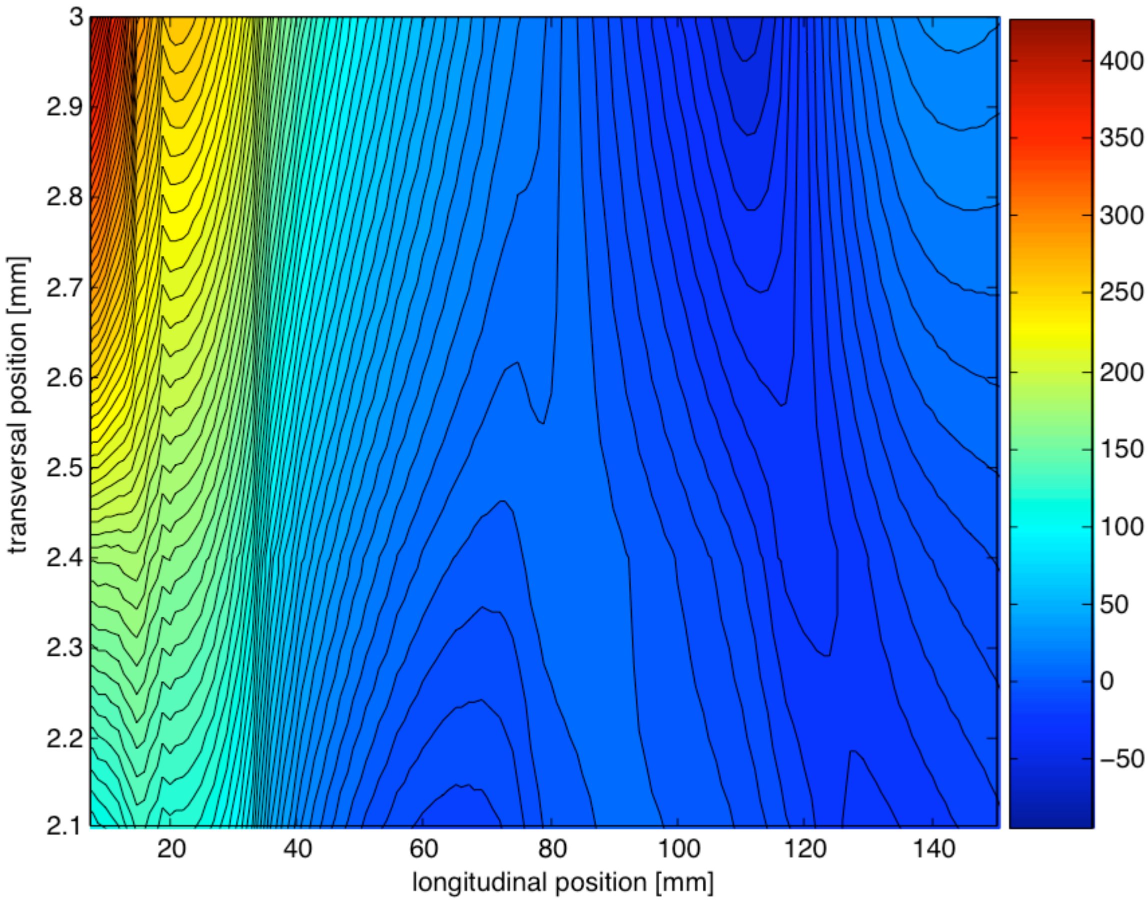

Fig. 73 c) - local contour map of the stress distribution near the weld-bead

It should be noted that for better results both plate halves have to be measured and their mean value has to be used for calculation. This has not been done for this plate. Plasticity effects that would limit residual stresses to the yield strength of the material numerically are not considered in the present model.

4.2. FSW

The measured plate was created during test C described above.

Due to maintenance problems with the only one available coordinate measuring machine[1], only one half of the plate could be successfully measured, so the results are to be looked at with some caution. Nevertheless, at least qualitative conclusions may be drawn. The calculation process is also fully presented in this part of the work, so that the introduction of the second halve of the measurements depend solely on the availability of measurement data.

[1] attempts of measuring this type of surface carried out at NORCAM proved unfortunately unsuccessful

The cut was done on a Sodick wire electro discharge machine (wEDM) at Autoconceptus in Rio Tinto, Portugal. A 0.25 mm diameter wire was used for the cutting process, and the cutting speed was about 24 mm/min.

Measurements where done on INEGIs coordinate measuring machine (CMM) Brown&Sharp model Gamma. The program used for this measurement is presented in [Annex D].

The measurement grid is spaced by 0.3 mm in the transversal direction and by 0.5 mm in longitudinal direction. The measurement of each plate half takes around 12 hours.

The plate geometry is also acquired, so a accurate FE model can be created.

For the FE model, the geometry measured before is used. The meshing is done using 20 node solid quadratic elements. In Figure 74 the mesh used is shown.

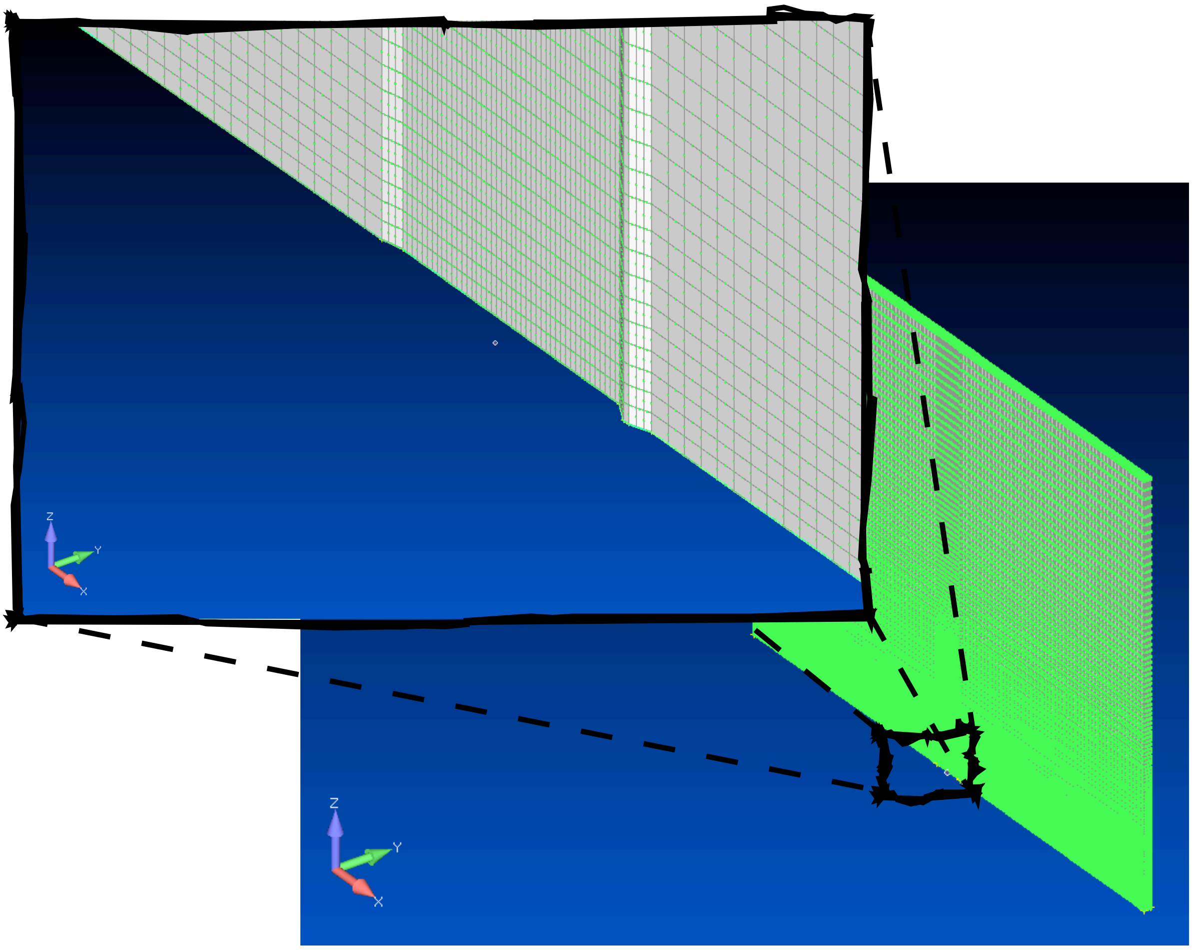

Fig. 74 - mesh used for the FE model necessary for the contour method

The measured surface is defined by 5693 nodes and 1704 elements. 60 elements are used perpendicular to the plate top-surface with a geometrical bias of 1:10. Elements are regularly spaced by 1 mm on the whole plate top-surface and refined to 0.3 mm in the welding area for a better geometry definition as can be seen in Figure 74. The complete model has 102240 quadratic elements and 466973 nodes.

The measured displacement is treated by a MATLAB algorithm presented in Annex C. Four steps are performed in this data refining process.

- Calculation of the mean of both plate half measurements; the second half of the plate will be measured as soon as the used CMM is available again. The Algorithm presented in [Annex E] is already prepared to receive this input data.
- Extrapolation of the measurements to the whole geometry. Measured data is extrapolated onto a rectangular grid that circumscribes the whole geometry. This grid is defined by 2000 x 20 points which proofed to be sufficient as can be seen by the goodness of the obtained fit.
- Smoothing using the MATLAB SPAP2 subroutine using the parameter set [2000, 20, 25, 2] described in section 4.1. This means that the extrapolated surface is described by a mesh of 2000 x 20 points, 25 quadratic functions are used in the longitudinal direction and 2 quadratic functions are used to smooth the transversal direction.
- Subtraction of the mean value in order to guarantee the necessary equilibrium between tensile and compressive stresses on the measured plane

This data preparation process leads to a relatively waveless surface which represents the raw measured data in a very high degree of accuracy. The goodness of the fit found was determined calculating the R^2 value for 7 parallel lines along the 250 mm of the plate length. Values between 97.83% and 99.51% are found, which is sufficiently high in order to have some confidence on the obtained results.

Boundary conditions on two nodes are defined. On one node the translation in two perpendicular directions (1 and 2) to the displacement direction (3) is restricted, and another nodes' displacement is restricted in direction 2 in order to limit free body movement and rotation.

Solving this model takes around 40 min on a dedicated Intel Xeon machine running Linux, using one core and 4GB of RAM.

The smoothing process is similar to the one described for the case of the MIG welded plate, being the only difference that in the present case quadratic shape function elements are used. The necessary data preparation code is presented in [Annex E].

After running the FE model, the applied deformation creates stresses, which are equal to the residual stresses that would be present if no cut had been made, see Figure 75.

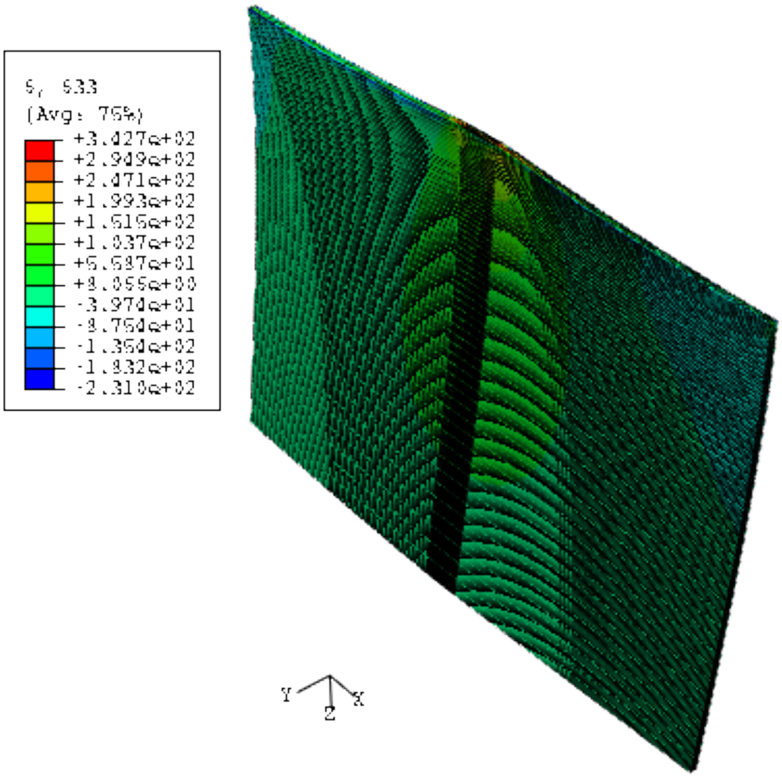

Fig. 75 a) - deformed finite element model for residual stress calculation by the contour method

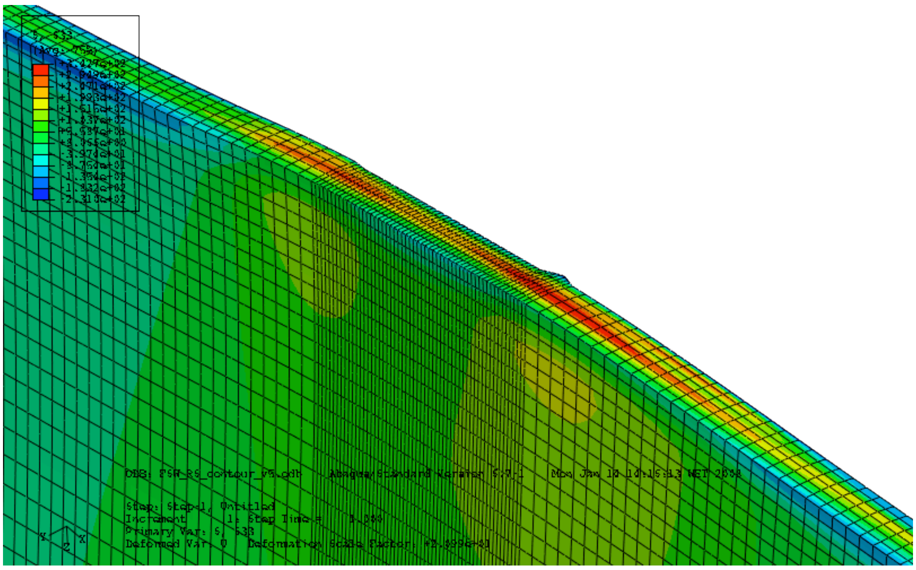

Fig. 75 b) - deformed finite element model for residual stress calculation by the contour method - magnification of Figure 75 a)

Since the deformation is applied with the opposite signal of the measured displacement, stresses calculated by this model are the required residual stresses presented in Figure 76 for longitudinal and transversal cross-sections on the plane of interest.

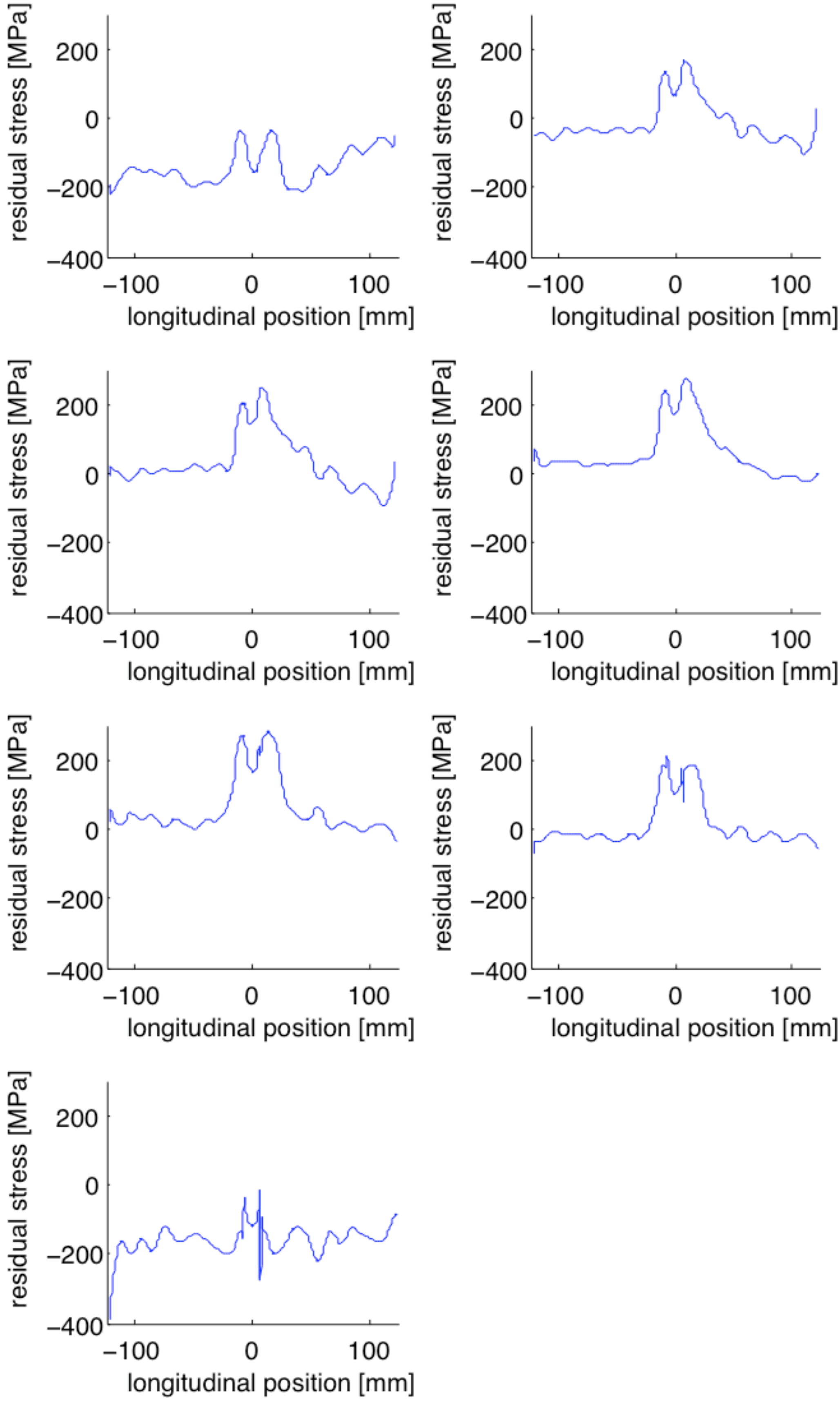

Fig. 76 a) - longitudinal stress distribution on 7 parallel lines

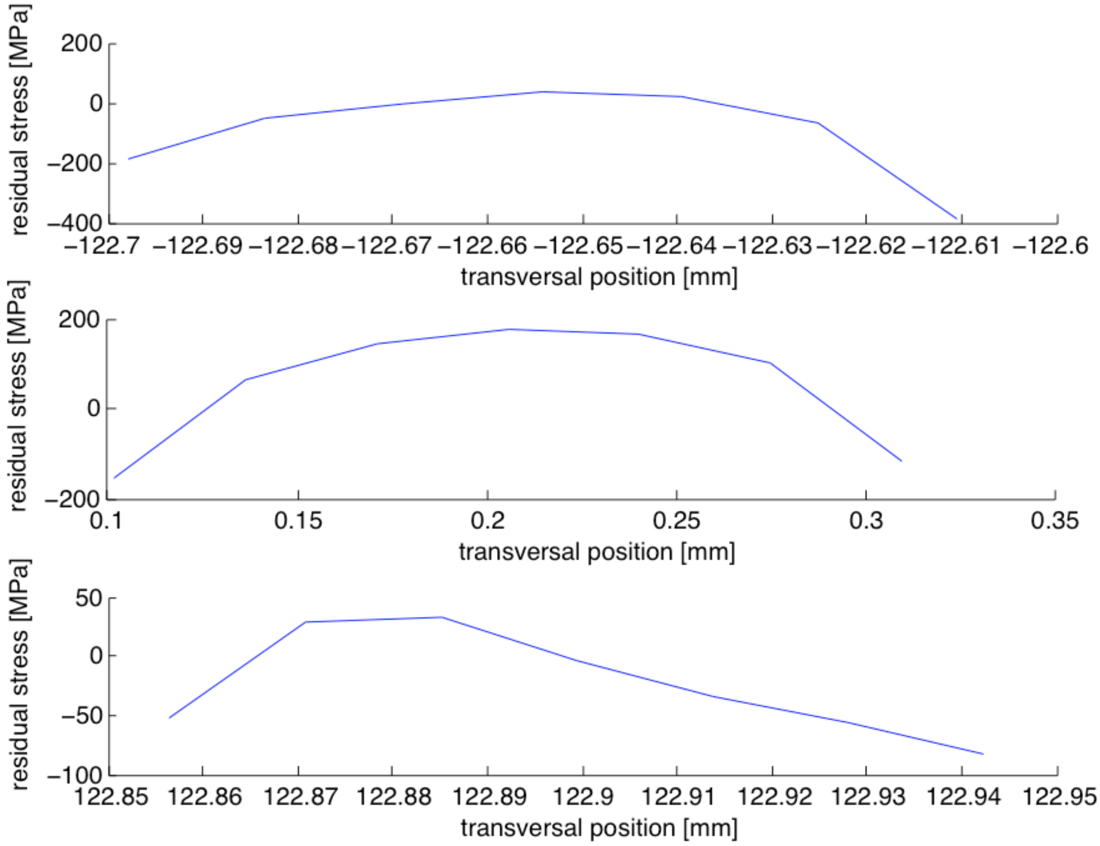

Fig. 76 b) - transversal stress distribution on 3 parallel lines (on both ends of the plate and the middle-line)

Figures 77 show the same stresses presented as surface and contour plots.

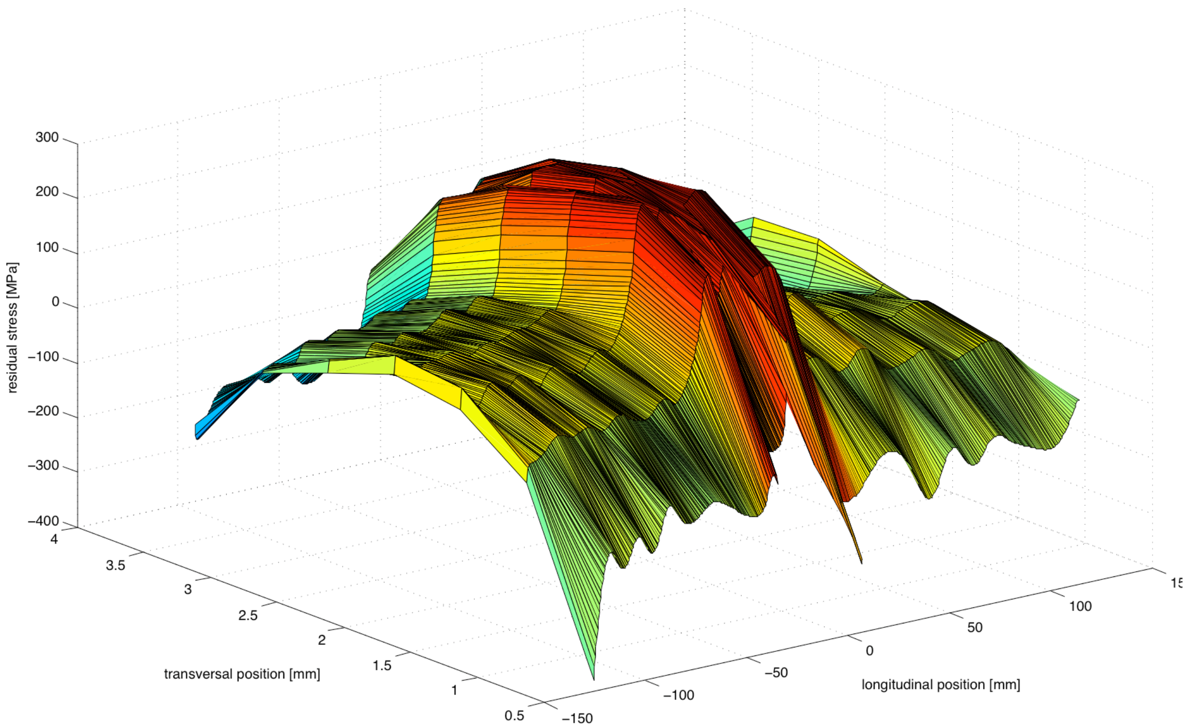

Fig. 77 a) - Three dimensional view of the residual stress distribution

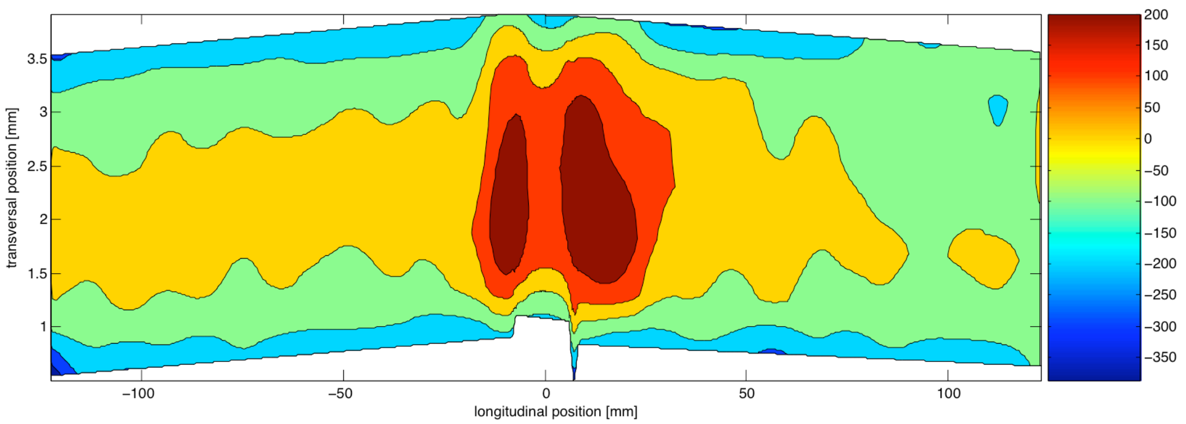

Fig. 77 b) - Contour plot of the residual stress distribution

As it can be seen especially in Figure 77 a), the typical "M" shape is obtained for the residual stress distribution using the contour method. The obtained stresses are not completely symmetric in relation to the welding line, which can be partly explained by the welding process itself which is also non-symmetric. Higher residual stresses are found on the retreating side of the weld.

At a longitudinal distance of 40 mm from the center of the welding line, residual stresses of the order of -100 MPa are found on the surface. It should however be noted that this results have to be recalculated as soon as the second half of the plate is measured. During FS welding tests, stresses of about -5 MPa are measured in longitudinal direction after the tool has passed and the bars have been removed, releasing forces and leaving residual stresses on the plate. It should be noted that only a tendency may be seen in this way, since the intact plate does not permit the strain gauge to measure the real residual stresses on the plate. The measuring process requires the whole stresses to be relaxed for deformation measurement.

5. Concluding remarks

5.1. Conclusions

- Temperature distribution during MIG and FS welding processes was successfully determined using thermocouples and FBG sensors.
- Deformation was measured by strain gauges during FS welding and by FBG sensors during both welding processes. Further study has to be made in order to gain confidence in the obtained results.
- Infrared thermography was successfully applied for determination of the tool temperature during a FS weld.
- Forces acting during a FS weld were acquired and a reasonable similarity to literature data has been found.
- Fatigue life of LB welded specimens was characterized by SN tests. A simple metallographic analysis of these specimens was also performed.
- CT-specimens were tested in order to characterize the fatigue crack growth behavior one Al alloy subjected to two different heat treatments, and good agreement with published data was found.
- A comparison of different crack growth laws was made. The importance of including residual stresses into fatigue life prediction models was demonstrated.
- Through the thickness longitudinal residual stresses were determined for both MIG and FS welded plates.

5.2. Suggestions for further work

- High temperature strain gauges should be used for deformation measurement during both welding processes.
- The optimum FBG sensor gluing technique for strain measurement has to be identified and tested.
- When applying the Contour method to determine residual stresses, both plate halves have to be considered. As soon as the used CMM is available again, these measurements should be made.
- Other well known residual stress measurement techniques like for example the sectioning technique or the hole-drilling technique should be applied to both plates for validation of the Contour method.

References

[1] The quote Lady (http://www.quotelady.com/subjects/testing.html) (December 2007)

[2] V. Richter-Trummer, “Residual Stress Measurement Using the Contour and the Sectioning Methods: Application to MIG and FSW Joints”, LEM - final report, FEUP, July 2007

[3] TWI (http://www.twi.co.uk/j32k/unprotected/band_1/fswintro.html) (September 2007)

[4] P. M. G. P. Moreira, T. Santos, S. M. O. Tavares, V. Richter-Trummer, P. Vilaça, P. M. S. T. de Castro, “Friction stir welds of dissimilar aluminium alloys AA6061-T6 and AA6082-T6. Mechanical characterization”, XIII Conference of Sociedade Portuguesa de Materiais, Materiais 2007, Porto, April 1-4, 2007

[5] Eclipse aviation (http://www.eclipseaviation.com/index.php?option=com_newsroom&task=viewarticle&id=72&Itemid=51) (September 2007)

[6] http://www.manufacturingtalk.com/news/mij/mij107.html (September 2007)

[8] J. C. Ion, “Laser beam welding of wrought aluminium alloys”, Science and Technology of Welding & Joining, Volume 5, Number 5, October 2000 , pp. 265-276

[9] Wikipedia: Fiber Bragg Grating (http://en.wikipedia.org/wiki/Fiber_Bragg_Grating)

[10] Wikipedia: electromagnetic spectrum (http://en.wikipedia.org/wiki/Electromagnetic_spectrum) (November 2007)

[11] F. P. Incropera, D. P. DeWitt, T. L. Bergman, A. S. Lavine, “Fundamentals of Heat and Mass Transfer”, 6th Edition, Wiley 2007, ISBN: 978-0-471-45728-2

[12] Vishay, Data Book, precision strain gages, 2005

[13] R.J. Dexter, P. J. Pilarski, “Crack propagation in welded stiffened panels”, Journal of Constructional Steel Research, Volume 58, 2002, pp. 1081-1102

[14] S. Lomolino, R. Tovo, J. dos Santos, “On the fatigue behaviour and design curves of friction stir butt-welded Al alloys ”, International Journal of Fatigue, Volume 27, 2005, pp. 305–316

[15] The Aluminium Association (http://www.aluminium.org) (January 2008)

[16] Wikipedia: Aluminium alloy (http://en.wikipedia.org/wiki/Aluminium_alloy) (January 2008)

[17] http://www.powerofaluminium.com/html/alloys.htm (January 2008)

[18] http://www.key-to-metals.com/Article74.htm (January 2008)

[19] P. M. G. P. Moreira, F. M. F. de Oliveira, P. M. S. T. de Castro, “Friction stir welded aluminium alloy 6063-T6: Mechanical Characterization, fatigue tests and defects identification”, 8th MESO - 2006 International Conference on Mesomechanics, Porto, Portugal, July 19-22, 2006

[20] P. M. G. P. Moreira, F. M. F. de Oliveira, P. M. S. T. de Castro, “Fatigue behaviour of notched specimens of friction stir welded aluminium alloy 6063-T6”, Journal of Materials Processing Technology, in press, 2008

[21] T. Neumann, R. Zettler, P. Vilaça, J. F. dos Santos, L. Quintino, "Analysis of self-reacting friction stir welds in a 2024-T351 alloy", Friction Stir Welding and Processing IV: pp. 55-72, 2007

[22] P. M. G. P. M. Moreira, V. Richter-Trummer, S. M. O. Tavares, F. M. F. de Oliveira, P. M. S. T. de Castro, “Characterization of fatigue crack growth rate of AA6056 T651 and T6. Application to DaToN panels life prediction”, DaToN–WD5-WP2-WP3–1.0/ IDMEC, 21st December 2007

[23] ASTM E647-05, “Standard Test Method for Measurement of Fatigue Crack Growth Rates”, 2007

[24] W. Vaidya, K. Angamuthu, M. Kocak, “Effect of load ratio and temper on fatigue crack propagation behaviour of Al-Alloys AA 6056”, in 8th International Fatigue Congress - FATIGUE 2002, 2002, Stockholm, Sweden

[25] ASTM E8-03 - “Standard Test Methods for Tension Testing of Metallic Materials”, 2004.

[26] LANEMA catálogo online 08 (http://www.lanema.pt/portugues.html) (October 2007)

[27] LANEMA catálogo técnico 05

[28] P. Paris, P. Gomez, and W. Anderson, “A rational analytic theory of fatigue”, The Trend in Engineering, Volume 13, 1961, pp. 9-14

[29] Southwest Research Institute (http://www.swri.org/4org/d18/mateng/matint/NASGRO/) (September 2007)

[30] V. Richter-Trummer, S. M. O. Tavares, P. M. G. P. Moreira, P. M. S. T. de Castro, “Residual stress measurement using the Contour and the sectioning methods: application to MIG and FSW joints”, Poster presented at Residual Stress Summit 2007, October 2-4, 2007, Oak Ridge, Tennessee, USA, (included in CD available from SEM - Society for Experimental Mechanics).

A. Thermocouple production

Thermocouples may be bought ready-made, or they may be custom made. Custom-made thermocouples have a lower price-tag, can be made to the necessary specifications and are readily available.

In this annex the thermocouple creation process is shown.

A.1. Necessary laboratory equipment

Figure A.1 shows the necessary laboratory equipment for thermocouple creation.

Fig. A.1 - general view over the used equipment

The equipment consists of a DC power supply which loads the capacitor which is used for an electric discharge necessary for the welding process.

A.2. Production

In order to join the tip of the thermocouple wires, the plastic insulation has to be peeled of and the tips of the wires have to be twisted. After that, the tip is connected to one of the electric outlets of the capacitor and immersed into a mercury bath where the second outlet is connected. An electric discharge takes place which welds both wires together. Figure A.2 shows the mercury bath where the actual welding takes place.

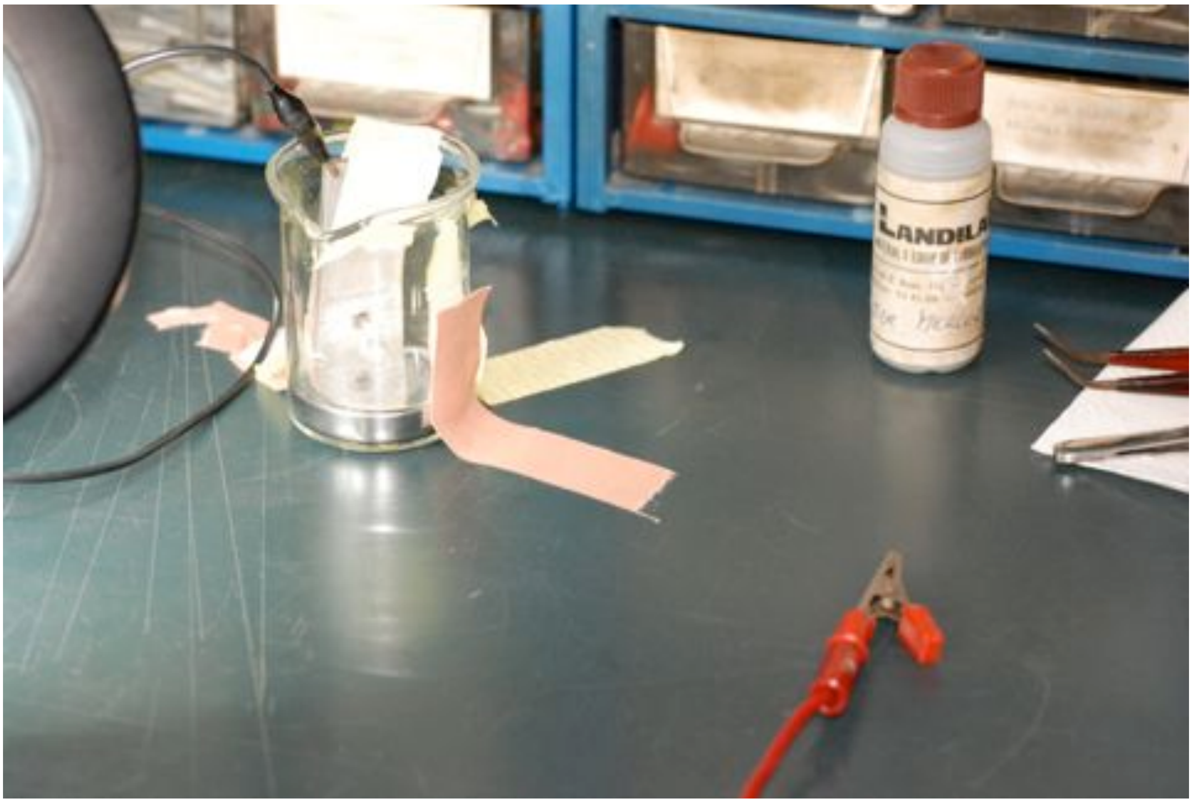

Fig. A.2 - mercury bath for thermocouple welding

The finished thermocouple should then be insulated using cyanoacrylate based glue so that no electrical signal influences the measured results during welding processes for example.

B. Interpretation of thermal imaging movies using MATLAB

Thermal imaging per se is interesting, but it is only useful, if the information can be adequately analyzed. Since data is acquired at a relatively high frame rate, only an automated image analysis process can lead to worthy results. Two algorithms are presented below, which help to generate interpretable results from a thermal imaging device.

B.1. Description of the algorithm

Two different algorithms are used for thermal image interpretation.

The first one transforms thermal images into temperature distribution graphics along the time, creating a video file. This is especially useful for the case of a MIG weld where temperature on the flat plate is acquired and therefore interpretation of the graphics is simplified by the geometry.

The second algorithm works in a similar way as the first one, but the output is a simple graphic of temperature variation along time for different points defined before.

Both algorithms are based on a simple logic. The video-file acquired by the thermal imaging device is transformed in a RGB image sequence using Quick Time Pro. Each image is than transformed into intensity images inside MATLAB. The intensities defined for each pixel on the image are transformed into temperature information by leveling the stored information with the minimum and maximum temperatures of the defined acquisition scale. This creates a temperature matrix for each frame with the dimensions of the original image, which has stored the temperature information for each pixel. Along time, both before described approximations can than be taken for data output.

B.2. Input and Output

As an input for both algorithms, the temperature scale and the thermal imaging movie as an image sequence has to be given. Image sequences can easily be made using Quicktime Pros export function for example.

Output of the first algorithm will be an image sequence which can easily be transformed into a film using programs like Quicktime Pro. The film shows the evolution of a temperature distribution graphic along time.

The second algorithm outputs a simple figure in the form time vs. temperature for different points selected on the image.

B.3. Algorithm 1 - createtion of a video of temperature distribution graphics

```
clear all

clear global
```

```
close ALL
clc
% defines the scale
max_temp=454
min_temp=31.5
nome_ficheiro_entrada_1='termo/MIG'
nome_ficheiro_saida='termo_graf/MIG'
frame_nr=1311
% eliminates white crosses
RGB8 = imread(strcat(nome_ficheiro_entrada_1,'0001','.png'));
RGB64 = double(RGB8)/255;
RGB16 = uint16(round(RGB64*65535/0.1)*0.1);
I16 = .2989*RGB16(:,:,1)+.5870*RGB16(:,:,2)+.1140*RGB16(:,:,3);
I64=double(I16);
Temp=I64.*(max_temp-min_temp)./65535+min_temp;
Temp_elimina=Temp-Temp(1,1);
[l,m]=find(Temp_elimina>5);
[l_2,m_2]=find(Temp_elimina<-5);
% image analysis loop
for i=1:1:frame_nr
nome_ficheiro_entrada=nome_ficheiro_entrada_1;
    if i<1000
        nome_ficheiro_entrada=strcat(nome_ficheiro_entrada,'0');
    if i<100
        nome_ficheiro_entrada=strcat(nome_ficheiro_entrada,'0');
    if i<10
        nome_ficheiro_entrada=strcat(nome_ficheiro_entrada,'0');
    end
    end
    end

% reads the input image
RGB8 = imread(strcat(nome_ficheiro_entrada,num2str(i),'.png'));
% converts the image
```

```
RGB64 = double(RGB8)/255;
RGB16 = uint16(round(RGB64*65535/0.1)*0.1);
I16 = .2989*RGB16(:,:,1)+.5870*RGB16(:,:,2)+.1140*RGB16(:,:,3);
% tranforms colors into temperature readings
I64=double(I16);
Temp=I64.*(max_temp-min_temp)./65535+min_temp;
% eliminates white crosses from the original film
for n=1:length(l)
        Temp(l(n),m(n))=NaN;
end
for n=1:length(l_2)
        Temp(l_2(n),m_2(n))=NaN;
end
% represents the graphic with lower resolution for better video
x=1:3:size(Temp,1);
y=1:3:size(Temp,2);
[X,Y] = meshgrid(x,y);
Temp_simple_nan=inpaint_nans(Temp,0);
Temp_simple=interp2(Temp_simple_nan,X,Y,'nearest');
figure('renderer', 'zbuffer','Color',[1 1 1])
surf(Temp_simple)
zlabel('Temp [^oC]')
axis([0,130,0,130,20,400])
M(i) = getframe;
movie_frame=frame2im(getframe);
imwrite(movie_frame,strcat(nome_ficheiro_saida,num2str(i),'.png'),'
png');
frame_nr-i % counter
close all
end
close all
```

B.4. Algorithm 2 - extraction of temperature graphics along time on one point

```
clear all
clear global
close ALL
clc
% defines the temperature scale used during measurement
max_temp=414
min_temp=58.4
nome_ficheiro_entrada_1='img_seq/FSW_tool'
nome_ficheiro_saida='termo_graf/FSW_tool'
frame_nr=89
temperatura(:,1:4)=0;
% starts the loop
for i=1:1:frame_nr
nome_ficheiro_entrada=nome_ficheiro_entrada_1;
    if i<10
        nome_ficheiro_entrada=strcat(nome_ficheiro_entrada,'0');
    end
% image input
RGB8 = imread(strcat(nome_ficheiro_entrada,num2str(i),'.png'));
% converts the image
RGB64 = double(RGB8)/255;
RGB16 = uint16(round(RGB64*65535/0.1)*0.1);
I16 = .2989*RGB16(:,:,1)+.5870*RGB16(:,:,2)+.1140*RGB16(:,:,3);
% transforms colors into a temperature scale
I64=double(I16);
Temp=I64.*(max_temp-min_temp)./65535+min_temp;
close all
% records the temperature on each point for the analyzed frame
temperatura(i,1)=mean(mean(Temp(305:320,130:145)));
temperatura(i,2)=mean(mean(Temp(305:320,195:220)));
temperatura(i,3)=mean(mean(Temp(309:324,167:182)));
temperatura(i,4)=mean(mean(Temp(225:240,180:195)));
```

```
end
close all
% represents the analyzed points for verification
Temp(305:320,130:145)=NaN;
Temp(305:320,195:220)=NaN;
Temp(309:324,167:182)=NaN;
Temp(225:240,180:195)=NaN;
figure(2)
surf(Temp)
axis equal
figure(1)
x_plot=1:frame_nr;
plot(x_plot,temperatura(:,1),x_plot,temperatura(:,2),x_plot,tempera
tura(:,3),x_plot,temperatura(:,4))
legend('point 1','point 2','point 3','point 4')
xlabel('time [s]')
ylabel('temperature [^oC]')
```

C. Fatigue crack growth rate according to ASTM E647 using MATLAB

The algorithm shown below is a translation of the FORTRAN code presented in the ASTM standard E647 into MATLAB programming language. Some differences exist in input and output of data, but the functionality is the same in both codes.

C.1. Description of the algorithm

This algorithm takes seven consecutive measured points in order to calculate the derivative (crack growth rate) of the measured points (crack length vs. number of cycles). An alternative to this method is to use the crack growth rate between every single point, but better results are obtained when more points are used due to the lower influence of measuring errors and punctual crack growth rate fluctuations.

The function “realColData.m” was written by Gerald Recktenwald (gerry@me.pdx.edu, Portland State University, Mechanical Engineering Department, 24 August 1995) and is used to import the data-file also used in the FORTRAN code.

C.2. Algorithm

```
% code that interprets crack growth data - translation of the For-
tran code
% Valentin 29.11.07
% ASTM-E647
clear all
close all
clc

% reads the input file
file='HSM1.dat';

[labels,x,y] = readColData(file,1,1,1);
nome=labels(1,1:4);
[labels,x,y] = readColData(file,1,7,1);
B=x(1,1);
[labels,x,y] = readColData(file,1,9,1);
W=x(1,1);
[labels,x,y] = readColData(file,1,11,1);
```

```
AM=x(1,1);
[labels,x,y] = readColData(file,1,13,1);
PMIN=x(1,1);
[labels,x,y] = readColData(file,1,15,1);
PMAX=x(1,1);
[labels,x,y] = readColData(file,1,17,1);
F=x(1,1);
[labels,x,y] = readColData(file,1,19,1);
TEM=x(1,1);
[labels,x,y] = readColData(file,1,22,1);
ENV=labels(1,1:2);
[labels,x,y] = readColData(file,1,23,1);
YS=x(1,1);
[labels,x,y] = readColData(file,1,25,1);
NPTS=x(1,1);
[labels,x,y] = readColData(file,2,28,1);
A=y(:,1);
N=x(:,1);
clear labels
clear x
clear y

% calculations according to ASTM-E647 standard
R=PMIN/PMAX;

A=A+AM; % calculates the real crack length

PP=PMAX-PMIN;
K=0;

NPTS=NPTS-6;
for i=1:NPTS
    L=0;
    K=K+1;
```

```
    K1=K+6;
    for j=K:K1
       L=L+1;
       AA(L)=A(j);
       NN(L)=N(j);
    end

C1=1/2*(NN(1)+NN(7));
C2=1/2*(NN(7)-NN(1));

SX=0;
SX2=0;
SX3=0;
SX4=0;
SY=0;
SYX=0;
SYX2=0;

for j=1:7
   X=(NN(j)-C1)/C2;
   YY=AA(j);
   SX=SX+X;
   SX2=SX2+X^2;
   SX3=SX3+X^3;
   SX4=SX4+X^4;
   SY=SY+YY;
   SYX=SYX+X*YY;
   SYX2=SYX2+YY*X^2;
end

DEN=7*(SX2*SX4-SX3^2)-SX*(SX*SX4-SX2*SX3)+SX2*(SX*SX3-SX2^2);
T2=SY*(SX2*SX4-SX3^2)-SYX*(SX*SX4-SX2*SX3)+SYX2*(SX*SX3-SX2^2);
BB(1)=T2/DEN;
T3=7*(SYX*SX4-SYX2*SX3)-SX*(SY*SX4-SYX2*SX2)+SX2*(SY*SX3-SYX*SX2);
```

```
BB(2)=T3/DEN;
T4=7*(SX2*SYX2-SX3*SYX)-SX*(SX*SYX2-SX3*SY)+SX2*(SX*SYX-SX2*SY);
BB(3)=T4/DEN;
YB=SY/7;
RSS=0;
TSS=0;

for j=1:7
    X=(NN(j)-C1)/C2;
    YHAT=BB(1)+BB(2)*X+BB(3)*X^2;
    RSS=RSS+(AA(j)-YHAT)^2;
    TSS=TSS+(AA(j)-YB)^2;
end

R2=1.0-RSS/TSS; % calculates R^2 for error minimization

DADN(i)=BB(2)/C2+2.0*BB(3)*(NN(4)-C1)/C2^2;% calculates da/dN
X=(NN(4)-C1)/C2;
AR=BB(1)+BB(2)*X+BB(3)*X^2;
S=1E+10;
SNET=0;
QQ=i+3;

% uses 7 consecutive points for rate calculation
T=AR/W;
FT=((2+T)*(0.886+4.64*T-13.32*T^2+14.72*T^3-5.6*T^4))/(1-T)^1.5;
S=YS*sqrt(pi*W*(1-T))/2;

DELK(i)=(FT*PP)/(B*sqrt(W));
AX=DELK(i)/(1-R);

% output of results and data verification
if ((AX >= S)||(SNET >= YS))
    out_bad(i,1:7)=[QQ N(QQ) A(QQ) AR R2 DELK(i) DADN(i)];
```

```
    msg='data violates specimen size requirements!'
else
    out_good(i,1:7)=[QQ N(QQ) A(QQ) AR R2 DELK(i) DADN(i)];
end

end
% the code presented in the standard ends here

% curve fit and calculation of C e m for the Paris law
[fitting,gof]=fit(DELK',DADN','power1');
coef=coeffvalues(fitting);
m=coef(2)
C=coef(1)

gof_cell=struct2cell(gof);
gof_mat=cell2mat(gof_cell);
R2_fit=gof_mat(2,1)

texto=strcat('C=',num2str(C),'; m=',num2str(m),'; R^2=',num2s-
tr(R2_fit));

figure(1)
plot(DELK,DADN,'.')
xlabel('dK')
ylabel('da/dN')
title('da/dN vs. dK')
annotation('textbox','Position',[0.1625 0.8161 0.2
0.06619],'String',texto,'FitHeightToText','on');
```

D. program for measuring a plates' surface using the CMM of INEGI

D.1. Description of the algorithm for the FSW plate

The scope of the annexed source-code is the measurement of the perpendicular (to the surface) displacement of the cut-surface described in the main text and of the geometry of this plate for definition of a finite element model.

In order to have an easily interpretable source-code comments were included in some parts.

For a correct execution of the described program, the following parameters have to be introduced:

- Diameter of the used tip (a 1 mm diameter ruby tip is used)
- Name of the output file (5 digits maximum length, the program itself adds a number and file extension to each file)
- Distance between measurements in the longitudinal and perpendicular directions
- Three points have to be selected manually on the plate: start, center of the welding zone, end

After introducing this starting parameters the program runs automatically in numerical command mode. The measuring speed should be chosen as small as possible so that no significant error is introduced by the dynamics of the machine.

The output file contains information about the geometry and the displacement, This information is later analyzed and treated within the MATLAB programming environment.

D.2. Algorithm

```
program FSW[WM1,WM2]

element_array MEMORY[100]

element EL1,EL2,EL3,test0,test1,test2,test3

vector PNT1,PNT2,PNT3,tev0,tev1,tev2,tev3

real
X0,Y0,Z0,X1,Y1,X2,Y2,Xi,Yi,Zi,Xf,Yf,Zf,theta,theta1,theta2,Zseg,Xse
g

real RAD,dent,xnorm,ynorm,norma,normi,X00,Y00,av

real compr,compri,norso,norsoi,Xav,Yav,dini
```

```
real Xisv, Yisv, Xfsv, Yfsv
string NEWFN[9],FNAME[6],EMPTY[1]
integer IJK,NPT,J
!!!!!!!!!!!!!!!!!!!!!!!!!!!!!!!!!!!!!!!!!!!!!!!!!!!!!!!!!!!!!!!!!!!
string NEWF2[9],FNAM2[6],EMPT2[1]
integer IJK2,NPT2,k
real norex
!!!!!!!!!!!!!!!!!!!!!!!!!!!!!!!!!!!!!!!!!!!!!!!!!!!!!!!!!!!!!!!!!!!
! chamada da subrotina que faz a medicao completa
LEPON
endstat
! inicio da subrotina que faz a medicao completa
procedure LEPON
integer I
Zseg=3
!DISTANCIA DE SEGURANÇA CHAPA DA CHAPA NA HORIZONTAL
Xseg=7
!Distancia entrada
dent=0.2
dy("Raio da esfera")
loop
        read(RAD)
        exif RAD gt 0
end_loop
EMPTY=" "
! ABRIR FICHEIRO DE SAIDA
      dy ("Displacement file name :")
      read (FNAME)
      IJK=0
      NEWFN="         "
      loop
        incr IJK
        exif (FNAME[IJK] eq EMPTY[1]) or (IJK gt 5)
        NEWFN[IJK]=FNAME[IJK]
```

```
      end_loop
      NEWFN[IJK]="."
      NEWFN[IJK+1]="I"
      NEWFN[IJK+2]="J"
      NEWFN[IJK+3]="K"
dy ("Ponto Inicial")
!pergunta ponto
mpick (EL1)
PNT1=EL1
dy ("Ponto Soldadura")
!pergunta ponto
mpick (EL2)
PNT2=EL2
dy ("Ponto Final")
!pergunta ponto
mpick (EL3)
PNT3=EL3
dy("Ponto Inicial:",PNT1)
dy("Ponto Soldadura:",PNT2)
dy("Ponto Final:", PNT3)
X0=PNT1|x
Y0=PNT1|y
Z0=PNT1|z
X1=PNT2|x
Y1=PNT2|y
X2=PNT3|x
Y2=PNT3|y
! calcula o angulo da posicao das placas na mesa
theta1=arctan((Y1-Y0)/(X1-X0))
theta2=arctan((Y2-Y1)/(X2-X1))
dy("Angulo 1:",theta1)
dy("Angulo 2:",theta2)
!mudança de comando manual para numerico
ncmove
```

```
!move para o ponto inicial
move(X=X0,Y=Y0,Z=Z0+Zseg)
theta=theta1
!move a ponta de medicao para o ponto de inicio da placa
move(X=X0-Xseg*cos(theta),Y=Y0-Xseg*sin(theta),Z=Z0+Zseg)
move(X=X0-Xseg*cos(theta),Y=Y0-Xseg*sin(theta),Z=Z0-1)
!medicao do ponto
approach(cos(theta),sin(theta),0)
mpick(test0)
movetf(X=X0,Y=Y0,Z=Z0-1)
tev0=test0
dy("Ponto Lido:",tev0)
X00=tev0|x
Y00=tev0|y
! dini é a distancia a partir do inicio da placa em [mm]
dini=1
X0=X00+(RAD+dini)*cos(theta)
Y0=Y00+(RAD+dini)*sin(theta)
!abertura do ficheiro para escrita
openf (f0,NEWFN)
open 1 (FNAME)
rewrite (f0)
out_format (10,4)
!!!!!!!!!!!!!!!!!!!!!!!!!!!!!!!!!!!!!!!!!!!!!!!!!!!!!!!!!!!!!!!!!!
! define o avanço ao longo do comprimento da placa em [mm]
av=1
!define o comprimento da placa de forma a poder terminar o loop
compr=SQRT(SQR(X1-X0)+SQR(Y1-Y0))+SQRT(SQR(X2-X1)+SQR(Y2-Y1))
compri=1
dy("comprimento da placa",compr)
J=1
! norso é a posicao da soldadura para alterar o angulo neste local
norso=SQRT(SQR(X1-X0)+SQR(Y1-Y0))
dy("norma soldadura:",norso)
```

```
Xav=X0
Yav=Y0
k=1
!-------inicio do LOOP - COMPRIMENTO PLACA ------------------------
loop
exif compri GE compr
dy("comprimento onde esta a medir",compri)
!mover para o primeiro ponto
move(X=Xav-Xseg*sin(theta),Y=Yav+Xseg*cos(theta),Z=Z0+Zseg)
move(X=Xav-Xseg*sin(theta),Y=Yav+Xseg*cos(theta),Z=Z0-1)
!aproximação à placa segundo o sentido "positivo"
approach(sin(theta),-cos(theta),0)
mpick(test1)
movetf(X=Xav,Y=Yav,Z=Z0-1)
tev1=test1
dy("Ponto Lido:",tev1)
!mover para o segundo ponto
move(X=Xav-Xseg*sin(theta),Y=Yav+Xseg*cos(theta),Z=Z0+Zseg)
move(X=Xav+Xseg*sin(theta),Y=Yav-Xseg*cos(theta),Z=Z0+Zseg)
move(X=Xav+Xseg*sin(theta),Y=Yav-Xseg*cos(theta),Z=Z0-1)
!aproximação à placa segundo o sentido "+y"
approach(-sin(theta),cos(theta),0)
mpick(test2)
movetf(X=Xav,Y=Yav,Z=Z0-1)
tev2=test2
dy("Ponto Lido:",tev2)
Xi=tev1|x
Yi=tev1|y
Zi=tev1|z
Xf=tev2|x
Yf=tev2|y
Zf=tev2|z
!mover para o ponto inicial do perfil
```

```
!calcula a norma (espessura da placa)
norma=SQRT(SQR(Xi-Xf)+SQR(Yi-Yf))-2*RAD
dy("Espessura da placa",norma)
!-------inicio do LOOP - PERFIL ----------------------------------
! este loop faz varias medicoes equidistantes ao longo da espessura
da placa
!inicializa os contadores para o loop de cada perfil
I=1
normi=0
NPT=I
file
blknb NPT
output test1
writeln(f0,tev1|x,tev1|y,tev1|z)
output test2
writeln(f0,tev2|x,tev2|y,tev2|z)
nofile
loop
!condição que termina as medicoes no final da espessura da placa
norex=normi+dent
exif norex GE norma
!move o ponteiro de medicao
move(X=Xf-(dent*I+RAD)*sin(theta),Y=Yf+(dent*I+RAD)*cos(theta),Z=Z0
+Zseg)
approach(0,0,-1)
mpick(test3)
movetf(X=Xf-(dent*I+RAD)*sin(theta),Y=Yf+(dent*I+RAD)*cos(theta),Z=
Z0-1)
tev3=test3
dy("Ponto Lido:",tev3)
NPT=I
file
blknb NPT
output test3
```

```
writeln(f0,tev3|x,tev3|y,tev3|z)
nofile
I=I+1
!close 2
!closef (f0)
! calcula a norma do vector entre o ponto inicial do perfil e do
ultimo ponto medido
xnorm=tev3|x
dy("xnorm",xnorm)
ynorm=tev3|y
dy("ynorm",ynorm)
normi=SQRT(SQR(Xf-xnorm-RAD*cos(theta))+SQR(Yf-ynorm-RAD*sin(theta)
))
dy("norma i",normi)
end_loop
!-------fim do LOOP - PERFIL -----------------------------------
! avanco que e feito ao longo da longitudinal da placa
Xav=Xav*(J)+av*cos(theta)
Yav=Yav*(J)+av*sin(theta)
norsoi=SQRT(SQR(Xav-X0)+SQR(Yav-Y0))
!decide qual o angulo a utilizar consoante o ponto de medicao
if norsoi GE norso then
theta=theta2
end_if
dy("norma de onde esta a medir",norsoi)
dy("angulo que esta a usar",theta)
compri=compri+av
end_loop
!-------fim do LOOP - COMPRIMENTO PLACA ----------------------------
close 1
!close 2
closef (f0)
end_procedure
end_program
```

E. Data preparation and surface smoothing in MATLAB

E.1. Description of the algorithm

The algorithm below has the following main objectives:

- import geometry and displacement measurement data from the CMM from INEGI
- export a file which can be imported into FEMAP for geometry and mesh generation
- map both measured plate halves onto the same grid and calculate their mean value for all further data manipulation
- calculate the mean displacement value of both surfaces
- align the measured data with horizontal lines
- smooth the raw surface measurement data
- map the smoothed surface onto the finite element mesh and write an ABAQUS input file with this data
- write an Abaqus script for path creation which simplify the data analysis

Some comments are made in the algorithm below which help to understand the steps necessary for these tasks.

E.2. Algorithm

```
% Valentin 14.12.07
clear all
clear global
close all
clc


% code parameters
data_meas_A=importdata('FS2A.MEA',';');
def_threshold=-142.5; % defines a height to differentiate geometry and displacement data
theta=0.00813 % correction angle z
alfa=0.02118 % correction angle xy
```

```
data_meas_B=importdata('FS2A.MEA',';');
def_threshold_B=-142.5; % defines a height to differentiate geome-
try and displacement data
alfa_B=0.00813 % correction angle z
theta_B=0.02118 % correction angle xy

nodes_FEM=importdata('FSW_malha_v5.INP',',');

% imported data from half A %%%%%%%%%%%%%%%%%%%%%%%%%%%%%%%%%%%%%%%
% plot of raw data
figure(1)
plot3(data_meas_A(:,1),data_meas_A(:,2),data_meas_A(:,3),'.')
title('raw measurement data')

% separates geometry and displacement data
j=1;
k=1;
for i=1:size(data_meas_A,1)
  if (data_meas_A(i,3)<def_threshold)
    geom(j,:)=data_meas_A(i,1:2);
    j=j+1;
  elseif(data_meas_A(i,3)>def_threshold)
    def(k,:)=data_meas_A(i,:);
    k=k+1;
  end
end

% horizontal alignment: z
def_c(:,1)=def(:,1)./cos(theta);
def_c(:,3)=def(:,3)-def(:,1).*sin(theta);

% horizontal alignment: xy
def_c(:,1)=def(:,1)./cos(alfa);
def_c(:,2)=def(:,2)-def(:,1).*sin(alfa);
```

```
geom_c(:,1)=geom(:,1)./cos(alfa);
geom_c(:,2)=geom(:,2)-geom(:,1).*sin(alfa);

% position alignment X
def_c(:,1)=def_c(:,1)-min(def_c(:,1))-(122.7-1);
geom_c(:,1)=geom_c(:,1)-min(geom_c(:,1))-(122.7-1);

% position alignment Y
def_c(:,2)=def_c(:,2)-min(def_c(:,2));
geom_c(:,2)=geom_c(:,2)-min(geom_c(:,2));

% writes the geometry in a file for femap import
fid1 = fopen('node.inp', 'w');
fprintf(fid1, '*NODE, NSET=GLOBAL\n');
for i=1:length(geom_c)
fprintf(fid1, strcat(num2str(i),',\t ',num2str(geom_c(i,1)),',\t
',num2str(geom_c(i,2)),',\t  0 \n'));
end

% interpolates the measured displacement onto a common grid
% creates a matrix with node locations (8 node elements)
k=0;
for i=1:569
    for j=1:13
        if isodd(i)==0
            if isodd(j)==0
                print=0;
            elseif isodd(j)==1
                print=1;
                k=k+1;
            end
        elseif isodd(i)==1
            print=1;
            k=k+1;
```

```
        end
        if print==1
            matx(j,i)=nodes_FEM(k,2);
            maty(j,i)=nodes_FEM(k,3);
            matn(j,i)=nodes_FEM(k,1);
        elseif print==0
            matx(j,i)=NaN;
            maty(j,i)=NaN;
            matn(j,i)=NaN;
        end
    end
end

% interpolation of measured data onto the defined grid
% defines the limits of the geometry
x_min=min(nodes_FEM(:,2));
x_max=max(nodes_FEM(:,2));
y_min=min(nodes_FEM(:,3));
y_max=max(nodes_FEM(:,3));

x=linspace(x_min,x_max,2000);
y=linspace(y_min,y_max,20);

% subtracts the mean value of the displacement
media=mean(mean(def_c(:,3)))
def_c(:,3)=def_c(:,3)-media;
media=mean(mean(def_c(:,3)))

figure(24)
plot(geom_c(:,1),geom_c(:,2),'.')

figure(25)
plot3(def_c(:,1),def_c(:,2),def_c(:,3),'.')
```

```
% extrapolates the measured data onto a rectangle around the plate
z_A=griddata(def_c(:,1),def_c(:,2),def_c(:,3),x',y,'nearest');
% imported data from half A %%%%%%%%%%%%%%%%%%%%%%%%%%%%%%%%%%%%%%%

% imported data from half B %%%%%%%%%%%%%%%%%%%%%%%%%%%%%%%%%%%%%%%
figure(11)
plot3(data_meas_B(:,1),data_meas_B(:,2),data_meas_B(:,3),'.')
title('raw measurement data')

j=1;
k=1;
for i=1:size(data_meas_B,1)
  if (data_meas_B(i,3)<def_threshold_B)
    geom_B(j,:)=data_meas_B(i,1:2);
    j=j+1;
  elseif(data_meas_B(i,3)>def_threshold_B)
    def_B(k,:)=data_meas_B(i,:);
    k=k+1;
  end
end

% z
def_c_B(:,1)=def_B(:,1)/cos(theta_B);
def_c_B(:,3)=def_B(:,3)-def_B(:,1)*sin(theta_B);

% xy
def_c_B(:,1)=def_B(:,1)/cos(alfa_B);
def_c_B(:,2)=def_B(:,2)-def_B(:,1)*sin(alfa_B);
geom_c_B(:,1)=geom_B(:,1)/cos(alfa_B);
geom_c_B(:,2)=geom_B(:,2)-geom_B(:,1)*sin(alfa_B);

% X
```

```
def_c_B(:,1)=def_c_B(:,1)-min(def_c_B(:,1))-124; %metade da placa
seria 125, distancia de entrada inicial de medição é 1
geom_c_B(:,1)=geom_c_B(:,1)-min(geom_c_B(:,1))-124;

% Y
def_c_B(:,2)=def_c_B(:,2)-min(def_c_B(:,2));
geom_c_B(:,2)=geom_c_B(:,2)-min(geom_c_B(:,2));

media_B=mean(mean(def_c_B(:,3)))
def_c_B(:,3)=def_c_B(:,3)-media_B;
media_B=mean(mean(def_c_B(:,3)))

z_B=griddata(def_c_B(:,1),def_c_B(:,2),def_c_B(:,3),x',y,'nearest')
;

% rotates plate B so that each point can be located on halves A and
B
%     for j=1:size(z_B,1)
%         z_B_rotate(size(z_B,1)-j+1,:)=z_B(j,:);
%     end
% z_B=z_B_rotate;
% imported data from half B
%%%%%%%%%%%%%%%%%%%%%%%%%%%%%%%%%%%%

% calculates the mean between both plate halves
for i=1:length(x)
    for j=1:length(y)
            z(j,i)=(z_A(j,i)+z_A(j,i))/2; % z_B when measurements
are done..
    end
end

% subtracts the mean of the measurements
media=mean(mean(z))
z=z-media;
```

```
media=mean(mean(z))

% surface plot of the extrapolated rectangle
z=z';
figure(6)
surf(x',y',z')
xlabel('longitudinal grid [mm]')
ylabel('transversal grid [mm]')
zlabel('extrapolated displacement [mm]')

NaNs_=size(find(isnan(z)))

% surface smoothing
k=3; % quadratic spline
knots={25,6};

function_smooth=spap2(knots,[k k],{x,y},z);

for i=1:569
    for j=1:13
        z_novo(j,i) = fnval(function_smooth,{matx(j,i),maty(j,i)});
    end
end

% plot of the smooth surface
clear plot_xx
clear plot_yy
clear plot_zz
k=1;
for i=1:13
   if isodd(i)==1
      plot_xx(k,:)=matx(i,:);
      plot_yy(k,:)=maty(i,:);
      plot_zz(k,:)=z_novo(i,:);
```

```
      k=k+1;
   end
end
figure(7)
surf(plot_xx',plot_yy',plot_zz')
xlabel('longitudinal grid [mm]')
ylabel('transversal grid [mm]')
zlabel('smoothed extrapolated displacement [mm]')

% restransforms the displacement matrix into a vector with the di-
placements
k=1;
for i=1:569
for j=1:13
    if isnan(z_novo(j,i))==0
    z_refinado(k)=z_novo(j,i);
    nome_node(k)=matn(j,i);
    k=k+1;
    end
end
end

% displacement file output
fid1 = fopen('INEGI_deformada.inp', 'w');
fprintf(fid1, '*BOUNDARY, TYPE=DISPLACEMENT, OP=MOD\n');
for i=1:length(nodes_FEM)
fprintf(fid1, strcat('\t
',num2str(nome_node(i)+5693),',\t',num2str(3),',\t,\t',num2str(z_re
finado(i)),' \n'));
end

% verifies the smoothing quality
x_compare_f=linspace(x_min,x_max,569);
y_compare_f=linspace(y_min,y_max,13);
```

```
for i=1:length(y)
z_compare((i-1)*length(x)+1:(i-1)*length(x)+1+(length(x)-1))=z(:,1)
;
x_compare((i-1)*length(x)+1:(i-1)*length(x)+1+(length(x)-1))=x(:);
y_compare((i-1)*length(x)+1:(i-1)*length(x)+1+(length(x)-1))=y(i);
end

z_old=griddata(x_compare,y_compare,z_compare,x_compare_f,y_compare_
f','nearest');
z_novo_compare=griddata(matx(1,:),maty(:,1),z_novo,x_compare_f,y_co
mpare_f','nearest');

figure(8)
k=1;
sum_smooth(1:13)=0;
sum_origin(1:13)=0;
for i=1:2:13;
subplot(4,2,k)
plot(matx(i,:),z_novo_compare(i,:),'b.',matx(i,:),z_old(i,:)','ro')
for j=1:length(matx(i,:))
   sum_smooth(i)=sum_smooth(i)+(z_novo_compare(i,j)-z_old(i,j))^2;

sum_origin(i)=sum_origin(i)+(z_old(i,j)-mean(z_novo_compare(i,:)))^
2;
end
goodness_of_fit(i)=1-sum_smooth(i)/sum_origin(i);
k=k+1;
end
k=1;
for i=1:2:13
goodness_of_fit_calc(k)=goodness_of_fit(i);
k=k+1;
end
goodness=min(abs(goodness_of_fit_calc)) % shows the worst case of 7
lines
```

```
% creates paths in abaqus for easier data extraction
% changes node numbers according to the femap model
old_node=[2354,...,3281:3292];
new_node=[min(old_node):max(old_node)];
nodes_FEM_n=nodes_FEM;
for i=1:length(old_node)
    linha_aux_old=find(nodes_FEM(:,1)==new_node(i));
    nodes_FEM_n(linha_aux_old,1)=old_node(i);
end
k=0;
clear matn
for i=1:569
    for j=1:13
        if isodd(i)==0
            if isodd(j)==0
                print=0;
            elseif isodd(j)==1
                print=1;
                k=k+1;
            end
        elseif isodd(i)==1
            print=1;
            k=k+1;
        end
        if print==1
            matn(j,i)=nodes_FEM_n(k,1);
        elseif print==0
            matn(j,i)=NaN;
        end
    end
end
node_abaqus=matn+5693;
fid10 = fopen('path_for_abaqus.py', 'w');
for j=1:1:13
```

```
fprintf(fid10, '\n');
fprintf(fid10, strcat('session.Path(name=''Path-',num2str(j),''',
type=NODE_LIST, expression=((''PART-1-1'', ('));
for i=1:569
if isnan(node_abaqus(j,i))==0
fprintf(fid10, strcat(num2str(node_abaqus(j,i)),', '));
end
end
fprintf(fid10, ' )) , ))');
end
```